Tunable Coupler in Superconducting Circuits and Impedance Engineering for Josephson Parametric Amplifier

by

Huichen Sun

A thesis
presented to the University of Waterloo
in fulfillment of the
thesis requirement for the degree of
Master of Science
in
Physics (Quantum Information)

Waterloo, Ontario, Canada, 2020

Author's Declaration

I hereby declare that I am the sole author of this thesis. This is a true copy of the thesis, including any required final revisions, as accepted by my examiners.

I understand that my thesis may be made electronically available to the public.

Abstract

In this thesis, we study two topics on superconducting circuits. The first topic is the tunable coupler for resonators. This coupler is implemented with a superconducting circuit coupling with resonators in the dispersive regime. It possesses a high on/off ratio and the coupling between two degenerate resonators can be turned off by tuning the frequency of the coupler via the biasing flux. We present the design, the simulation, and the fabrication of the chip implementing this coupler. We derive the Hamiltonian of the chip via formal circuit quantization. We also present numerical results of the eigenenergies and the eigenstates of the chip. From the numerical results, we show that the tunable coupling and the turn-off point can be realized on the chip.

The second topic is impedance engineering for enhancing the bandwidth of a Josephson parametric amplifier. By transforming the input impedance seen by the Josephson parametric amplifier, the frequency dependence of the gain function can be decreased and the bandwidth of the Josephson parametric amplifier can be enhanced. We study impedance engineering for two different types of flux pumping Josephson parametric amplifier. For each type of amplifier, we develop a corresponding method of impedance engineering, and study implementing the method with transmission lines.

Acknowledgements

I would like to thank my supervisor Prof. Christopher Wilson. Thank you for giving me the chance to explore the experimental life in the field of superconducting circuits. I enjoy your working style that providing insightful guidance and letting the students have freedom to arrange their research by themselves. You create a relaxed atmosphere for our lab in which everyone is willing to help others, discuss questions, and share new ideas.

I would like to thank post-doc Ibrahim for your help in fabrication. Without you, I cannot imagine how I could have learned fabrication in which so many tricks are not written in any book. I would like to thank senior group members Vadiraj and Sandbo who were always kind and ready to answer my questions. I would like to thank my fellow group members Jimmy and Jamal. We fought together on the academic way. With your company I never felt lonely in the academic life.

I would like to thank my collaborators Prof. Matteo Mariantoni, Cary Earnest, Jeremy Bejanin for your help in leading me into the world of Xmon.

I would like to thank the teachers Prof. Richard Cleve, Prof. Adrian Lupascu, Prof. Slim Boumaiza, and Prof. Achim Kempf, who provide carefully prepared vivid courses for students.

I would like to thank my supervisory committee, Prof. Michel Gingras and Prof. Eduardo Martin-Martinez, who provided consistent guidance for my research.

I would like to thank the four years' life and study at the University of Waterloo.

At the time of writing this thesis, the world is still suffering from the COVID-19 pandemic and most activities are interrupted. It is a pity that my experimental study of the tunable coupler is also affected and cannot be included in this thesis. I hope that the whole world can soon recover from the COVID-19. I also hope that my thesis can be helpful for researchers who work on similar research topics.

Dedication

Dedicated to my parents for their consistent support and love.

Table of Contents

List of Figures

List of Tables

Chapter 1

Introduction

1.1 Superconducting circuits

The past decade has witnessed a tremendous progress in the field of superconducting circuits [1, 2, 3]. With the Josephson junction working as a nonlinear element, the superconducting circuits exhibit unequally spaced quantum energy levels at low temperature which can be addressed by microwave tones with corresponding frequencies. There are three main application directions of superconducting circuits:

(1) Building blocks of quantum computer.

(2) New platform for quantum optics and fundamental physics.

(3) High-performance measurement devices.

Superconducting circuits are promising candidates as building blocks of quantum computers. The lowest two energy levels of a superconducting circuit can work as a quantum bit (qubit) to process information. Combining the technology of microfabrication and microwave engineering, superconducting qubits can be easily integrated on a chip and rapidly controlled via electromagnetic pulses. A milestone called "quantum supremacy" has been reached [4], in which scientists demonstrated a processor consisting of 53 superconducting qubits can be exponential faster than a state-of-the-art classical supercomputer in solving certain problems. The ultimate goal for quantum information processing with superconducting qubits is realizing a large scale universal quantum computer. To achieve this aim, quantum error correction codes like surface codes [5, 6] and Bosonic codes [7, 8] have been

proposed and demonstrated on superconducting qubits, in which quantum information are stored in a logical qubit consisting of multiple physical qubits to gain lower error rates.

The superconducting circuit is an excellent platform for quantum optics and fundamental physics. The parameters of a superconducting circuit can be specially designed to satisfy different experimental requirements. Unlike natural atoms which are hard to control due to their microscopic dimensions, superconducting circuits are macroscopic quantum devices fixed on chips that interact strongly with external electromagnetic fields. Many quantum optics phenomenon have been demonstrated on superconducting circuits like Rabi oscillation [9], Landau-Zener transition [10], Electromagnetically induced transparency [11, 12], and ultra strong light-matter coupling [13]. Analogous to cavity quantum electrodynamics [14] for atoms, the circuit quantum electrodynamics (cQED) [15, 16, 17] for superconducting circuits have been extensively studied and has been the basic architecture for manipulating superconducting circuits. Superconducting circuits have also been applied for exploring fundamental physics such as the dynamical Casimir effect [18], quantum trajectory theory [19], and Bell's inequality [20].

Superconducting circuits can work as high-performance measurement devices. The superconducting quantum interference device (SQUID) [21] has been used as a sensitive magnetometer for a long time before it became a building block for superconducting circuits. Another important measurement device based on superconducting circuits is the Josephson parametric amplifier (JPA) [22, 23]. JPA can achieve high gain amplification for microwave signals with very low added noises. Due to this property, JPA has been widely used in measurements of superconducting circuits as the first level amplifier.

In this thesis, we study two different topics about superconducting circuits. The first topic is related to the application directions (1) and (2) of superconducting circuits listed in the first paragraph, in which we study a superconducting circuit working as a tunable coupler for two resonators. This coupler possesses a high on-off ratio, and can be used to construct two qubit gates between the two resonators. This device is based on the cQED architecture and can be potential building blocks for quantum computers with bosonic error correction codes. Our study is both theoretical and experimental, which includes theoretical modelling, design, simulation, and fabrication of the coupler.

The second topic is related to the application direction (3) of superconducting circuits, in which we theoretically study impedance engineering for a JPA. By using transmission lines as impedance transformers, we engineer the input impedance of a JPA and modify its gain profile. This impedance engineering is an efficient method of improving the bandwidth of a JPA, as it can be implemented by adding auxiliary devices into the measurement chain without changing the JPA itself.

1.2   Thesis outline

This thesis is organized as follows. In Ch. 2, we give a brief introduction for the background knowledge of superconducting circuits. In Ch. 3 and Ch. 4, we study the first topic, the tunable coupler. In Ch. 3, we derive the theoretical model for the tunable coupler for two resonators. In Ch. 4, we focus on the design, the fabrication, and the simulation for the specific circuit implementation of the tunable coupler. In Ch. 5, we study the second topic, impedance engineering for a JPA. In Ch. 6, we summarize the whole thesis and discuss possible research directions for the future. In App. A, the full fabrication process flow of the tunable coupler is presented. In App. B, the codes for simulating the tunable coupler is presented.

Chapter 2

Superconducting quantum circuits

In this chapter, we briefly introduce the background knowledge of superconducting circuits. In Sec. 2.1, we introduce the core element of superconducting circuits, the Josephson junction. In Sec. 2.2, we introduce the direct-current superconducting quantum interference device (dc-SQUID), which can be regarded as a tunable Josephson junction. In Sec. 2.3, we introduce a main type of superconducting circuits, the transmon qubit. Specifically, we introduce the Xmon qubit, which is a transmon qubit specially designed for 2D fabrication techniques. In Sec. 2.4, we summary this chapter.

2.1 Josephson junction

A Josephson junction is made of two pieces of superconducting material connected by a weak link. The weak link can be a thin insulating layer, a short section of non-superconducting metal, or a physical constriction that weakens the superconductivity at the point of contact. In this thesis, we only consider the Josephson junction with the first type of weak link, which is known as the superconductor–insulator–superconductor (SIS) junction. In the SIS junction, the insulating layer is thin enough to let the superconducting material on both sides have a weak coupling. As a result, the Cooper pairs (a pair of electrons bound together via the electron-phonon interaction) in one side of the superconducting material can transfer to the other side via quantum tunnelling effect and generate a supercurrent.

In 1962, physicist Brian D. Josephson first predicted this phenomenon and derived the

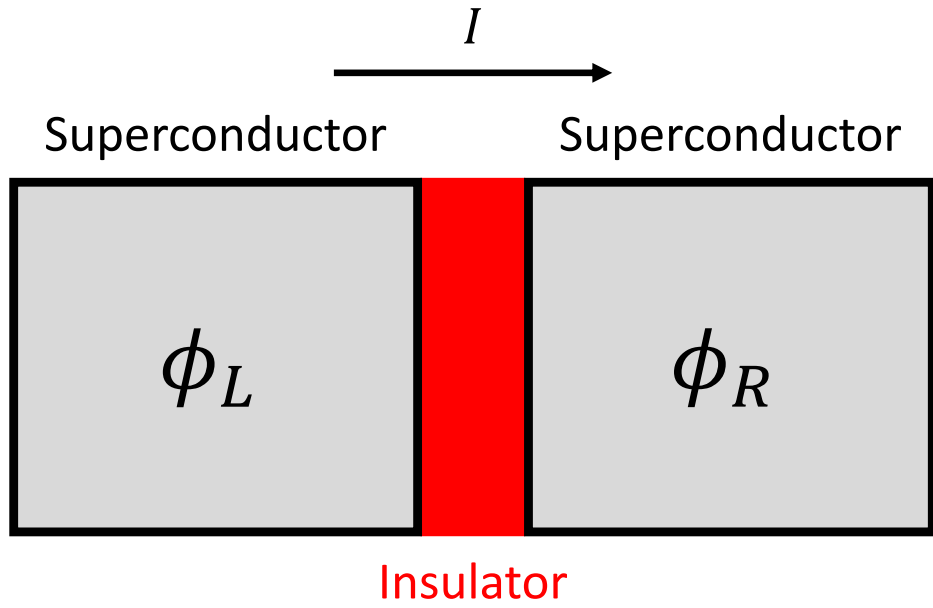Figure 2.1: Schematic of a SIS Josephson junction. A SIS junction is made of two pieces of superconductors (grey rectangles) linked by an insulator layer (red rectangle). ϕ_L (ϕ_R) represents the phase of the Ginzburg-Landau wave function for the left (right) superconductor. The positive direction of supercurrent I is defined as flowing from the left superconductor to the right superconductor.

relation between supercurrent and voltage on the Josephson junction [24]:

$$I = I_c \sin \varphi, \tag{2.1}$$

$$V = \frac{\Phi_0}{2\pi} \frac{d\varphi}{dt}, \tag{2.2}$$

where $\Phi_0 \equiv h/2e$ is the magnetic flux quantum. φ is the phase difference of the Ginzburg-Landau wave functions describing superconductors on both sides of the junction, respectively. As shown in Fig. 2.1, the phase of the Ginzburg-Landau wave function for the left (right) superconductor is ϕ_L (ϕ_R), and the positive direction of supercurrent I is defined as flowing from the left superconductor to the right superconductor, then the phase difference φ is given by $\varphi = \phi_L - \phi_R$.

I_c is an important parameter of a Josephson junction. According to Eq. (2.1), I_c represents the maximum value of the supercurrent I that can flow thought the junction, and thus called the critical current. Assuming the insulating layer has a simple 1D structure of cross-sectional area A and thickness L, we can express I_c as $I_c = J_c A$, where J_c is the critical current density of the junction that depends on the layer thickness L, the materials of the superconductor and the insulator, and the environmental factors like temperature and magnetic field. In fabricating a junction, we usually keep J_c unchanged, and vary the cross-sectional area A to obtain a junction with a certain I_c. Another important relation of I_c is the Ambegaokar-Baratoff formula [25], which relate I_c with the normal state resistance R_n of the junction through the following expression

$$I_c R_n = \frac{\pi \Delta(T)}{2e} \tanh(\frac{\Delta(T)}{2k_{\mathrm{B}}T}). \tag{2.3}$$

Here $\Delta(T)$ is the temperature dependent superconducting energy gap, e is the elementary charge, and k_{B} is the Boltzmann constant. At $T = 0$, Eq. (2.3) reduces to

$$I_c R_n = \frac{\pi \Delta(0)}{2e}. \tag{2.4}$$

For our junctions working at $20 - 50$ mK, Eq. (2.4) is a good approximation. With this relation, we can check if a junction is successfully fabricated by measuring its resistance at room temperature before cryogenic experiments.

The work done by current I on the Josephson junction is given by

$$W = \int_0^t dt' \, VI = \frac{\Phi_0 I_c}{2\pi} \int_0^\varphi d\varphi' \sin \varphi' = E_{\mathrm{J}}(1 - \cos \varphi). \tag{2.5}$$

6

Here $E_{\mathrm{J}} = \Phi_0 I_c/2\pi$ is called the Josephson energy. It is an important parameter of the Josephson junction which characterizes the coupling strength between the superconductors on both sides of the junction. Correspondingly, the energy stored in a Josephson junction can be given by $-E_{\mathrm{J}}\cos\varphi$, in which we omit a constant term.

According to Eq. (2.1) and Eq. (2.2), the Josephson junction can also be regarded as a nonlinear inductor L_{J},

$$L_{\mathrm{J}} = V\left(\frac{\partial I}{\partial t}\right)^{-1} = \frac{\Phi_0}{2\pi I_c \cos\varphi}. \tag{2.6}$$

Because of the nonlinear effects of the Josephson junction, the superconducting quantum circuits consisting of Josephson junctions have unequally spaced energy levels. In this way, we can excite specific energy levels of superconducting quantum circuits via an external electromagnetic field with corresponding frequency.

An ideal Josephson junction only allows the flowing of supercurrent. However, in a real Josephson junction, the superconductors on both sides and the insulating layer define a conductor of sorts and introduce a certain amount of resistance. In the scope of our discussion, the effects of junction capacitance should be taken into account, while the effects of resistance can be ignored. Thus a real Josephson junction can be modeled by an equivalent circuit consisting of an ideal junction shunted by a conductor.

2.2   dc-SQUID

A superconducting quantum interference device (SQUID) is a superconducting loop interrupted by one (rf-SQUID) or two (dc-SQUID) Josephson junctions, and biased by a magnetic flux. Here, we only introduce the dc-SQUID, which is a fundamental building block of the superconducting circuits discussed in the following chapters.

As shown in Fig. 2.2, a dc-SQUID can be described by two junctions shunted together. The junction J_i ($i = 1, 2$) has a Josephson energy E_i, a critical current I_{ci}, and a phase difference φ_i, and the current flowing through the junction J_i is I_i. Thus the total current of the dc-SQUID I can be expressed as

$$I = I_1 + I_2 = I_{c1}\cos\varphi_1 + I_{c2}\cos\varphi_2. \tag{2.7}$$

The total flux threading the dc-SQUID loop can be expressed as

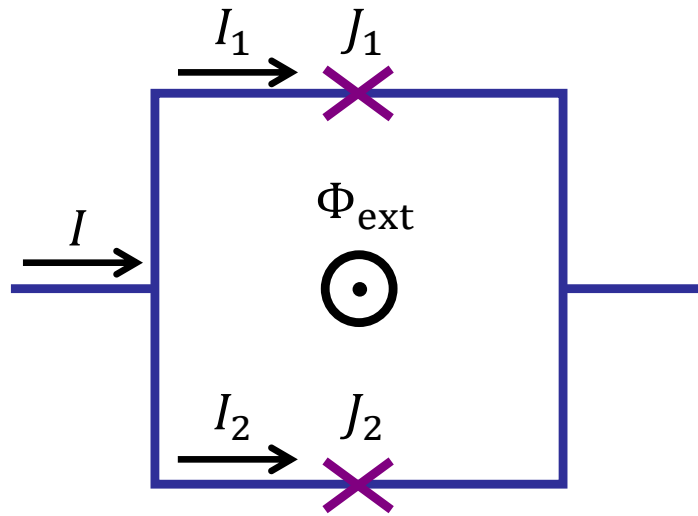$$\Phi_{\mathrm{tot}} = \Phi_{\mathrm{ext}} + L_{\mathrm{self}}I_{\mathrm{cir}}, \tag{2.8}$$

7

Figure 2.2: Schematic of a dc-SQUID. A dc-SQUID is a superconducting loop interrupted by two junctions J_i ($i = 1, 2$). The current flowing through the junction J_i is I_i, and the total current of the dc-SQUID is $I = I_1 + I_2$. An externally supplied magnetic flux Φ_{ext} threads the loop of the dc-SQUID.

where Φ_{ext} is the externally supplied flux, L_{self} is the self inductance of the dc-SQUID loop, and $I_{\mathrm{cir}} = (I_2 - I_1)/2$ is the circulating current of the loop. In practice, the inductance L_{self} is usually designed to be a very small value [26], thus we can ignore the term $L_{\mathrm{self}}I_{\mathrm{cir}}$ in Eq. (2.8) and assume $\Phi_{\mathrm{tot}} \approx \Phi_{\mathrm{ext}}$ in the following discussions. Using the flux quantization condition [26], we have

$$\varphi_1 - \varphi_2 = 2\pi \frac{\Phi_{\mathrm{ext}}}{\Phi_0} + 2n\pi, \tag{2.9}$$

where n is an integer. With the following variable transformation $\widetilde{\varphi} \equiv (\varphi_1 + \varphi_2)/2$, $I_{\mathrm{sum}} \equiv I_{c1} + I_{c2}$, $f \equiv \pi\Phi_{\mathrm{ext}}/\Phi_0$, and $d \equiv (I_{c1} - I_{c2})/(I_{c1} + I_{c2})$, the total current I in Eq. (2.7) can be expressed as

$$\begin{aligned} I &= I_{c1}\cos\varphi_1 + I_{c2}\cos\varphi_2 \\ &= I_{c1}\cos\left(\widetilde{\varphi} + f + n\pi\right) + I_{c2}\cos\left(\widetilde{\varphi} - f - n\pi\right) \\ &= I_{\mathrm{sum}}\cos\left(f + n\pi\right)\sqrt{1 + (d\tan f)^2}\sin\left(\widetilde{\varphi} - \varphi_0\right), \end{aligned} \tag{2.10}$$

with $\varphi_0 = \arctan(d\tan f)$. We can use the relation $\widetilde{\varphi} = \varphi_1 - f - n\pi$ to eliminate the dependence of n in the above equation. As a result, I can be given by

$$I = I_{\mathrm{sum}}\cos(f)\sqrt{1 + d^2\tan^2 f}\sin\left(\varphi_1 - f - \varphi_0\right). \tag{2.11}$$

Similarly, the total energy of the dc-SQUID, $E = -E_1\cos\varphi_1 - E_2\cos\varphi_2$, is given by

$$E = -E_{\mathrm{sum}}\cos(f)\sqrt{1 + d^2\tan^2 f}\cos\left(\varphi_1 - f - \varphi_0\right), \tag{2.12}$$

with $E_{\mathrm{sum}} = E_1 + E_2 = \Phi_0 I_{\mathrm{sum}}/2\pi$. Thus the dc-SQUID can be regarded as a tunable Josephson junction with the critical current I_{sq} and Josephson energy E_{sq} given by

$$E_{\mathrm{sq}} = \frac{\Phi_0}{2\pi}I_{\mathrm{sq}} = E_{\mathrm{sum}}|\cos f|\sqrt{1 + d^2\tan^2 f}. \tag{2.13}$$

Now we make a comparison between the symmetric dc-SQUID ($E_{c1} = E_{c2}$) and the asymmetric dc-SQUID ($E_{c1} \neq E_{c2}$). As shown in Fig. 2.3, the Josephson energies of a symmetric dc-SQUID (red) and an asymmetric dc-SQUID (blue) are plotted with respected to the reduced external flux f, in which both the SQUIDs have the same E_{sum}. We find that the symmetric dc-SQUID has a better tunability than the asymmetric one: The E_{sq} of a symmetric dc-SQUID can be tuned from E_{sum} to zero; while the E_{sq} of an asymmetric dc-SQUID can only be tuned from E_{sum} to $|E_1 - E_2|$.
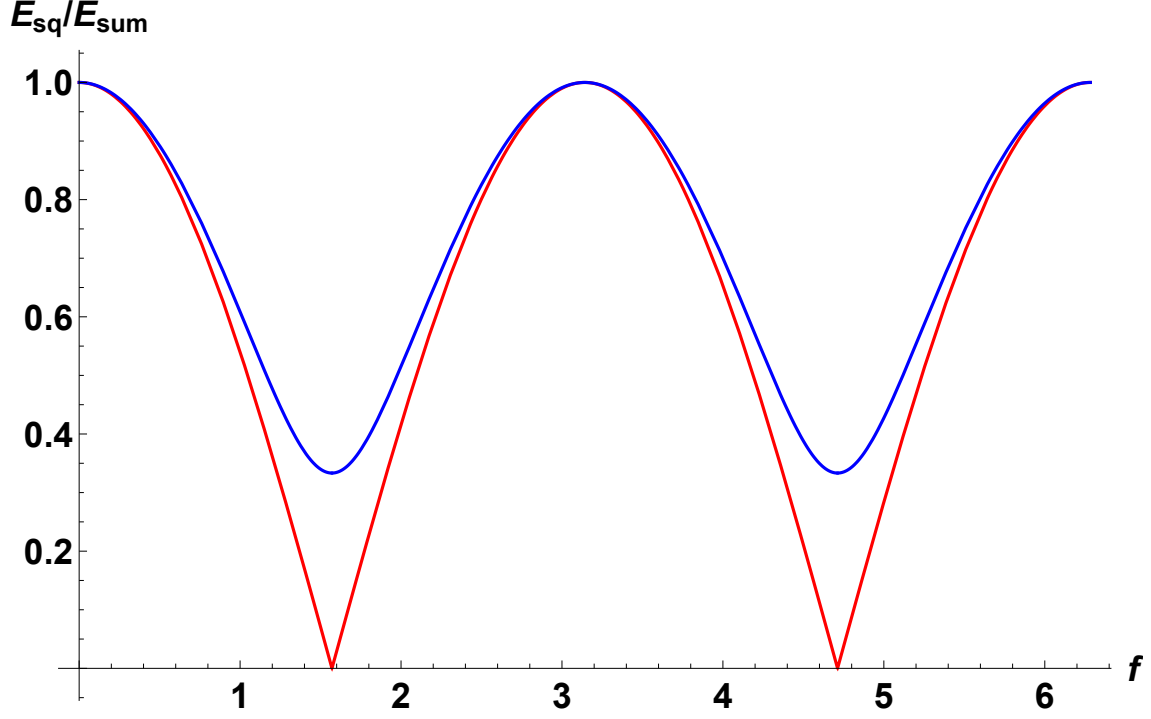
Figure 2.3: The Josephson energies E_{sq} of a symmetric dc-SQUID (red) and an asymmetric dc-SQUID (blue) are plotted with respected to the reduced external flux f. For the symmetric dc-SQUID, $E_1 = E_2 = E_{\text{sum}}/2$. For the asymmetric dc-SQUID, $E_1 = 2E_2 = 2E_{\text{sum}}/3$.

On the contrary, the asymmetric dc-SQUID is less sensitive to flux noise than the symmetric one. First, we note that $\partial E_{\text{sq}}/\partial f = 0$ when an asymmetric dc-SQUID is tuned to either its maximum or minimum E_{sq}. These points are called *sweet spots* because the dc-SQUID has the minimum sensitivity to flux noise at these points. The symmetric dc-SQUID, however, only reaches sweet spots when tuned to its maximum E_{sq}, which is a shortcoming compared with a asymmetric dc-SQUID. In addition, when both the dc-SQUIDs are tuned to the same E_{sq}, the value $|\partial E_{\text{sq}}/\partial f|$ of the asymmetric dc-SQUID is smaller than that of the symmetric one. That is to say, the asymmetric dc-SQUID has a better resilience to flux noise at this certain E_{sq}. Thus it is preferred to use an asymmetric dc-SQUID, as long as its range of E_{sq} satisfies our requirements.

10
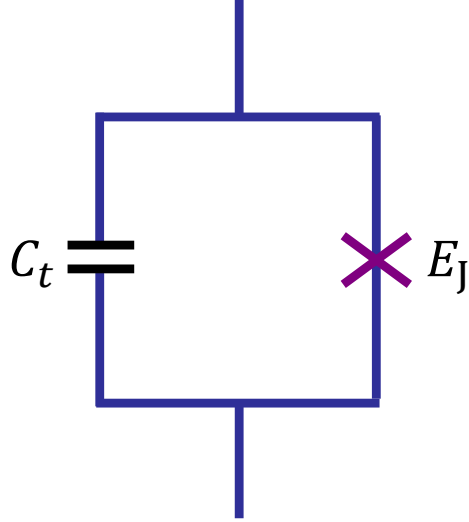
Figure 2.4: Electrical circuit of a transmon qubit. A transmon qubit consists of a Josephson junctions with the Josephson energy E_J and a large shunting capacitor C_t.

2.3 Transmon and Xmon

The transmon qubit [27, 28] consists of a Josephson junctions with the Josephson energy E_J and a large shunting capacitor C_t (as shown in Fig. 2.4). The Hamiltonian of a transmon qubit can be given by

$$H_t = 4E_\mathrm{C}n^2 - E_\mathrm{J}\cos\varphi, \tag{2.14}$$

where $E_\mathrm{C} = e^2/(2C_t)$. Here, the generalized coordinate φ is the phase difference across the junction, and the generalized momentum n is the number of Cooper pairs stored in the capacitor. These two operators follow the commutation relation $[\varphi, n] = i$. By shunting a large capacitance C_t, the transmon works in the regime $E_\mathrm{J}/E_\mathrm{C} \gg 1$, which makes the transmon insensitive to the change of charge, and thus reduces the effects of charge noise. In addition, in the regime of $E_\mathrm{J}/E_\mathrm{C} \gg 1$, we can expand $\cos\varphi$ at $\varphi = 0$ and keep up to 4th order terms of φ. As a result, the Hamiltonian in Eq. (2.14) is approximately given as

$$H_t \approx \hbar\omega_t a^\dagger a - \frac{E_\mathrm{C}}{2}a^\dagger a^\dagger aa, \tag{2.15}$$

where

$$\omega_t = \frac{1}{\hbar} \left(\sqrt{8E_{\mathrm{J}}E_{\mathrm{C}}} - E_{\mathrm{C}} \right), \tag{2.16}$$

$$n = -\frac{i\beta}{\sqrt{2}}(a - a^\dagger), \tag{2.17}$$

$$\varphi = \frac{1}{\sqrt{2}\beta}(a + a^\dagger), \tag{2.18}$$

$$\beta = \left(\frac{E_{\mathrm{J}}}{8E_{\mathrm{C}}} \right)^{\frac{1}{4}}. \tag{2.19}$$

Usually, the junction in the transmon is replaced by a dc-SQUID. In this way, the frequency of the transmon can be tuned by the biasing flux of the dc-SQUID.

The Xmon [29] qubit is a transmon qubit specially designed for 2D fabrication techniques. It has the same Hamiltonian as that of a transmon, while its specially designed structure provides much efficiency in operation. As shown in Fig, 2.5, Xmon is named by its crossing pad formed by two superconducting coplanar waveguide lines, where a grounded dc-SQUID is connected to one arm of the crossing pad. A flux biasing line is coupled inductively with the dc-SQUID for frequency tuning. The capacitor formed between the crossing pad and the ground serves as the large capacitor shunted to the Josephson junctions in the transmon qubit. The line for XY control of the Xmon is capacitively coupled to the crossing pad, which can be placed near the arm with dc-SQUID, or be placed by the other three arms of the crossing pad. The rest arms of the crossing pad can capacitively couple with other qubits or resonators. With this design, the tuning, control, coupling, and readout of Xmon can be individually operated and optimized.

2.4   Summary

In this chapter, we introduce the basic building blocks of superconducting circuits: the Josephson junction, the dc-SQUID, the transmon qubit, and the Xmon qubit. In the following three chapters, we focus on specific topics of superconducting circuits. In Ch. 3 and Ch. 4, we use the Xmon qubit to realize tunable coupling between two resonators. In Ch. 5, we study impedance engineering of a JPA, in which the JPA is made by a Josephson junction (or a dc-SQUID) shunted with a capacitor.
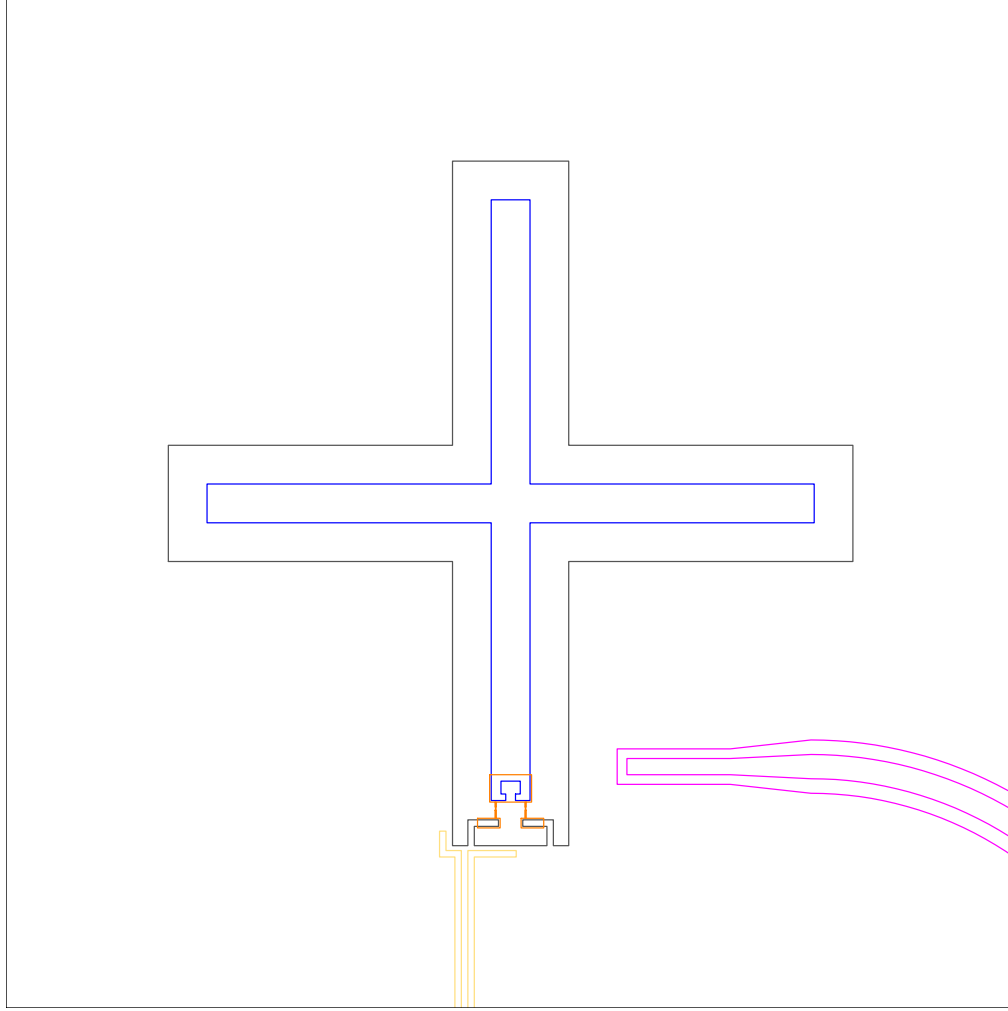
Figure 2.5: Chip layout of an Xmon qubit. An Xmon qubit consists of a crossing pad (blue) and a grounded dc-SQUID (orange) connected to one arm of the crossing pad. A flux biasing line (yellow) is coupled inductively with the dc-SQUID for frequency tuning. The XY control line (purple) is capacitively coupled to the crossing pad. The rest three arms of the crossing pad can capacitively couple with other qubits or resonators.

Chapter 3

Xmon as a tunable coupler between two resonators

In this and the next chapter, we study the tunable coupler for resonators. In this chapter, we focus on the theoretical model of the tunable coupler. In the next chapter, we shall discuss design, simulation, and fabrication of the tunable coupler.

3.1 Introduction

A tunable coupling between superconducting qubits or resonators is the basis for constructing two-qubit gates and realizing large scale quantum computers. A coupler interacting with two superconducting quantum elements (qubits or resonators) simultaneously can generate an effective coupling between the two elements. Various types of coupler have been studied [30, 31, 32, 33], in which the two elements are coupled via inductive, capacitive, or galvanic interactions.

In Ref. [34] and Ref. [35], two groups of researchers proposed using the transmon qubit as a tunable coupler. In Ref. [34], this coupler is used to realize two-qubit gates between two superconducting qubits and this proposal was demonstrated in experiments later [36]. On the contrary, in Ref. [35], this coupler is proposed to realize two-qubit gates between two resonators.

The key feature of this coupler is that it possesses a turn-off point where the interaction between the two elements (superconducting qubits or resonators) can be cancelled even they are at the same frequency. As more and more superconducting qubits are integrated

in the same chip, the frequency domain gets crowded, and the conventional way to turn off interactions between qubits by tuning their frequency away from each other is not feasible. Thus this tunable coupler has great potential for large scale quantum information processing.

In this and the next chapter, we study the tunable coupler for resonators proposed in Ref. [35], with the aim of experimentally realizing this coupler. In this chapter, we focus on the theoretical model of the tunable coupler. The contents are organized as follows. In Sec. 3.2, we introduce the principle of tunable coupling according to the derivations in Refs. [34, 35]. In Sec. 3.3, we present a specific chip design of the tunable coupler and derive the corresponding Hamiltonian using the formal circuit quantization method. In Sec. 3.4, we summary this chapter.

3.2   Hamiltonian of the tunable coupler

As shown in Fig. 3.1, the tunable coupler system consists of two superconducting resonators and one Xmon coupler. Hereafter we denote the tunable coupler as the resonator-Xmon-resonator (RXR) system. The two resonators R_a and R_b couple to each other with a coupling strength g_{ab}, and each couple to the Xmon with a coupling strength g_a and g_b, respectively. Here we regard the Xmon as a qubit consisting of its two lowest energy levels with a tunable angular frequency ω_x. In this case, the Hamiltonian H of the RXR system is given by [34, 35]

$$
\begin{aligned}
H/\hbar = {} & \omega_a a^\dagger a + \omega_b b^\dagger b + \omega_x \sigma^\dagger \sigma + g_{ab}(a^\dagger b + ab^\dagger - a^\dagger b^\dagger - ab) \\
& + g_a(a^\dagger \sigma + a\sigma^\dagger - a^\dagger \sigma^\dagger - a\sigma) + g_b(b^\dagger \sigma + b\sigma^\dagger - b^\dagger \sigma^\dagger - b\sigma).
\end{aligned} \tag{3.1}
$$

Here a and b are the annihilation operators of the resonant modes of R_a and R_b with angular frequencies ω_a and ω_b, respectively. And σ is the lowering operator defined in the eigenbasis of Xmon. The detuning between the Xmon and resonators is defined as $\Delta_i = \omega_i - \omega_x$ ($i = a, b$).

We note that in Eq. (3.1), not only the Jaynes-Cummings interaction terms (e.g., $[a^\dagger \sigma + a\sigma^\dagger]$), but also the counter-rotating terms (e.g., $[a^\dagger \sigma^\dagger + a\sigma]$) are kept. That is because, as will be shown below, the counter-rotating terms also make a significant contribution in the dispersive regime, which is comparable to that of the Jaynes-Cummings interaction terms.

Now, we discuss the effect of the Xmon when it is dispersively coupled to both of the two resonators, i.e., $g_i \ll |\Delta_i|$ ($i = a, b$). Following the derivation in Ref. [34], we apply
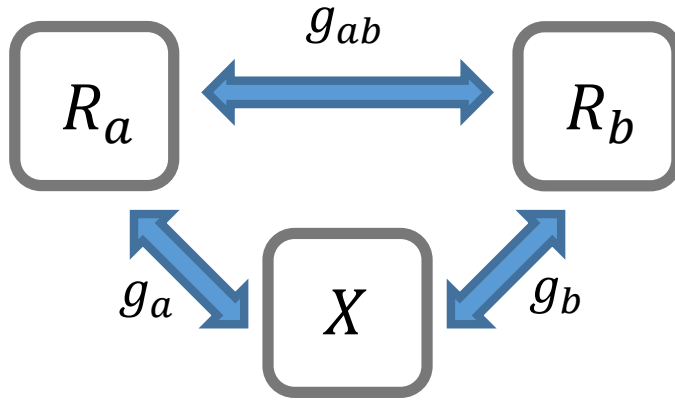
Figure 3.1: Schematic of the RXR system. The RXR system consists of two supercon-ducting resonators R_a and R_b, and an Xmon coupler denoted as "X". R_a and R_b couple to each other with a coupling strength g_{ab}. The Xmon couples to R_a (R_b) with a coupling strength g_a (g_b).

the following Schrieffer-Wolff transformation

$$U = \exp\left(\left[\frac{g_a}{\Delta_a}(a^\dagger\sigma - a\sigma^\dagger) - \frac{g_a}{\Sigma_a}(a^\dagger\sigma^\dagger - a\sigma)\right] + \left[\frac{g_b}{\Delta_b}(b^\dagger\sigma - b\sigma^\dagger) - \frac{g_b}{\Sigma_b}(b^\dagger\sigma^\dagger - b\sigma)\right]\right), \tag{3.2}$$

where $\Sigma_i = \omega_i + \omega_x$ ($i = a, b$). Expanding $UHU^\dagger$ with respect to $g_a^{k_a}g_b^{k_b}g_{12}^{k_{ab}}$ and keeping terms up to second order, i.e., $k_a + k_b + 2k_{ab} \leq 2$ (g_{ab} is assumed to a second-order quantity), the effective Hamiltonian $\widetilde{H}$ can be given by

$$\widetilde{H} = UHU^\dagger \approx \hbar\widetilde{\omega}_a a^\dagger a + \hbar\widetilde{\omega}_b b^\dagger b + \hbar\widetilde{g}_{ab}(a^\dagger b + ab^\dagger), \tag{3.3}$$

where

$$\widetilde{\omega}_a = \omega_a + g_a^2\left(\frac{1}{\Delta_a} - \frac{1}{\Sigma_a}\right), \tag{3.4}$$

$$\widetilde{\omega}_b = \omega_b + g_b^2\left(\frac{1}{\Delta_b} - \frac{1}{\Sigma_b}\right), \tag{3.5}$$

$$\widetilde{g}_{ab} = \frac{g_a g_b}{2}\left(\frac{1}{\Delta_a} + \frac{1}{\Delta_b} - \frac{1}{\Sigma_a} - \frac{1}{\Sigma_b}\right) + g_{ab}. \tag{3.6}$$

In Eq. (3.3), the Xmon is assumed to be in its ground state and the corresponding operators are eliminated. The indirect coupling between two resonators via a coupler in its ground state is called virtual exchange interaction [37]. We denote that the eigenstate of the RXR system without any interaction by $|n_a, m, n_b\rangle$, in which $m = g$ (or e) represents the ground (first-excited) state of Xmon, and n_i represents the Fock state of resonator R_i with $i = a, b$. Then, we find that the Jaynes-Cummings interaction terms ($[a^\dagger\sigma + a\sigma^\dagger]$ and $[b^\dagger\sigma + b\sigma^\dagger]$) in Eq. (3.1) enable the virtual interaction between the states $|n, g, n - 1\rangle$ and $|n-1, g, n\rangle$ through the state $|n-1, e, n-1\rangle$. On the other hand, the counter-rotating terms ($[a^\dagger\sigma^\dagger + a\sigma]$ and $[b^\dagger\sigma^\dagger + b\sigma]$) enable the virtual interaction between the states $|n, g, n-1\rangle$ and $|n - 1, g, n\rangle$ through the state $|n, e, n\rangle$. In the dispersive regime, $|\Delta_i| \approx |\Sigma_i|$, the counter-rotating terms also make a significant contribution to the virtual interaction between two resonators and should not be ignored.

Assuming $\omega_a = \omega_b = \omega_r = \omega_x/r$, the coupling strength $\widetilde{g}_{ab}$ in Eq. (3.6) can be expressed as

$$\widetilde{g}_{ab} = \frac{r}{1 - r^2}\frac{2g_a g_b}{\omega_r} + g_{ab}. \tag{3.7}$$

According to Refs. [34, 35], we have the following conclusions about Eq. (3.7):

17

(1) For a given resonator frequency ω_r, g_a and g_b are dependent of r, while g_{ab} is independent of r. Thus the total coupling strength $\widetilde{g}_{ab}$ can be tuned by changing r, i.e., by changing the frequency ω_x of the Xmon.

(2) When r is tuned to a certain value $r_{\text{off}} > 1$, we have $\widetilde{g}_{ab} = 0$. That is to say, when the frequency of Xmon is tuned to $\omega_x = r_{\text{off}} \omega_r$, the coupling between R_a and R_b can be turned off.

In the next section, we will derive the specific expressions for g_a, g_b, g_{ab}, and discuss the above conclusions in details.

3.3 Circuit implementation

In this section, we discuss the circuit implementation of the RXR system. The first version of the chip layout was finished by Carolyn Earnest and Jeremy Bejanin. Then we modified this chip layout to comply with our design and fabrication requirements, and finally completed the final version of the chip layout.

In Fig. 3.2, we present the final version of our chip layout. An Xmon, accompanied by a flux biasing line and an XY control line, stays at the center of the chip and capacitively couples to three $\lambda/4$ resonators R_a, R_b, and R_m through its crossing pad. Resonators R_a and R_b have the same resonant frequency ω_r, while R_m has a resonant frequency ω_m largely detuned from ω_r. On the left side of the chip, a pump line is used to excite the resonant modes of R_a though capacitive coupling. On the right side of the chip, a readout line is used to probe the resonant modes of R_b and R_m though capacitive coupling.

Fig. 3.3 shows an enlarged view of the Xmon area in Fig. 3.2, in which the resonators couple to the Xmon's crossing pad via "claws". A direct capacitance between the claws of R_a and R_b enables the coupling between these two resonators. Similarly, the resonator R_m also couples with R_a (R_b) via direct capacitances between their claws. These perturbations from R_m will also be considered in the following derivation.

As illustrated in Sec. 3.2, the Xmon and the flux biasing line, together with the two resonators R_a and R_b, make up the essential elements of a RXR system with tunable coupling. The XY control line, the resonator R_m, the pump line, and the readout line are added as ancillary elements to characterize the RXR system. The XY control line is used to manipulate the state of the Xmon. R_m is used to readout the state of the Xmon. The pump line is used to excite the resonator R_a, and the readout line is used to detect the states of R_b and R_m.
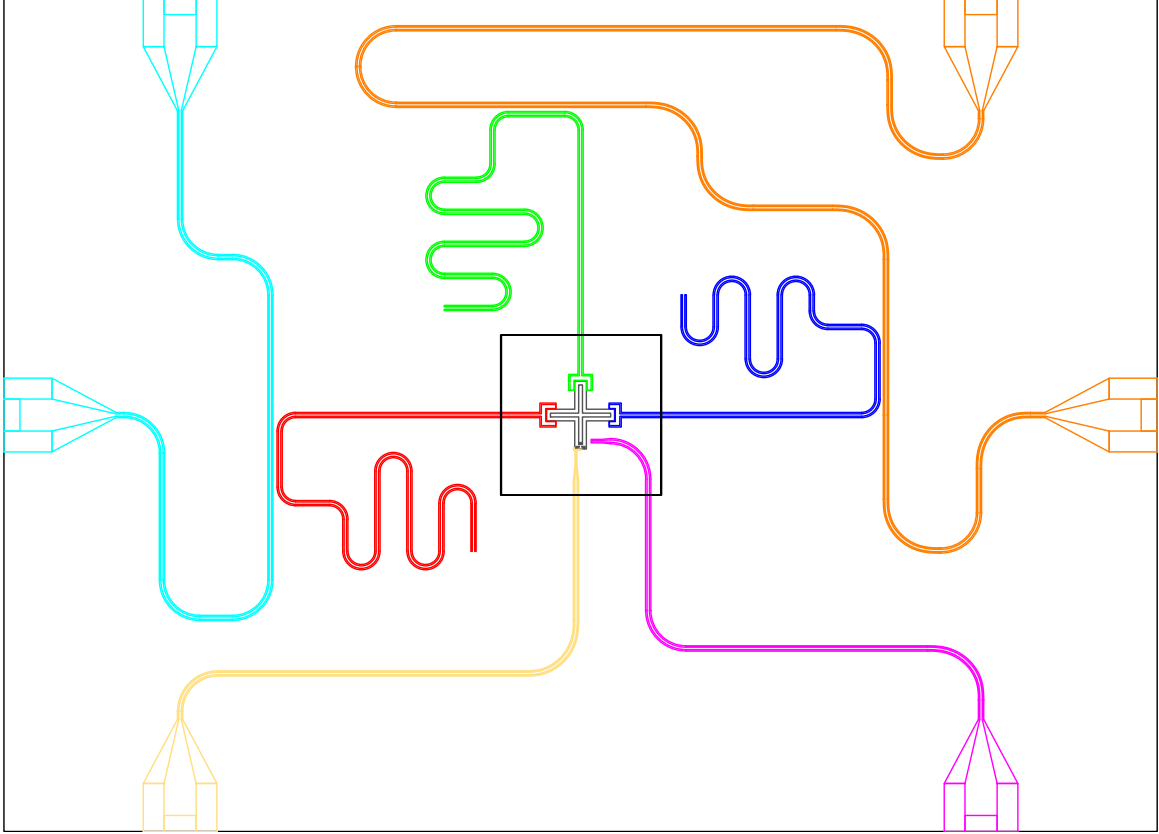
Figure 3.2: Chip layout of the RXR system. An Xmon (black crossing), accompanied by a flux line (yellow) and an XY line (purple), stays at the center of the chip and capacitively couples to three resonators R_a (red), R_b (green), and R_m (blue). A pump line (light blue) is located on the left side of the chip. A readout line (orange) is on the right side of the chip. An enlarged view of the Xmon area (black dashed rectangle) is shown in Fig. 3.3.
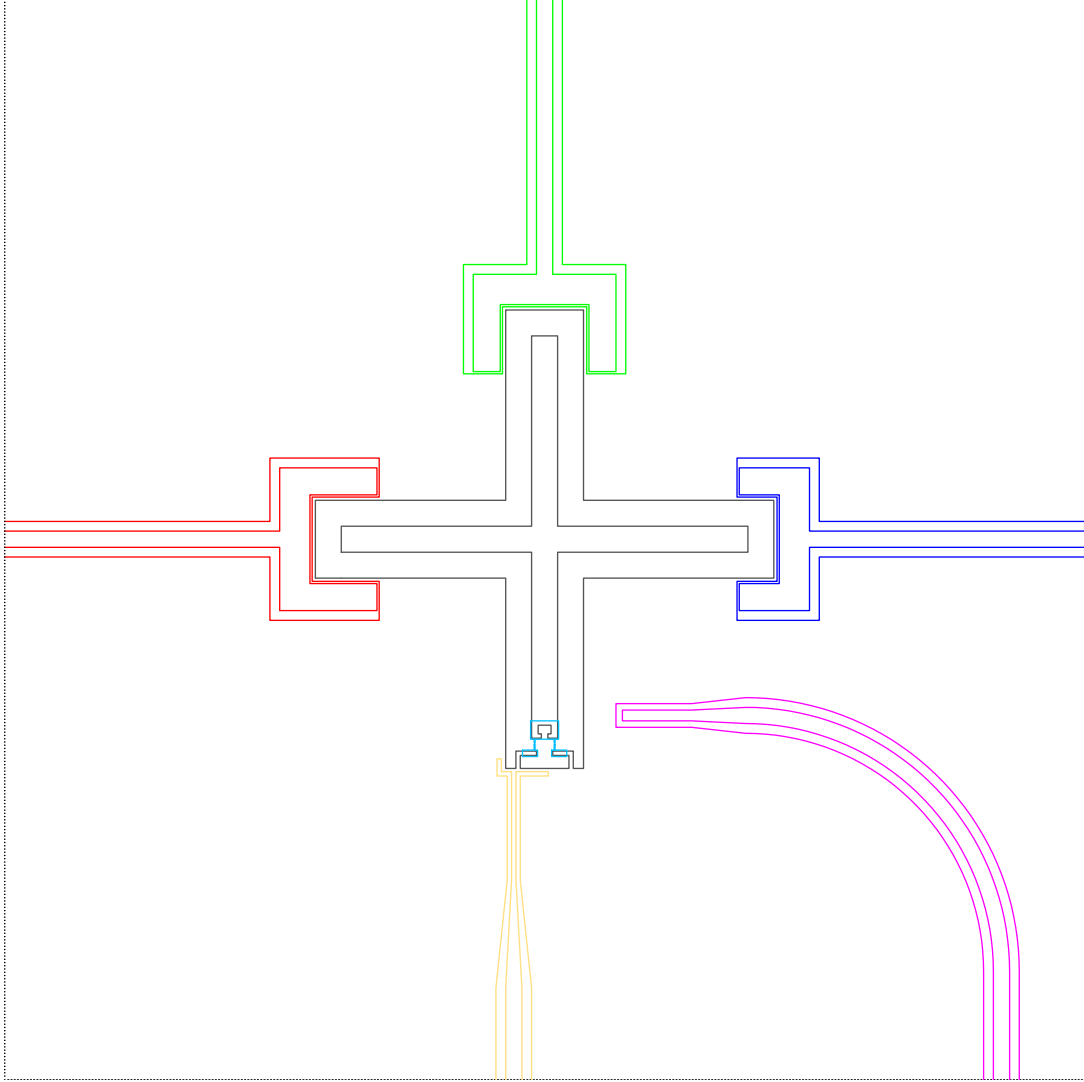
Figure 3.3: Enlarged view of the Xmon area (black dashed rectangle in Fig. 3.2). The Xmon is capacitively coupled with R_a (red), R_b (green), R_m (blue), and the XY control line (purple) through its crossing pad. The flux biasing line (yellow) is inductively coupled with the dc-SQUID (light blue) of the Xmon.
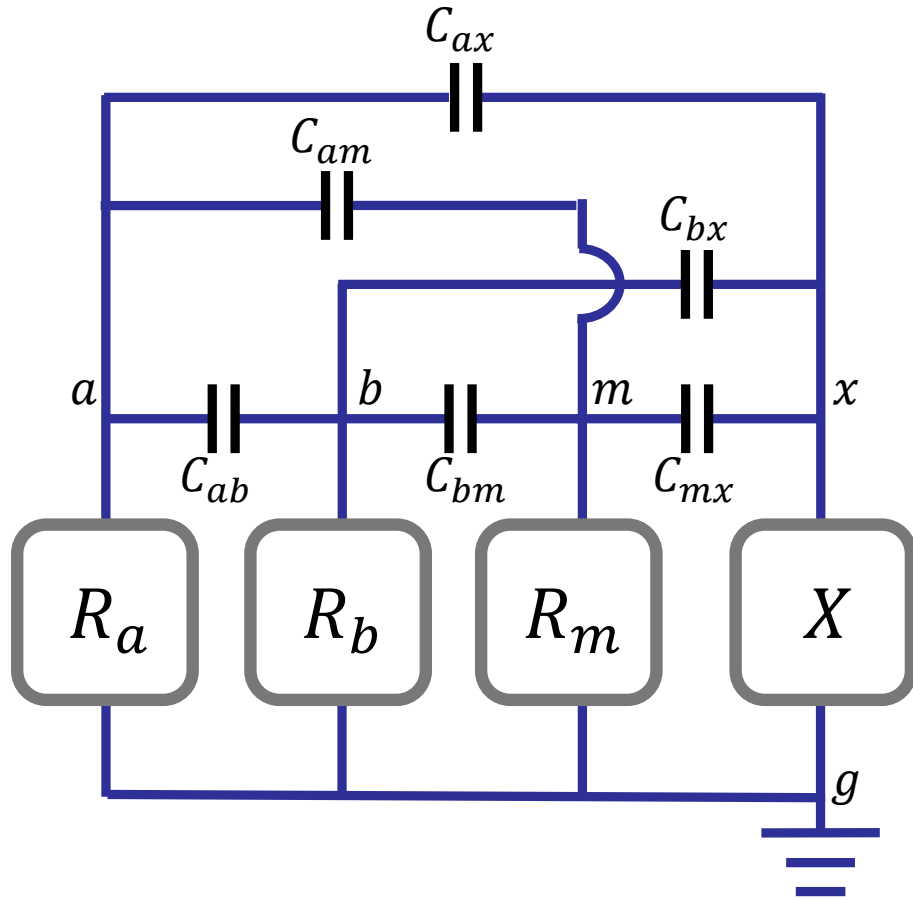
Figure 3.4: Circuit diagram of the RXR system. R_a, R_b, R_m, and the Xmon (denoted by "X") are coupled with each other. Each two of these four circuit elements are linked by a coupling capacitor C_{ij} ($i, j = a, b, m, x$ and $i < j$). The five nodes of the circuit are labeled by a, b, m, x, g, respectively

Based on the chip layout of the RXR system, the corresponding circuit diagram is shown in Fig. 3.4. The resonators R_i are modeled by LC oscillators with inductances L_i and capacitors C_i ($i = a, b, m$), respectively. While the Xmon is modeled by a Josephson junction shunted with a capacitor C_x. The Josephson junction has a tunable Josephson energy E_{jx}, and its capacitance has been merged into C_x for simplicity. Each two of the above four circuit elements are linked by a coupling capacitor C_{ij} ($i, j = a, b, m, x$ and $i < j$). Here the labels a, b, m, x represent R_a, R_b, R_m, and the Xmon respectively, with the order $a < b < m < x$.

Note that only the Xmon and the resonators R_i ($i = a, b, m$) are taken into consideration in Fig. 3.4, for which the total Hamiltonian H_{tot} is what we are concerned with. The effect of the flux line has been incorporated into the tunability of the Josephson energy E_{jx}. The XY, pump, and readout lines, which can be treated as external driving terms coupled to H_{tot}, are not included in the circuit diagram.

To characterize the property of our chip, we need to derive the Hamiltonian H_{tot}. Our aim is twofold. First, as we introduce a new component R_m into the circuit, the original Hamiltonian H in Eq. (3.1) is not applicable for our RXR system. Second, from the chip layout we can only get the electromagnetic (EM) parameters such as L_i, C_i, and C_{ij} ($i, j = a, b, m, x$). We need to express H_{tot} as a function of these EM parameters.

To achieve the above aim, we use the formal circuit quantization method to derive H_{tot}. Following the formalism in Ref. [38], the five nodes of the circuit are labeled by a, b, m, x, g, respectively (see Fig. 3.4). The fluxes of these five circuit nodes are denoted by ϕ_i ($i = a, b, m, x, g$). Without loss of generality, the ground node flux ϕ_g is assumed to be zero, and the rest four node fluxes are chosen as the generalized coordinates of the circuit. The kinetic energy, T, and the potential energy, U, of the circuit can be given by

$$T = \frac{1}{2} \Big[C_a \dot{\phi}_a^2 + C_b \dot{\phi}_b^2 + C_m \dot{\phi}_m^2 + C_x \dot{\phi}_x^2 + C_{ax}(\dot{\phi}_a - \dot{\phi}_x)^2 + C_{bx}(\dot{\phi}_b - \dot{\phi}_x)^2 + C_{mx}(\dot{\phi}_m - \dot{\phi}_x)^2$$
$$+ C_{ab}(\dot{\phi}_a - \dot{\phi}_b)^2 + C_{am}(\dot{\phi}_a - \dot{\phi}_m)^2 + C_{bm}(\dot{\phi}_b - \dot{\phi}_m)^2 \Big], \tag{3.8}$$

and

$$U = \frac{\phi_a^2}{2L_a} + \frac{\phi_b^2}{2L_b} + \frac{\phi_m^2}{2L_m} + E_{jx} \cos\left(\frac{2\pi}{\Phi_0}\phi_x\right), \tag{3.9}$$

respectively.

Equation (3.8) can be written in vector form as $T = \frac{1}{2}\dot{\vec{\phi}}^T \mathbb{C} \dot{\vec{\phi}}$, where $\vec{\phi} = [\phi_a, \phi_b, \phi_m, \phi_x]$

and $\mathbb{C}$ is the capacitance matrix. The expression for $\mathbb{C}$ is

$$\mathbb{C} = \begin{bmatrix} \mathbb{C}_{11} & -C_{ab} & -C_{am} & -C_{ax} \\ -C_{ab} & \mathbb{C}_{22} & -C_{bm} & -C_{bx} \\ -C_{am} & -C_{bm} & \mathbb{C}_{33} & -C_{mx} \\ -C_{ax} & -C_{bx} & -C_{mx} & \mathbb{C}_{44} \end{bmatrix}, \tag{3.10}$$

where the diagonal elements are given by

$$\begin{aligned} \mathbb{C}_{11} &= C_a + C_{ab} + C_{am} + C_{ax} \\ \mathbb{C}_{22} &= C_{ab} + C_b + C_{bm} + C_{bx} \\ \mathbb{C}_{33} &= C_{am} + C_{bm} + C_m + C_{mx} \\ \mathbb{C}_{44} &= C_{ax} + C_{bx} + C_{mx} + C_x. \end{aligned} \tag{3.11}$$

With the Lagrangian of the circuit $L = T - U$, the generalized momenta q_i, which are the node charges, are given by

$$q_i = \frac{\partial L}{\partial \dot{\phi}_i}, \;\; (i = a, b, m, x). \tag{3.12}$$

Eq. (3.12) can be written in vector form as $\vec{q} = \mathbb{C}\dot{\vec{\phi}}$, where $\vec{q} = [q_a, q_b, q_m, q_x]$. The classical Hamiltonian can be expressed as

$$H_{\text{cla}} = \vec{q} \cdot \dot{\vec{\phi}} - L = \frac{1}{2}\vec{q}^{\,T}\mathbb{C}^{-1}\vec{q} + U = T' + U, \tag{3.13}$$

where $\mathbb{C}^{-1}$ is the inverse matrix of $\mathbb{C}$. The term T' is the kinetic energy T rewritten as a function of the generalized momenta, which can be expanded with respect to $q_i q_j$ as

$$T' = \sum_i \frac{q_i^2}{2\widetilde{C}_i} + \sum_{i<j} \frac{q_i q_j}{\widetilde{C}_{ij}}, \;\; (i, j = a, b, m, x). \tag{3.14}$$

Here $\widetilde{C}_i$ and $\widetilde{C}_{ij}$ are positive quantities with a dimension of capacitance.

Using Eq. (3.9), Eq. (3.13), and Eq. (3.14), the quantum-mechanical Hamiltonian H_{tot} of the circuit can be derived via canonical quantization,

$$H_{tot} = H_a + H_b + H_m + H_x + \sum_{i<j} H_{ij}. \tag{3.15}$$

23

In Eq. (3.15), H_i ($i = a, b, m$) are the Hamiltonian of R_a, R_b, R_m, respectively,

$$H_a = \frac{q_a^2}{2\widetilde{C}_a} + \frac{\phi_a^2}{2L_a} = \hbar\omega_a a^\dagger a, \tag{3.16}$$

$$H_b = \frac{q_b^2}{2\widetilde{C}_b} + \frac{\phi_b^2}{2L_b} = \hbar\omega_b b^\dagger b, \tag{3.17}$$

$$H_m = \frac{q_m^2}{2\widetilde{C}_m} + \frac{\phi_m^2}{2L_m} = \hbar\omega_m m^\dagger m, \tag{3.18}$$

where $\omega_i = 1/\sqrt{L_i\widetilde{C}_i}$, and m is the annihilation operator of the resonant mode of R_m. H_x is the Hamiltonian of the Xmon given in Eq. (2.14), which can be approximately treated as a weakly anharmonic oscillator denoted by the annihilation operator c,

$$H_x = \frac{q_x^2}{2\widetilde{C}_x} + E_{jx}\cos\left(\frac{2\pi}{\Phi_0}\phi_x\right) = 4E_{cx}n_x^2 - E_{jx}\cos\varphi_x$$

$$\approx \hbar\omega_x c^\dagger c - \frac{E_{cx}}{2}c^\dagger c^\dagger cc. \tag{3.19}$$

Here $n_x \equiv q_x/(2e)$, $\varphi_x \equiv 2\pi\phi_x/\Phi_0$, $E_{cx} \equiv e^2/(2\widetilde{C}_x)$, and ω_x is given by

$$\omega_x = \frac{1}{\hbar}\left(\sqrt{8E_{jx}E_{cx}} - E_{cx}\right). \tag{3.20}$$

The last term in Eq. (3.15) represents the interactions between the above four circuit elements,

$$H_{ij} = \frac{q_i q_j}{\widetilde{C}_{ij}}, \tag{3.21}$$

where $i, j = a, b, m, x$ and $i < j$.

In Eqs. (3.16–3.21), q_i and ϕ_i are quantum operators satisfying the following relations

$$q_a = -i\sqrt{\frac{\hbar}{2Z_a}}(a - a^\dagger), \ \phi_a = \sqrt{\frac{\hbar Z_a}{2}}(a + a^\dagger), \tag{3.22}$$

$$q_b = -i\sqrt{\frac{\hbar}{2Z_b}}(b - b^\dagger), \ \phi_b = \sqrt{\frac{\hbar Z_b}{2}}(b + b^\dagger), \tag{3.23}$$

$$q_m = -i\sqrt{\frac{\hbar}{2Z_m}}(m - m^\dagger), \ \phi_m = \sqrt{\frac{\hbar Z_m}{2}}(m + m^\dagger), \tag{3.24}$$

$$q_x = 2en_x = -i\sqrt{\frac{\hbar}{2Z_x}}(c - c^\dagger), \ \phi_x = \frac{\Phi_0}{2\pi}\varphi_x = \sqrt{\frac{\hbar Z_x}{2}}(c + c^\dagger), \tag{3.25}$$

where $Z_i = \sqrt{L_i/\widetilde{C}_i}$ $(i = a, b, m, x)$ and $L_x = (\frac{\Phi_0}{2\pi})^2/E_{jx}$.

Comparing H_{tot} in Eq. (3.15) with H in Eq. (3.1), we can find the effects of R_m are twofold. (1) The capacitive coupling between R_m and R_a (R_b) results in the interaction term H_{am} (H_{bm}). As R_m is designed largely detuned from R_a and R_b, the effects of H_{am} and H_{bm} are suppressed. (2) As R_b is located nearer to R_m than R_a (see Fig. 3.2(b)), we have $C_{bm} > C_{am}$. This asymmetry will lead to $\omega_a \neq \omega_b$ even if the RXR system is designed symmetrically (i.e., $L_a = L_b$, $C_a = C_b$, and $C_{ax} = C_{bx}$).

Now, we derive the expressions for the coupling strengths g_a, g_b, and g_{ab} introduced in Eq. (3.1). For the interaction between the Xmon and R_a (R_b), the corresponding term is

$$
\begin{aligned}
H_{ax} &= \frac{q_a q_x}{\widetilde{C}_{ax}} = \frac{1}{\widetilde{C}_{ax}} \frac{\hbar}{\sqrt{4Z_a Z_x}} (a^\dagger c + a c^\dagger - a^\dagger c^\dagger - ac) \\
&\approx \frac{1}{\widetilde{C}_{ax}} \frac{\hbar}{\sqrt{4Z_a Z_x}} (a^\dagger \sigma + a \sigma^\dagger - a^\dagger \sigma^\dagger - a\sigma),
\end{aligned}
\tag{3.26}
$$

$$
\begin{aligned}
H_{bx} &= \frac{q_b q_x}{\widetilde{C}_{bx}} = \frac{1}{\widetilde{C}_{bx}} \frac{\hbar}{\sqrt{4Z_b Z_x}} (b^\dagger c + b c^\dagger - b^\dagger c^\dagger - bc) \\
&\approx \frac{1}{\widetilde{C}_{bx}} \frac{\hbar}{\sqrt{4Z_b Z_x}} (b^\dagger \sigma + b \sigma^\dagger - b^\dagger \sigma^\dagger - b\sigma).
\end{aligned}
\tag{3.27}
$$

Here, we treat the Xmon as a weakly anharmonic oscillator and only consider its lowest two levels. The expressions for g_a and g_b are thus given by

$$
g_a = \frac{1}{\widetilde{C}_{ax}\sqrt{4Z_a Z_x}},
\tag{3.28}
$$

$$
g_b = \frac{1}{\widetilde{C}_{bx}\sqrt{4Z_b Z_x}}.
\tag{3.29}
$$

For the interaction between R_a and R_b, the corresponding term is

$$
H_{ab} = \frac{q_a q_b}{\widetilde{C}_{ab}} = \frac{1}{\widetilde{C}_{ab}} \frac{\hbar}{\sqrt{4Z_a Z_b}} (a^\dagger b + a b^\dagger - a^\dagger b^\dagger - ab).
\tag{3.30}
$$

Thus the expression for g_{ab} is

$$
g_{ab} = \frac{1}{\widetilde{C}_{ab}\sqrt{4Z_a Z_b}}.
\tag{3.31}
$$

Now we revisit $\widetilde{g}_{ab}$ in Eq. (3.7) to discuss the tunable coupling between R_a and R_b. Here we ignore the effects of R_m, and assume the RXR system is designed symmetrically.

25

In this case, we have $L_a = L_b$, $\widetilde{C}_a = \widetilde{C}_b = \widetilde{C}_r$, $\widetilde{C}_{ax} = \widetilde{C}_{bx}$, $\omega_a = \omega_b = \omega_r$, and $Z_a = Z_b$. Using the above relations, $\widetilde{g}_{ab}$ can be expressed as

$$\widetilde{g}_{ab} = \frac{r^2}{2(1-r^2)} \frac{\widetilde{C}_r \widetilde{C}_x}{\widetilde{C}_{rx}^2} \omega_r + \frac{\widetilde{C}_r}{2\widetilde{C}_{ab}} \omega_r, \tag{3.32}$$

where $r \equiv \omega_x/\omega_r$. In deriving Eq. (3.32), we make the approximation that

$$\omega_x = \frac{1}{\hbar} \left(\sqrt{8E_{jx}E_{cx}} - E_{cx} \right) \approx \frac{\sqrt{8E_{jx}E_{cx}}}{\hbar}, \tag{3.33}$$

which is valid due to $E_{jx} \gg E_{cx}$ for an Xmon qubit. Using Eq. (3.32), we can derive the turn-off ratio r_{off} such that $\widetilde{g}_{ab} = 0$,

$$r_{\text{off}} = \frac{\widetilde{C}_{rx}}{\sqrt{\widetilde{C}_{rx}^2 - \widetilde{C}_{ab}\widetilde{C}_x}}. \tag{3.34}$$

That is to say, when ω_x is tuned to $\omega_{\text{off}} = r_{\text{off}}\omega_r$, the coupling between R_a and R_b can be turned off.

3.4 Summary

In this chapter, we introduce the theoretical model of the tunable coupler. By deriving the Hamiltonian H_{tot} of the RXR chip for implementing the coupler, we connect H_{tot} with the EM parameters of the RXR chip. In the next chapter, we shall obtain these EM parameters from the design and the fabrication parameters of the RXR chip, and construct the corresponding Hamiltonian H_{tot}. Then we verify whether the tunable coupling can be achieved on this chip from numerical simulating the energy spectrum of H_{tot}.

Chapter 4

Design, simulation & fabrication

In Chapter 3, we related the Hamiltonian of the RXR chip with the EM parameters of its circuit model. In this chapter, we focus on the design, the simulation, and the fabrication of that specific RXR chip, in which we obtain the EM parameters according to the layout design and the fabrication processes, and use them to simulate the Hamiltonian of the chip. In Sec. 4.1, we introduce design and simulation of the resonators. In Sec. 4.2, we obtain the coupling capacitances of the RXR chip from EM simulation. In Sec. 4.3, we introduce the design of the Josephson junctions in the Xmon. In Sec. 4.4, we calculate the eigenenergies and the eigenstates of the RXR chip. In Sec. 4.5, we summary this chapter.

4.1   Design of resonators

On the RXR chip (see Fig. 3.2), the pump line, the readout line, and the resonators R_a, R_b, and R_m are all implemented by the coplanar waveguide (CPW) transmission line. As shown in Fig. 4.1, the CPW consists of a central conducting line laying on a dielectric substrate, together with a pair of return conductors on both sides of the central line. The electrical properties of CPW is determined two factors. The first factor is the materials of the conductor and the substrate. For our chip, the conductor and the substrate is made with Al and Si, respectively. The EM properties of these two materials are shown in Table 4.1. The second factor is the geometric dimensions of the conductor and the substrate. According to our previous fabrication experience, the geometric dimensions of our CPW are chosen as follows: the central line width $W = 15$ μm, the gap width $G = 9$ μm, the conductor thickness $T = 78$ nm, and the substrate thickness $H = 500$ μm. As will be shown in the simulation below, these parameters satisfy our design requirements.

27
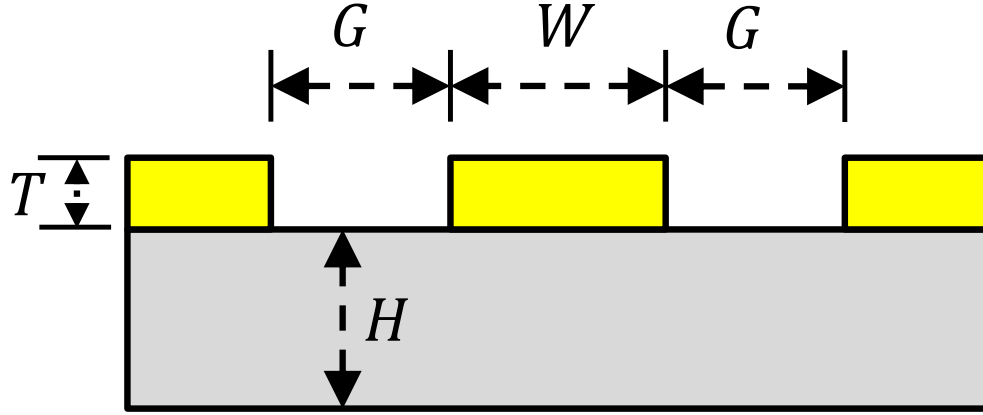
Figure 4.1: Cross section of coplanar waveguide transmission line. The CPW is made by a thin conductive film with thickness T, laying on a dielectric substrate with thickness H. The CPW consists of a central conducting line with width W, and a pair of return conductors on both sides of the central line. The width of the gap between the central line and each return conductor is denoted as G.

	Al (PEC)	Si
relative permittivity	1	11.9
relative permeability	1	1
dielectric loss tangent	0	0
Bulk conductivity	10^{30} S/m	0

Table 4.1: EM properties of Al and Si. The relative permittivity is also called as "dielectric constant". Here the temperature is assumed to be 0 K, and Al is treated as a perfect electric conductor (PEC). Data cited from the database of the EM simulation software *ANSYS HFSS*.

With the above parameters, the electrical properties of the CPW can be calculated using *ADS LineCalc*. We have the characteristic impedance $Z_0 = 49.7\ \Omega$ and the effective relative permittivity $\epsilon_{\text{eff}} = 6.42$. Using ϵ_{eff}, the phase speed in the CPW can be calculated,

$$v_p = \frac{c}{\sqrt{\epsilon_{\text{eff}}}} \approx 1.18 \times 10^8 \ \text{m/s}. \tag{4.1}$$

As the pump line and the readout line need to be connected to the input/measurement devices via cables, it is optimal for them to have a characteristic impedance close to the standard impedance $Z_{\text{std}} = 50\ \Omega$ to minimize the return loss. The resonators, however, are not necessarily required to have a standard impedance.

For our chip, our goal is to implement the resonators with $\lambda/4$ shorted CPW transmission lines, with the resonant frequency $\omega_a = \omega_b \approx 2\pi \times 5$ GHz and $\omega_m \approx 2\pi \times 5.5$ GHz. First we have a look at the parallel LC circuit, which is the prototype of the $\lambda/4$ shorted CPW resonator. For a parallel LC circuit, its total impedance is given by

$$Z_{\text{LC}}(\omega) = (\frac{1}{i\omega L} + i\omega C)^{-1} = -\frac{i}{C}\frac{\omega}{\omega^2 - \omega_0^2}, \tag{4.2}$$

where $\omega_0 = 1/\sqrt{LC}$ is the resonant frequency. We can find $Z_{\text{LC}}(\omega)$ goes to ∞ when ω approaches ω_0. Another useful relation is about C and the admittance $Y_{\text{LC}}(\omega) \equiv 1/Z_{\text{LC}}(\omega)$. Noting that

$$\frac{dY_{\text{LC}}(\omega)}{d\omega} = -\frac{1}{i\omega^2 L} + iC = iC\frac{\omega^2 + \omega_0^2}{\omega^2}, \tag{4.3}$$

the capacitance C can be expressed as

$$C = \frac{1}{2i} \frac{dY_{\text{LC}}(\omega)}{d\omega}\bigg|_{\omega=\omega_0}. \tag{4.4}$$

Now, we come back to the shorted CPW, for which the input impedance Z_{in} is given by

$$Z_{\text{in}}(\omega) = iZ_0 \tan(\beta l) = iZ_0 \tan(\frac{l}{v_p}\omega), \tag{4.5}$$

where $\beta = \omega/v_p$ is the phase constant and l is the length of the CPW. Similar to the parallel LC circuit, the resonant frequency ω_{res} is the frequency such that

$$\lim_{\omega \to \omega_{\text{res}}} Z_{\text{in}}(\omega) = \infty. \tag{4.6}$$

29

We readily find that

$$\omega_{\text{res}}(n) = \frac{v_p}{l}\frac{\pi}{2}(2n+1), \ (n = 0, 1, 2, ...). \tag{4.7}$$

Assuming $\omega_0 = \omega_{\text{res}}(0) = \pi v_p/(2l)$, the CPW is called a $\lambda/4$ resonator when $\omega = \omega_0$, because at this frequency l equals one quarter of the wavelength λ. Using Eq. (4.4), the effective capacitance of the $\lambda/4$ CPW resonator can be given by

$$C_{\text{eff}} = \frac{1}{2i}\frac{dY_{\text{in}}(\omega)}{d\omega}\bigg|_{\omega=\omega_0} = \frac{\pi}{4\omega_0 Z_0}, \tag{4.8}$$

where $Y_{\text{in}}(\omega) = 1/Z_{\text{in}}(\omega)$. Correspondingly, the effective inductance of the resonator is given by

$$L_{\text{eff}} = \frac{1}{\omega_0^2 C} = \frac{4Z_0}{\pi\omega_0}. \tag{4.9}$$

As shown in Fig. 4.2, a resonator consists of a regular CPW part and a claw. The length of the regular CPW part of R_a (R_m) is denoted as l_a (l_m). For our chip, we have $l_a = 5714\ \mu\text{m}$ and $l_m = 5164\ \mu\text{m}$. Using Eq. (4.7), we can calculate resonant frequencies of R_a and R_m,

$$\omega_a \approx \frac{\pi v_p}{2l_a} = 2\pi \times 5.18\ \text{GHz}, \tag{4.10}$$

$$\omega_m \approx \frac{\pi v_p}{2l_m} = 2\pi \times 5.73\ \text{GHz}. \tag{4.11}$$

The above calculation is a rough estimation because the effects of the claws of R_a and R_m are ignored. To obtain the parameters of resonators with more accuracy, we use the EM simulation software *ANSYS HFSS* to numerical simulate the resonators. As shown in Fig. 4.3, the impedance of R_a and R_m at different frequencies are plotted. The resonant frequencies can be obtained from the maximum points of the impedance curve,

$$\omega_a = 2\pi \times 4.9\ \text{GHz}, \tag{4.12}$$

$$\omega_m = 2\pi \times 5.57\ \text{GHz}. \tag{4.13}$$

The imaginary part of admittance of R_a and R_m at different frequency are plotted in Fig. 4.4. For the curve of R_a, the slope at the resonant frequency is $s_a = 0.008\ (\Omega\cdot\text{GHz})^{-1}$. Accordingly, for R_m the slope is $s_m = 0.0065\ (\Omega\cdot\text{GHz})^{-1}$. Noting the following relations

$$\text{Im}(Y_{\text{in}}) = Y_{\text{in}}/i \tag{4.14}$$
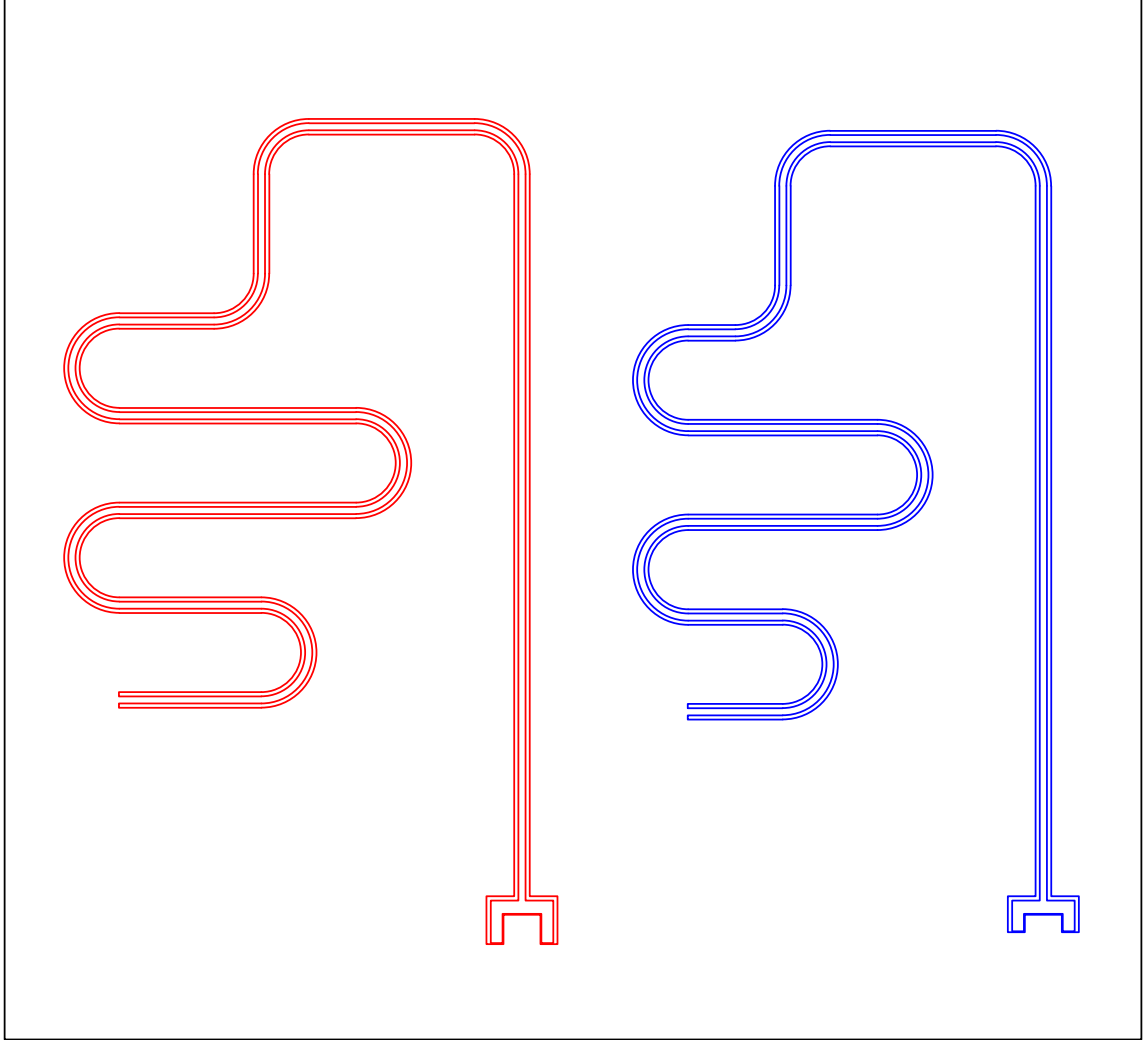
Figure 4.2: Layout of R_a (red) and R_m (blue). Each resonator consists of a regular CPW part and a claw part. R_a and R_m is different from each other in both the CPW part and the claw part.
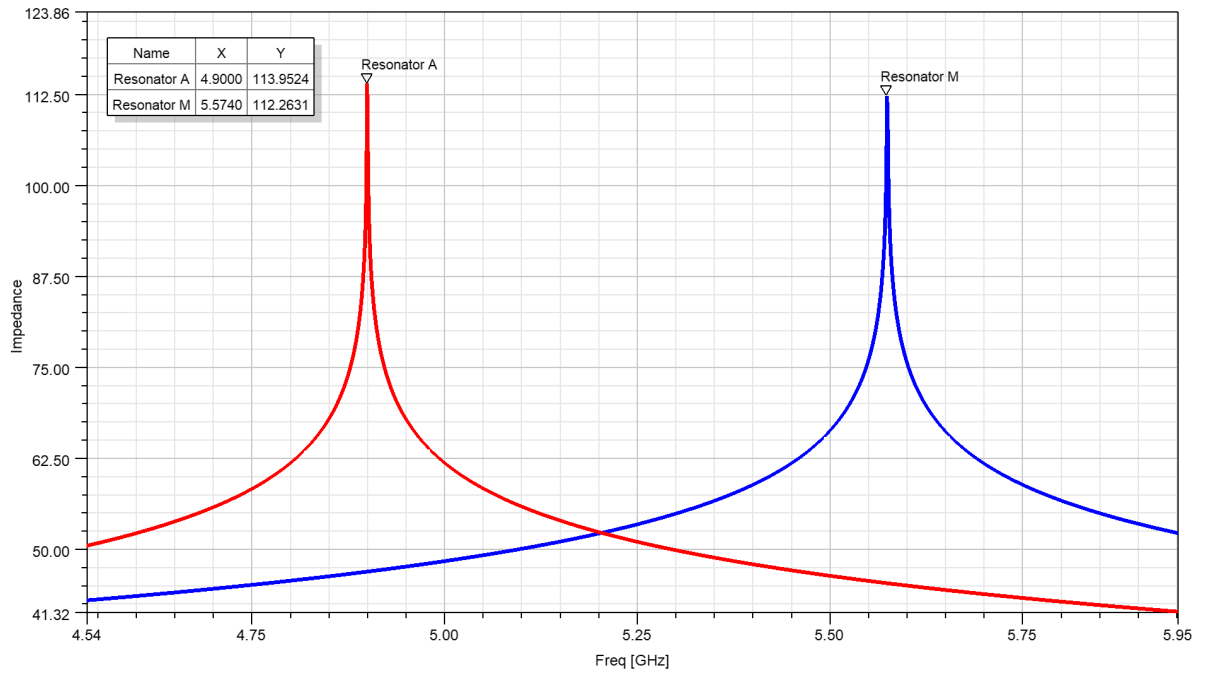
Figure 4.3: Impedance of R_a and R_m from EM simulation. The impedance of R_a (red) and R_m (blue) are plotted with the frequency. The maximum point of the impedance of R_a (R_m), which indicates the resonant frequency of R_a (R_m), is marked with "Resonator A" ("Resonator M").

Name	X	Y
Resonator A	4.9000	-0.0000
Resonator M	5.5740	-0.0000
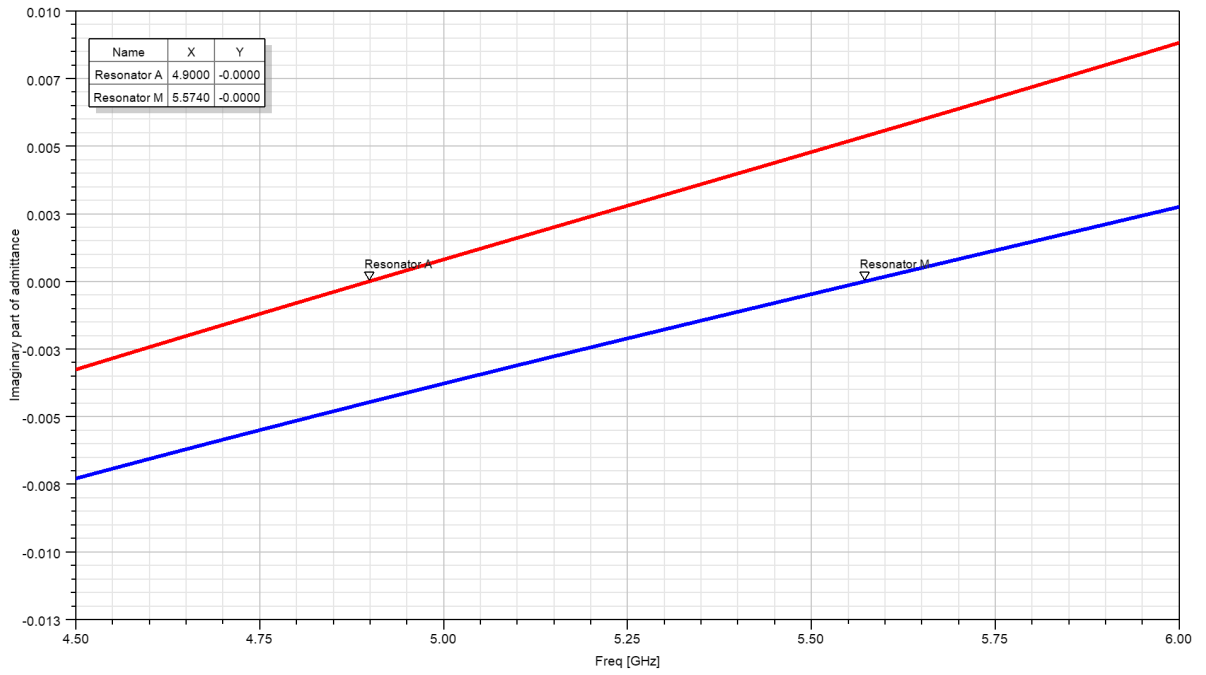
Figure 4.4: Imaginary part of the admittance of R_a (red) and R_m (blue) from EM simulation. The marker "Resonator A" ("Resonator M") is put at the resonant frequency of R_a (R_m).

and

$$\frac{dY_{\text{in}}}{d\omega} = \frac{1}{2\pi}\frac{dY_{\text{in}}}{df}, \tag{4.15}$$

the effective capacitances for R_a and R_m can be calculated using Eq. (4.8),

$$C_a = \frac{s_a}{4\pi} = 637 \text{ fF}, \tag{4.16}$$

$$C_m = \frac{s_m}{4\pi} = 517 \text{ fF}. \tag{4.17}$$

Then the effective inductance for R_a and R_m are given by

$$L_a = \frac{1}{\omega_a^2 C_a} = 1.66 \text{ nH}, \tag{4.18}$$

$$L_m = \frac{1}{\omega_m^2 C_m} = 1.58 \text{ nH}. \tag{4.19}$$

For the resonator R_b, we use the same design of R_a, thus we also have $\omega_b = 2\pi \times 4.9$ GHz, $C_b = C_a$, and $L_b = L_a$. In this way, we accomplish our design aim that $\omega_a = \omega_b \approx 2\pi \times 5$ GHz and $\omega_m \approx 2\pi \times 5.5$ GHz.

4.2 Simulation of coupling capacitance

In this section we use the EM simulation software *ANSYS Q3D* to obtain the coupling capacitance between the resonators and the Xmon, C_{ij} ($i, j = a, b, m, x$ and $i < j$), and the shunting capacitance C_x of the Xmon .

As shown in Fig. 4.5, we only clip the area around the Xmon for simulation instead of using the whole chip in Fig. 3.2. Because this area contribute to the main part of the coupling capacitance, the simulation using this area can yield results with enough accuracy in a moderate time. We also ignore the flux biasing line in our simulation, as it is grounded and contributes little to the coupling capacitances.

Figure 4.5: Xmon area for capacitance simulation. A rectangle area around the Xmon is clipped from the whole chip layout in Fig. 3.2 for capacitance simulation. The flux biasing line is ignored as it contributes little to the coupling capacitances.
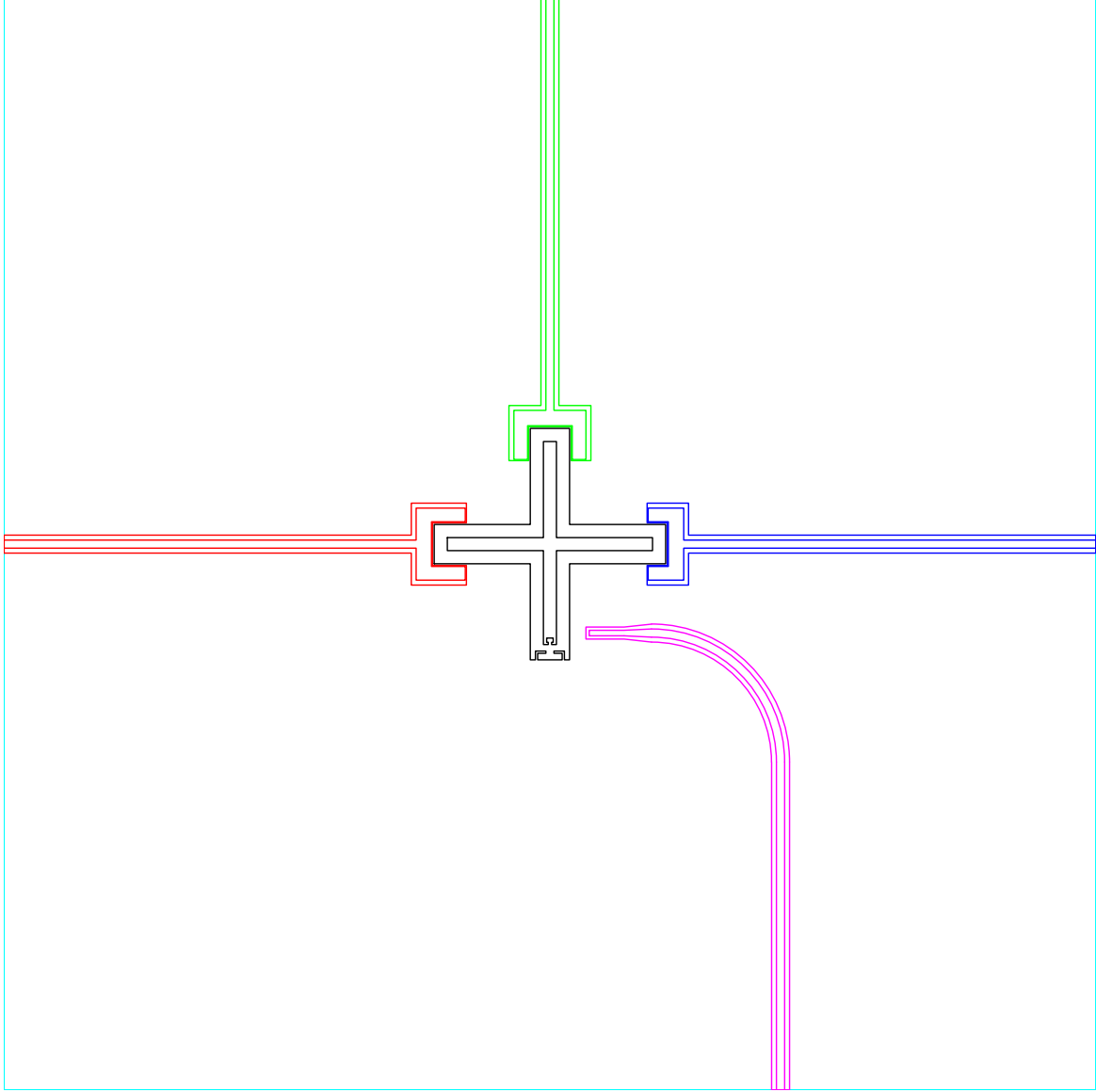
The simulation results for coupling capacitance are given as below,

$$C_{ab} = 0.137 \text{ fF}, \tag{4.20}$$
$$C_{am} = 0.0449 \text{ fF}, \tag{4.21}$$
$$C_{bm} = 0.112 \text{ fF}, \tag{4.22}$$
$$C_{ax} = 3.47 \text{ fF}, \tag{4.23}$$
$$C_{bx} = 3.47 \text{ fF}, \tag{4.24}$$
$$C_{mx} = 2.40 \text{ fF}. \tag{4.25}$$

Besides the coupling capacitance, the capacitance of each components to the ground plane can also be calculated. The capacitance between the Xmon and the ground plane, i.e, the capacitance shunted to the Josephson junction C_x, is given by

$$C_x = 90.3 \text{ fF}. \tag{4.26}$$

This parameter will be used in Sec. 4.3 for the design of Josephson junction.

4.3   Design of Josephson junction

In this section, we design the fabrication parameters of the Josephson junctions, which are used in the Xmon of the RXR system.

As shown in Fig. 4.6, we use the double-angle shadow evaporation technique [39] to fabricate the Josephson junction, with the parameters for fabrication given in Table 4.2. t_1 is the thickness of first deposition when the deposition is perpendicular to the substrate. As the actual first deposition is tilted by an angle θ_1, t_1 is the length of $\overline{\text{AB}}$ (light blue line in Fig. 4.6). Similarly, for the second deposition tilted by an angle θ_2, t_2 is the length of $\overline{\text{CD}}$ (yellow line in Fig. 4.6).

The area of the junction, A_J, is the overlapping area between the first and the second deposition layers. We have

$$A_\text{J} = W_\text{J}\, b_\text{J}, \tag{4.27}$$

where W_J is the width of the junction, and b_J is the length of the junction. W_J is determined by the smaller width between the two windows for deposition, i.e., the width of the red box in Fig. 4.6(a). b_J is the length of $\overline{\text{BC}}$ (green line in Fig. 4.6(b)), which is given by

$$b_\text{J} = (t_r - t_1 \cos\theta_1)\tan\theta_2 + (t_r - t_1 \cos\theta_1)\tan\theta_1 - b. \tag{4.28}$$
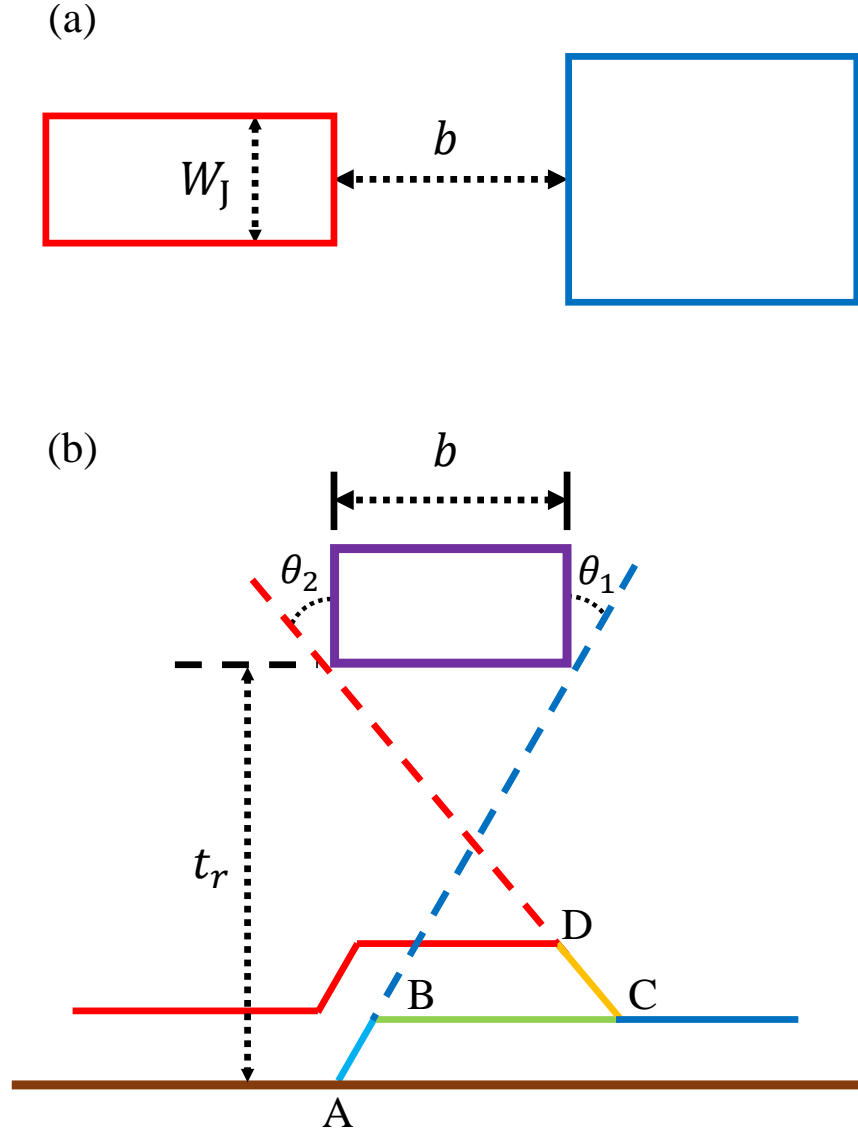
Figure 4.6: Fabrication of Josephson junction. (a) Schematic of the fabrication of a Josephson junction in the top view. Two windows (the red and the blue boxes) separated by the length b are developed from the photoresist, in which the blue (red) box is the window for the first (second) deposition. The red box has a width of W_J, which is smaller than that of the blue box. (b) Schematic of the fabrication of a Josephson junction in the side view. The first (second) deposition is tilted by an angle θ_1 (θ_2) with respect to the normal direction of the substrate (brown line). t_r is the thickness of the bottom layer photoresist.

θ_1	Angle of the first deposition
t_1	Thickness of the first deposition
θ_2	Angle of the second deposition
t_2	Thickness of the second deposition
t_r	Thickness of the bottom layer photoresist
b	Width of the photoresist bridge
W_J	Width of the junction
b_J	Length of the junction

Table 4.2: Parameters of Josephson junction fabrication

Then the Josephson energy of the junction is given by

$$E_J = J_u A_J, \tag{4.29}$$

where J_u is the current density of the junction. According to the results of previous fabrications, we use $J_u = 8 \times 10^{-7}$ A/μm^2 for the following calculation.

Now, we determine the fabrication parameters of the junctions on the RXR chip. First, we need to obtain the turn-off ratio r_{off} in Eq. (3.34). Using the simulation results given in Sec. 4.1 and Sec. 4.2, and ignoring the effects of R_m, we have

$$\widetilde{C}_{rx} = 18.4 \text{ pF}, \tag{4.30}$$

$$\widetilde{C}_{ab} = 1.59 \text{ nF}, \tag{4.31}$$

$$\widetilde{C}_x = 99.6 \text{ fF}, \tag{4.32}$$

$$\omega_r = \omega_a = 2\pi \times 4.9 \text{ GHz}. \tag{4.33}$$

Then r_{off} is given by

$$r_{\text{off}} = \frac{\widetilde{C}_{rx}}{\sqrt{\widetilde{C}_{rx}^2 - \widetilde{C}_{ab}\widetilde{C}_x}} = 1.37. \tag{4.34}$$

Thus the coupling between R_a and R_b vanishes when the Xmon is tuned to the turn-off frequency

$$\omega_{\text{off}} = r_{\text{off}} \omega_r \approx 2\pi \times 6.7 \text{ GHz}. \tag{4.35}$$

To turn off the coupling between R_a and R_b, the frequency range of the Xmon should cover the turn-off frequency ω_{off}. For the Xmon on the RXR chip, we use a symmetric dc-SQUID consisting of two junctions with the same Josephson energy E_J. Using Eq. (2.13)

and Eq. (3.20), the frequency of this Xmon is given by

$$\omega_x(f) = \frac{1}{\hbar}\left(\sqrt{16E_{\mathrm{J}}|\cos(f)|E_{cx}} - E_{cx}\right). \tag{4.36}$$

where $E_{cx} = e^2/(2\widetilde{C}_x) = h \times 0.194$ GHz. From the above equation, the maximum frequency of the Xmon is given by

$$\omega_{\mathrm{max}} = \frac{1}{\hbar}\left(\sqrt{16E_{\mathrm{J}}E_{cx}} - E_{cx}\right). \tag{4.37}$$

Here we set the design aim of ω_{max} as $2\pi \times 7.5$ GHz, which is much larger than $\omega_{\mathrm{off}} = 2\pi \times 6.7$ GHz. With such a large redundancy of 0.8 GHz, we can make sure that ω_{off} falls into the frequency range of the Xmon.

By choosing a set of fabrication parameters in Table 4.2, we determine the Josephson energy E_{J} in Eq. (4.37), and thus determine ω_{max}. In this process, both the design aim of ω_{max} and the range of the fabrication parameters need to be taken into consideration. We note that usually the values of t_1, t_2, t_r, and b are kept unchanged, and we only change θ_1, θ_2, and W_{J} to realize the design aim. Finally, the fabrication parameters of the junction are set as below,

$$\theta_1 = \theta_2 = 24°, \tag{4.38}$$
$$t_1 = 40 \text{ nm}, \tag{4.39}$$
$$t_2 = 60 \text{ nm}, \tag{4.40}$$
$$t_r = 500 \text{ nm}, \tag{4.41}$$
$$b = 200 \text{ nm}, \tag{4.42}$$
$$W_{\mathrm{J}} = 225 \text{ nm}. \tag{4.43}$$

Using these fabrication parameters, we have

$$E_{\mathrm{J}} = h \times 19 \text{ GHz}, \tag{4.44}$$
$$\omega_{\mathrm{max}} = 2\pi \times 7.5 \text{ GHz}, \tag{4.45}$$

which just satisfy our design aim of ω_{max}.

4.4   Energy spectrum of RXR

With all parameters of the resonators and the Xmon derived in the previous sections, now we simulate the RXR chip using the Hamiltonian H_{tot} in Eq. (3.15). The codes for this numerical calculation are given in App. B.

We summarize the parameters derived in the sections 4.1-4.3 as below,

$$L_a = L_b = 1.66 \text{ nH}, \tag{4.46}$$
$$L_m = 1.58 \text{ nH}, \tag{4.47}$$
$$C_a = C_b = 637 \text{ fF}, \tag{4.48}$$
$$C_m = 517 \text{ fF}, \tag{4.49}$$
$$C_{ab} = 0.137 \text{ fF}, \tag{4.50}$$
$$C_{am} = 0.0449 \text{ fF}, \tag{4.51}$$
$$C_{bm} = 0.112 \text{ fF}, \tag{4.52}$$
$$C_{ax} = 3.47 \text{ fF}, \tag{4.53}$$
$$C_{bx} = 3.47 \text{ fF}, \tag{4.54}$$
$$C_{mx} = 2.40 \text{ fF}, \tag{4.55}$$
$$C_x = 90.3 \text{ fF}, \tag{4.56}$$
$$E_{\mathrm{J}} = h \times 19 \text{ GHz}. \tag{4.57}$$

Using Eqs. (3.16–3.19), the frequencies of R_a, R_b, R_m, and the maximum frequency of the Xmon are given by

$$\omega_a = 2\pi \times 4.8809 \text{ GHz}, \tag{4.58}$$
$$\omega_b = 2\pi \times 4.8806 \text{ GHz}, \tag{4.59}$$
$$\omega_m = 2\pi \times 5.5552 \text{ GHz}, \tag{4.60}$$
$$\omega_{\mathrm{max}} = 2\pi \times 7.4980 \text{ GHz}. \tag{4.61}$$

Here, we present more significant figures of our data for comparison. We note that ω_a and ω_b are slightly different, even though R_a and R_b have the same design parameters. The reason for this asymmetry is $C_{bm} > C_{am}$, i.e., R_m couples more strongly with R_b than with R_a.

With the above parameters, we can construct H_{tot} and calculate its eigenstates. As shown in Fig. 4.7, the lowest five eigenenergies (in units of frequency) of H_{tot} are plotted as a function of the biasing flux of the Xmon $f \equiv \pi \Phi_{\mathrm{ext}}/\Phi_0$. Fig. 4.7 can be approximately regarded as a figure consisting of four horizontal lines and a decreasing curve. First, the lowest horizontal line at 0 GHz represents the ground state of H_{tot}, in which R_a, R_b, R_m, and the Xmon are all staying at their corresponding ground states. Second, the two horizontal lines at about 4.9 GHz are the eigenmodes of the two resonators R_a and R_b. Third, the horizontal line at about 5.5 GHz is the first excited state of R_m. At last, the
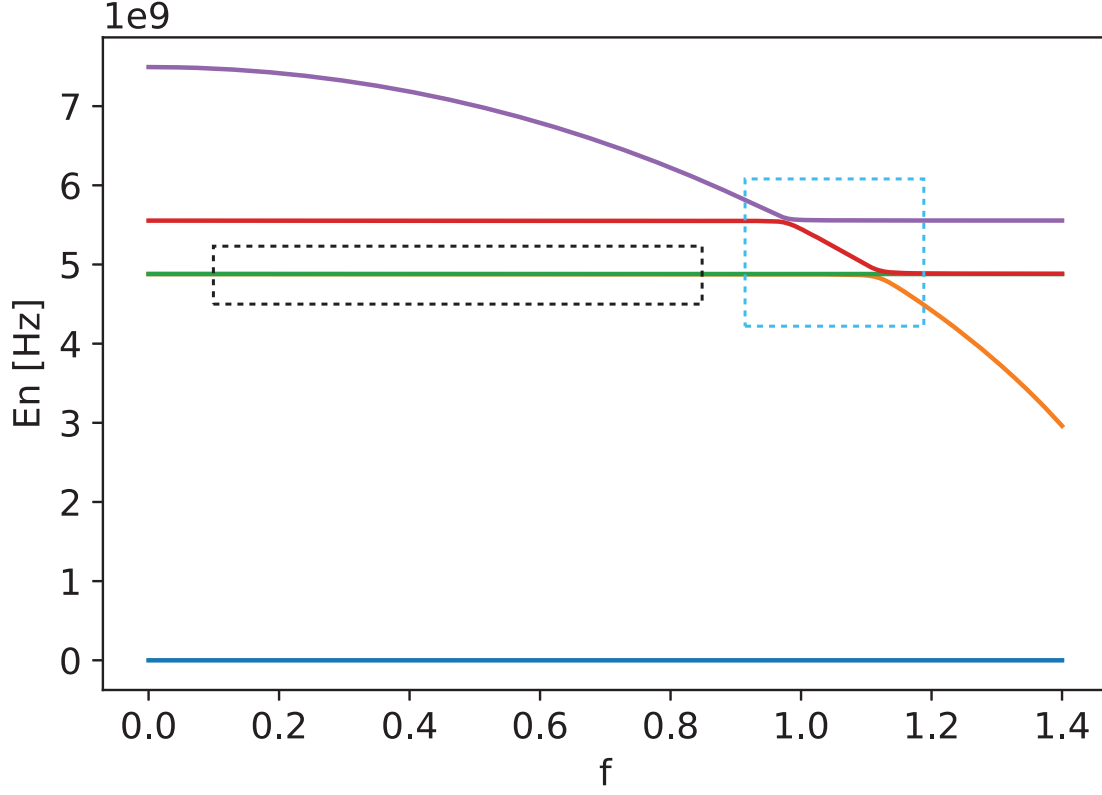
Figure 4.7: Energy levels of the RXR chip. The lowest five eigenenergies (in units of frequency) of H_{tot} are plotted as a function of the biasing flux f. From the lowest to the highest eigenenergy, the corresponding curves are plotted in blue, yellow, green, red, and purple, respectively. The area enclosed by the blue (black) dashed rectangle is plotted in Fig. 4.8 (Fig. 4.9) for further discussion.
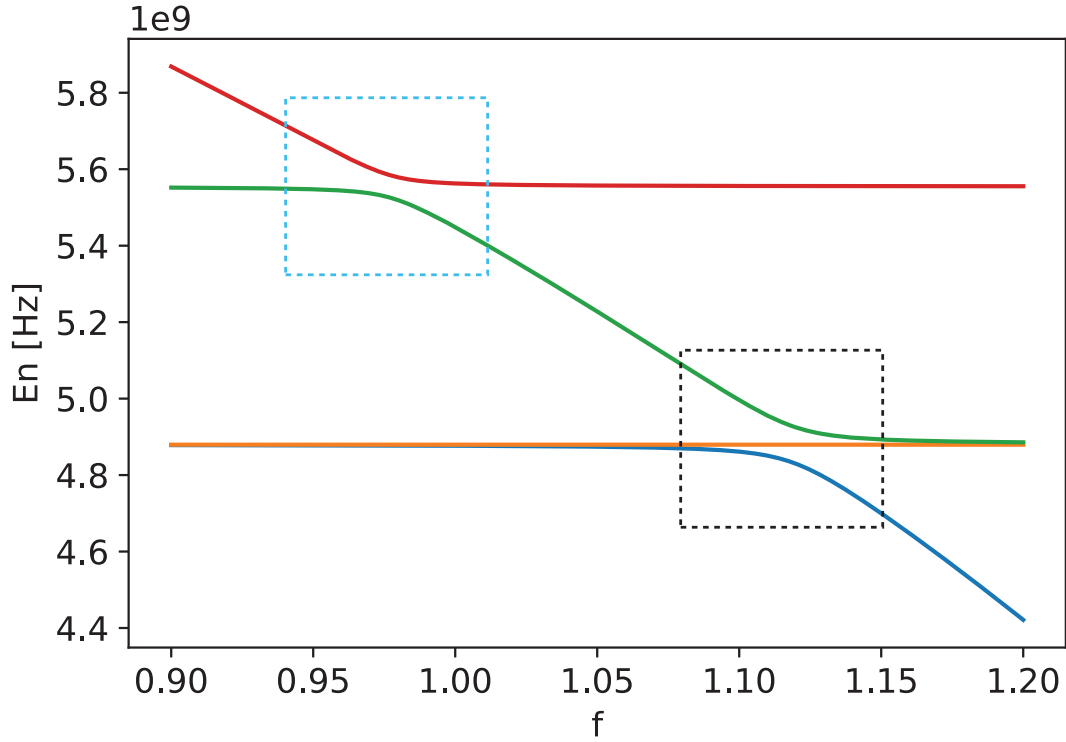
Figure 4.8: Anti-crossing patterns formed by the Xmon and the resonators. The area enclosed by the blue dashed rectangle in Fig. 4.7 is plotted here, showing the energy levels of H_{tot} when the Xmon is resonant with R_a, R_b or R_m. The first, second, third, and fourth excited states are plotted in blue, yellow, green, and red, respectively. Two anti-crossing patterns are marked by a blue dashed rectangle and a black dashed rectangle, respectively.

decreasing curve is the first excited state of the Xmon, which goes down with the increase of f.

The above physical interpretations are valid when the Xmon is largely detuned from the resonators. In contrast, when the Xmon is resonant with R_a, R_b, or R_m, the states of the Xmon and the resonator mix together, resulting in the anti-crossing pattern in the figure of the energy levels.

To illustrate this phenomenon, in Fig. 4.8, we zoom in the area enclosed by the blue dashed rectangle in Fig. 4.7. When ω_x is tuned to $\omega_m \approx 5.5$ GHz, the Xmon strongly interacts with R_m, resulting in the anti-crossing pattern formed by the red and the green curves (the blue dashed rectangle Fig. 4.8). When ω_x is tuned to $\omega_a \approx \omega_b \approx 4.9$ GHz, the Xmon strongly interacts with one eigenmode of R_a and R_b, resulting in the anti-crossing pattern formed by the green and the blue curves (the black dashed rectangle in Fig. 4.8). In contrast, the other eigenmode (yellow line) keeps unchanged with respect to f, indicating that there is almost no interaction between this eigenmode and the Xmon. This phenomenon between the Xmon and the eigenmodes of R_a and R_b can be better interpreted using the annihilation operators $c_\pm$ of the eigenmodes defined as below,

$$c_+ \equiv \cos(\theta)a + \sin(\theta)b, \tag{4.62}$$

$$c_- \equiv \sin(\theta)a - \cos(\theta)b, \tag{4.63}$$

with

$$\theta = \frac{1}{2}\tan^{-1}\left(\frac{2g_{ab}}{\omega_a - \omega_b}\right). \tag{4.64}$$

As R_m is largely detuned from R_a, R_b, and the Xmon, we can omit the Hamiltonian of R_m, and use the Hamiltonian H in Eq. (3.1) to describe the system. R_m can be regarded as a weak perturbation to the Hamiltonian H, which makes $\omega_a \neq \omega_b$ and $g_a \neq g_b$. However, this perturbation is very weak and we have $|\omega_a - \omega_b| \ll \omega_a, \omega_b$ and $|g_a - g_b| \ll |g_a|, |g_b|$.

Rewriting the Hamiltonian H in Eq. (3.1) with $c_\pm$, we get

$$H/\hbar = \omega_+ c_+^\dagger c_+ + \omega_- c_-^\dagger c_- + g_+(c_+^\dagger \sigma + c_+ \sigma^\dagger) + g_-(c_-^\dagger \sigma + c_- \sigma^\dagger), \tag{4.65}$$

where

$$\omega_+ = \cos^2(\theta)\omega_a + \sin^2(\theta)\omega_b + 2\cos(\theta)\sin(\theta)g_{ab}, \tag{4.66}$$

$$\omega_- = \sin^2(\theta)\omega_a + \cos^2(\theta)\omega_b - 2\cos(\theta)\sin(\theta)g_{ab}, \tag{4.67}$$

$$g_+ = \cos(\theta)g_a + \sin(\theta)g_b, \tag{4.68}$$

$$g_- = \sin(\theta)g_a - \cos(\theta)g_b. \tag{4.69}$$
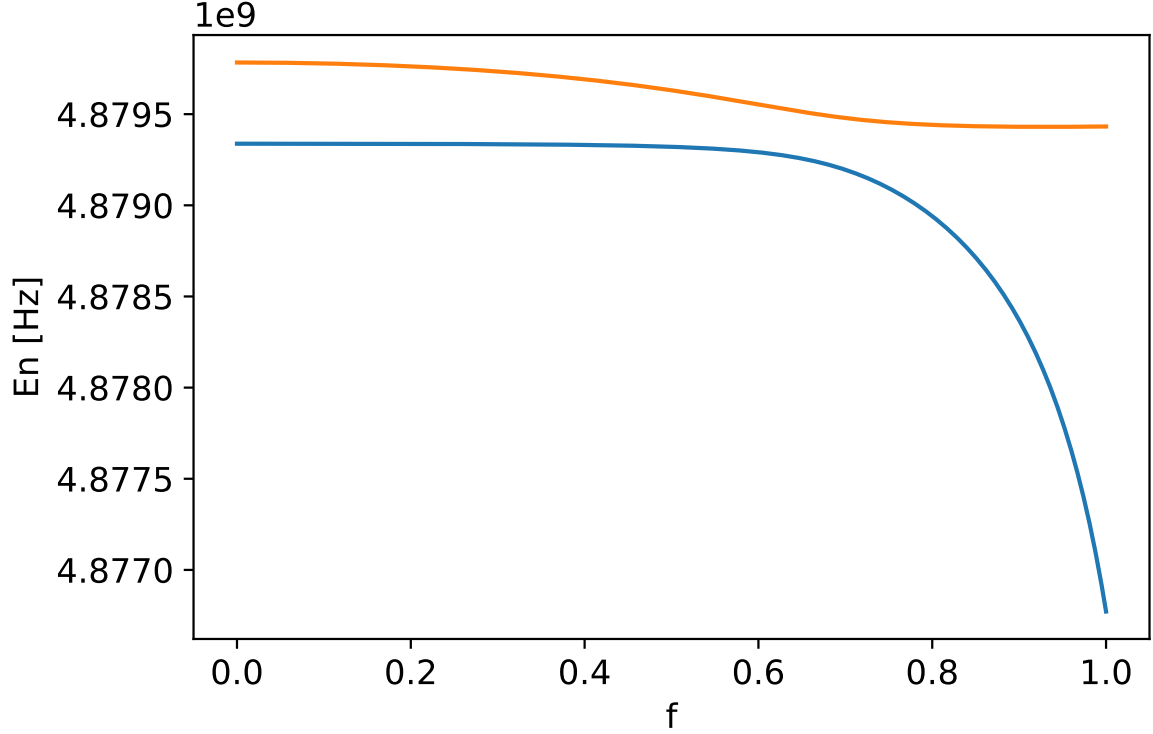
Figure 4.9: Eigenmodes of R_a and R_b. The area enclosed by the black dashed rectangle in Fig. 4.7 is plotted here, showing the energies of the two eigenmodes of R_a and R_b, in which the lower (higher) energy level is plotted in blue (yellow).

In deriving Eq. (4.65), the counter-rotating terms in Eq. (3.1) are ignored because $\omega_a \approx \omega_b \approx \omega_x$. According to Eq. (4.65), g_+ (g_-) is the coupling strength between the Xmon and the "+" ("−") mode of R_a and R_b. As $\omega_a \approx \omega_b$ and $g_a \approx g_b$, we have $\theta \approx \pi/4$, $g_+ \approx \sqrt{2}g_a$, and $g_- \approx 0$. Thus there is almost no interaction between the Xmon and the "−" mode (yellow line in Fig. 4.8). In addition, if $\omega_a = \omega_b$ and $g_a = g_b$, then $g_- = 0$ and the "−" mode is completely decoupled from the Xmon.

In Fig. 4.9, we zoom in the area enclosed by the black dashed rectangle in Fig. 4.7, showing the energies of the eigenmodes of R_a and R_b. We can find there is always a gap between the two eigenmodes of R_a and R_b. This gap results from the frequency difference between ω_a and ω_b. As mentioned above, this frequency difference between R_a and R_b is induced by the fact that $C_{am} < C_{bm}$. As a comparison, we can assume $C_{am} = C_{bm} = 0$,

Figure 4.10: Eigenmodes of R_a and R_b in the symmetric situation. The energies of the two eigenmodes of R_a and R_b is plotted as a function of the biasing flux f, with the assumption $C_{am} = C_{bm} = 0$. The lower (higher) energy level is plotted in blue (yellow).

and keep all the other parameters unchanged. In this case, R_a and R_b are symmetric on the RXR chip, and we have $\omega'_a = \omega'_b = 2\pi \times 4.8866$ GHz. In Fig. 4.10, we plot the energies of the eigenmodes of R_a and $R_b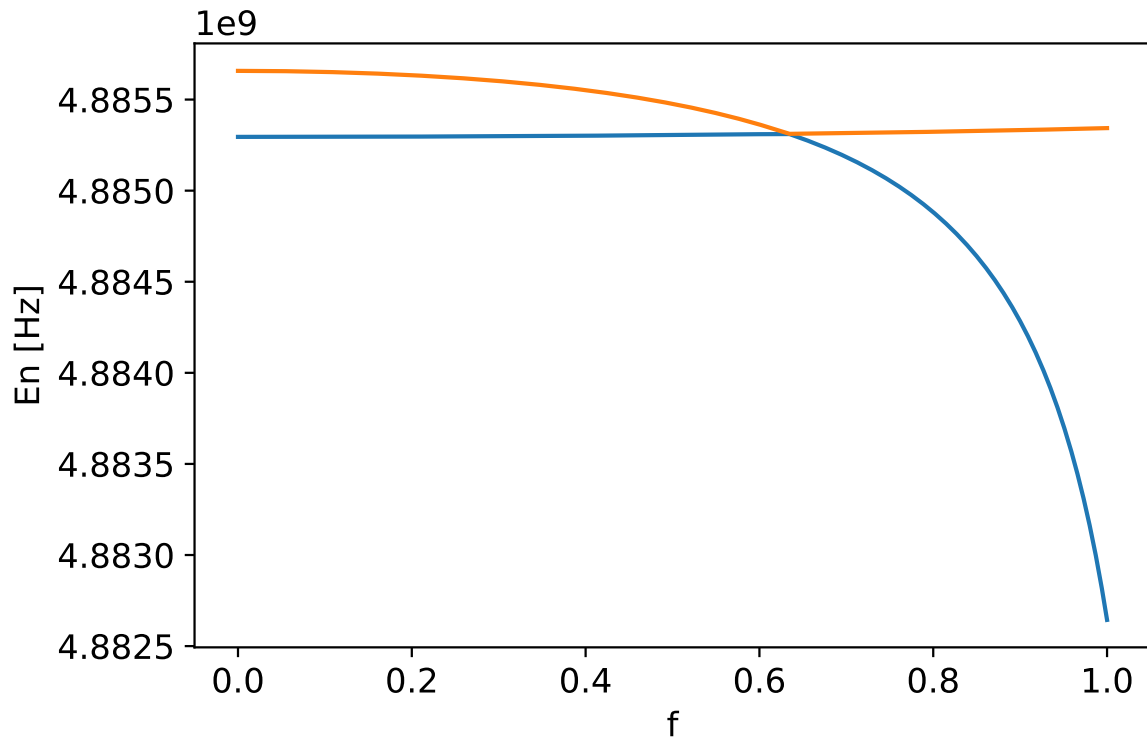$ with the assumption $C_{am} = C_{bm} = 0$. In contrast to Fig. 4.9, we can find that the two eigenmodes become degenerate at $f = 0.634$, where the coupling between g_a and g_b is zero.

Now, we come back to the situation shown in Fig. 4.9, where the asymmetric perturbation from R_m is taken into account. As the Xmon is dispersively coupled to R_a and R_b, we can use the Hamiltonian $\widetilde{H}$ in Eq. (3.3) to describe R_a and R_b. Similar to Eq. (4.62) and Eq. (4.63), we use the annihilation operators d_+ and d_- defined as below,

$$d_+ \equiv \cos(\gamma)a + \sin(\gamma)b, \tag{4.70}$$
$$d_- \equiv \sin(\gamma)a - \cos(\gamma)b, \tag{4.71}$$

to rewrite $\widetilde{H}$. As a result, we obtain the following Hamiltonian

$$\widetilde{H}/\hbar = \widetilde{\omega}_+ d_+^\dagger d_+ + \widetilde{\omega}_- d_-^\dagger d_-, \tag{4.72}$$

where

$$\gamma = \frac{1}{2}\tan^{-1}\left(\frac{2\widetilde{g}_{ab}}{\widetilde{\omega}_a - \widetilde{\omega}_b}\right), \tag{4.73}$$
$$\widetilde{\omega}_+ = \cos^2(\gamma)\widetilde{\omega}_a + \sin^2(\gamma)\widetilde{\omega}_b + 2\cos(\gamma)\sin(\gamma)\widetilde{g}_{ab}, \tag{4.74}$$
$$\widetilde{\omega}_- = \sin^2(\gamma)\widetilde{\omega}_a + \cos^2(\gamma)\widetilde{\omega}_b - 2\cos(\gamma)\sin(\gamma)\widetilde{g}_{ab}. \tag{4.75}$$

From Eq. (4.74) and Eq. (4.75), we can find that $\widetilde{\omega}_+ \geq \widetilde{\omega}_-$. Thus the "+" mode corresponds to the higher energy level (the yellow curve) in Fig. 4.9, while the "−" mode corresponds to the lower energy level (the blue curve) in Fig. 4.9.

The frequency difference between the eigenmodes is given by

$$\Delta_\pm \equiv \widetilde{\omega}_+ - \widetilde{\omega}_- = \sqrt{(\widetilde{\omega}_a - \widetilde{\omega}_b)^2 + 4\widetilde{g}_{ab}^2} \tag{4.76}$$

$$= \sqrt{(\Delta_{ab} + \delta)^2 + 4\widetilde{g}_{ab}^2}, \tag{4.77}$$

where

$$\Delta_{ab} = \omega_a - \omega_b, \tag{4.78}$$
$$\delta = g_a^2\left(\frac{1}{\Delta_a} - \frac{1}{\Sigma_a}\right) - g_b^2\left(\frac{1}{\Delta_b} - \frac{1}{\Sigma_b}\right). \tag{4.79}$$

Here, δ results from the frequency corrections to R_a and R_d induced by the Xmon. In the dispersive coupling regime where $\omega_x/(2\pi)$ is in the range of 6–7.5 GHz, we have $|\delta| < 2\pi \times 10^{-3}$ MHz $\ll \Delta_{ab}$. Thus δ is ignored in the following calculations.

Using Eq. (4.58), Eq. (4.59), and Eq. (4.76), we have $\Delta_\pm \geq \Delta_{ab} = 2\pi \times 0.3$ MHz. As a result, there is always a gap between the energies of the two eigenmodes in Fig. 4.9. Furthermore, we can use Eq. (4.76) to calculate the effective coupling strength $|\widetilde{g}_{ab}|$ between R_a and R_b. According to Fig. 4.9, $\Delta_\pm$ reaches its minimum value $\Delta_\pm^{(\mathrm{min})} \approx 2\pi \times 0.3$ MHz at $f = 0.637$. As $\Delta_\pm^{(\mathrm{min})} \approx \Delta_{ab}$, we can infer that $\widetilde{g}_{ab} \approx 0$ at $f = 0.637$. The corresponding frequency of the Xmon at $f = 0.637$ is the turn-off frequency ω_{off}. Using Eq. (4.36), we have $\omega_{\mathrm{off}} = 2\pi \times 6.6966$ GHz, which agrees with our estimation for ω_{off} in Eq. (4.35).

According to Eq. (4.76), $\Delta_\pm$ can be used as an indicator of the value of $|\widetilde{g}_{ab}|$. From Fig. 4.9, we can find $|\widetilde{g}_{ab}|$ increases as ω_x deviates from ω_{off}. We note that, in order to achieve a large $|\widetilde{g}_{ab}|$, it is more efficient to decrease ω_x than to increase ω_x, because $|\widetilde{g}_{ab}| \leq g_{ab}$ when $\omega_x > \omega_{\mathrm{off}}$. Here, we take $f = 0.85$ as an example to demonstrate the coupling strength in the regime $\omega_x < \omega_{\mathrm{off}}$. In this case, we have $\omega_x = 2\pi \times 6.0482$ GHz, $\Delta_\pm = 2\pi \times 0.72$ MHz, and $|\widetilde{g}_{ab}| = 2\pi \times 0.34$ MHz. This coupling strength corresponds to a time of $2\pi/|\widetilde{g}_{ab}| \approx 3$ μs. This time is too long to perform a gate operation, as the relaxation time of a superconducting CPW resonator is 1–5 μs [40, 41]. We can further increase $|\widetilde{g}_{ab}|$ by tuning ω_x towards ω_a. However, we should not make ω_x too close to ω_a, ω_b, or ω_m, because in this case the assumption of dispersive coupling is invalid. As $\omega_{\mathrm{off}} > \omega_m > \omega_a$, the resonator R_m limits the tuning range of ω_x, and thus limits the range of $|\widetilde{g}_{ab}|$. Without R_m, we can further tune ω_x down to 5.5 GHz to achieve a larger $|\widetilde{g}_{ab}|$, where the Xmon is still dispersively coupled to R_a and R_b.

Besides eigenenergies, we can also use eigenstates to characterize the tunable coupling between R_a and R_b. First, we define the single-photon state of R_a as

$$|\psi_a\rangle \equiv |1_a\rangle \otimes |0_b\rangle \otimes |0_m\rangle \otimes |g\rangle, \tag{4.80}$$

where $|n_i\rangle$ is the n-photon Fock state of the resonator R_i $(i = a, b, m)$, and $|g\rangle$ is the ground state of the Xmon. Similarly, the single-photon state of R_b is defined as

$$|\psi_b\rangle \equiv |0_a\rangle \otimes |1_b\rangle \otimes |0_m\rangle \otimes |g\rangle. \tag{4.81}$$

Second, we denote the first and the second excited states of H_{tot} as $|\psi_1\rangle$ and $|\psi_2\rangle$, respectively. When the Xmon is in the dispersive coupling regime, $|\psi_1\rangle$ ($|\psi_2\rangle$) corresponds to the single-photon state of the "$-$" ("$+$") eigenmode in Eq. (4.72). The projection

Figure 4.11: Probabilities of projecting $|\psi_1\rangle$ to $|\psi_a\rangle$ and $|\psi_b\rangle$. The probabilities $P_{1,a}$ (blue) and $P_{1,b}$ (yellow) are plotted as a function of f. At $f = 0.637$, $P_{1,a} \approx 0$ and $P_{1,b} \approx 1$.
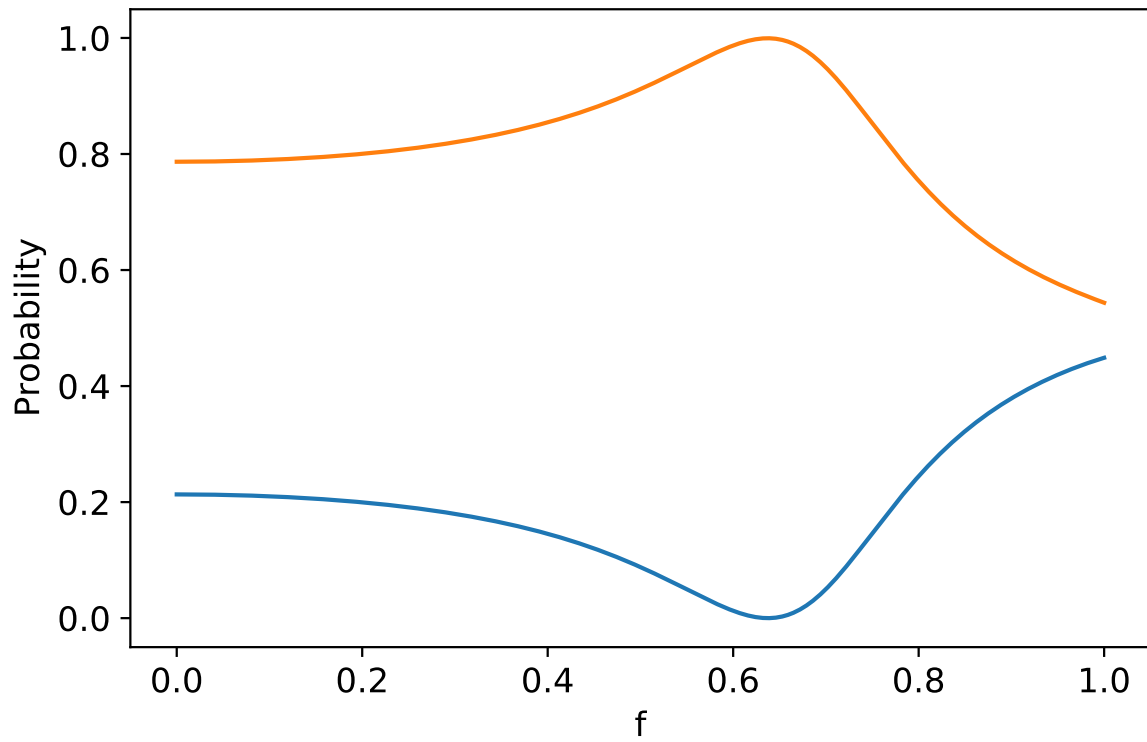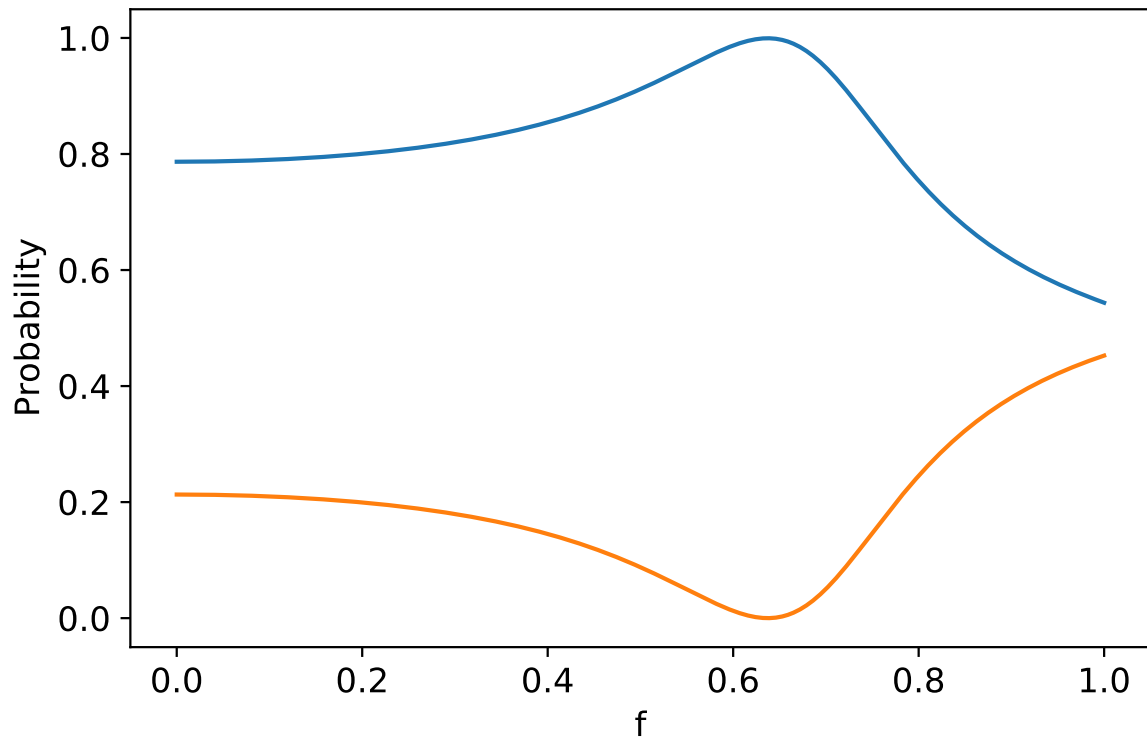
Figure 4.12: Probabilities of projecting $|\psi_2\rangle$ to $|\psi_a\rangle$ and $|\psi_b\rangle$. The probabilities $P_{2,a}$ (blue) and $P_{2,b}$ (yellow) are plotted as a function of f. At $f = 0.637$, $P_{2,a} \approx 1$ and $P_{2,b} \approx 0$.

probabilities from the eigenmodes "±" to the single-photon state of R_a and R_b are given as

$$P_{1,a} = |\langle\psi_a|\psi_1\rangle|^2, \tag{4.82}$$
$$P_{1,b} = |\langle\psi_b|\psi_1\rangle|^2, \tag{4.83}$$
$$P_{2,a} = |\langle\psi_a|\psi_2\rangle|^2, \tag{4.84}$$
$$P_{2,b} = |\langle\psi_b|\psi_2\rangle|^2. \tag{4.85}$$

According to Eq. (4.70) and Eq. (4.71), we have the following relations

$$P_{1,a} \approx P_{2,b} \approx \sin^2(\gamma), \tag{4.86}$$
$$P_{1,b} \approx P_{2,a} \approx \cos^2(\gamma). \tag{4.87}$$

When $\widetilde{g}_{ab} = 0$, we have $\gamma = 0$, $P_{1,a} \approx P_{2,b} \approx 0$, and $P_{1,b} \approx P_{2,a} \approx 1$. That is to say, $|\psi_1\rangle \approx |\psi_b\rangle$ and $|\psi_2\rangle \approx |\psi_a\rangle$ when $\widetilde{g}_{ab} = 0$.

Now, we numerically calculate $P_{i,j}$ ($i = 1, 2$ and $j = a, b$) by solving the eigenstates of H_{tot}. The results of $P_{1,a}$ and $P_{1,b}$ ($P_{2,a}$ and $P_{2,b}$) are plotted as a function of f in Fig. 4.11 (Fig. 4.12). From Fig. 4.11 and Fig. 4.12, we find the following relations,

$$P_{1,a} \approx P_{2,b}, \tag{4.88}$$
$$P_{1,b} \approx P_{2,a}, \tag{4.89}$$
$$P_{1,a} + P_{1,b} \approx 1, \tag{4.90}$$
$$P_{2,a} + P_{2,b} \approx 1, \tag{4.91}$$

which agree with Eq. (4.86) and Eq. (4.87). In addition, at $f = 0.637$, we have $P_{1,a} \approx P_{2,b} \approx 0$ and $P_{1,b} \approx P_{2,a} \approx 1$. Thus at $f = 0.637$, $|\psi_1\rangle \approx |\psi_b\rangle$ and $|\psi_2\rangle \approx |\psi_a\rangle$. This result is consistent with the minimum energy gap in Fig. 4.9, which also indicates that $\widetilde{g}_{ab}$ is turned off at $f = 0.637$.

4.5   Summary

In this chapter, we focus on the design, the simulation, and the fabrication of the RXR chip. We obtain the EM parameters according to the layout design of the chip and the fabrication parameters of the junction. Using the EM parameters, we numerically calculate the eigenenergies and the eigenstates of the chip. From the numerical results, we confirm that the effective coupling between R_a and R_b can be turned off by tuning the frequency of

the Xmon. For the present RXR chip, we have two main problems. First, the perturbation from R_m breaks the degeneracy of R_a and R_b, making $\omega_a \neq \omega_b$ and $g_a \neq g_b$. Second, the effective coupling between R_a and R_b is too small to perform fast gate operations. In Ch. 6, we shall discuss possible methods of solving the above problems and improving the RXR chip.

Chapter 5

Impedance engineering for broadband parametric amplification

In this chapter, we study impedance engineering for the Josephson parametric amplifier (JPA) to enhance its bandwidth, with a focus on impedance engineering of a certain type of JPA, the flux pumping JPA (FJPA). We first introduce the theoretical model of impedance engineering. Then we theoretically study impedance engineering for two different types of FJPA.

5.1   Introduction

The Josephson parametric amplifier is a type of superconducting circuits which can amplify the microwave signal it receives. The critical feature of the JPA is that it can achieve high gain, low-noise amplification. The average energy of the noises added by the JPA can approach a lower bound laid by the Heisenberg uncertainty principle [22, 23], which equals to a half of the energy of a photon at the signal frequency. Due to this property, the JPA has been widely used in measurements for superconducting circuits. The main shortcoming of the JPA is the limited bandwidth around 50 MHz [42, 43]. Although a special type of JPA, the traveling wave parametric amplifier (TWPA) [44, 45], can achieve a bandwidth around 4 GHz, the fabrication of TWPA is much sophisticated than the conventional JPA. Instead of using TWPA, another method of increasing the bandwidth of a JPA is found in Ref. [46]. In Ref. [46], scientists found that the bandwidth of an FJPA can be improved by inserting a tapered transmission line in the measurement chain, while the underlying

reason was not clearly understood. In Ref. [47], scientists clarified that the principle for the results in Ref. [46] is the impedance engineering, i.e., engineering the input impedance seen from the JPA side, and apply this method experimentally on a current pumping JPA (CJPA).

Following the principal in Ref. [47], in this chapter we theoretically study the way to improve the bandwidth of the FJPA by impedance engineering. The contents are organized as follows. In Sec. 5.2, we introduce the theoretical model of the JPA. In Sec. 5.3, we show the principal of the impedance engineering. In Sec. 5.4, we study impedance engineering of one type of FJPA, the lumped-element FJPA. In Sec. 5.5, we study impedance engineering of another type of FJPA, the transmission line (TL) FJPA. In Sec. 5.6, we summary this chapter.

5.2 Theoretical model of JPA

JPA can be modeled by a damped-driven nonlinear oscillator, which can have several resonant modes and input/output ports. Here we consider the simplest case, a 1-mode, 1-port oscillator with a quadratic Hamiltonian [22, 23],

$$\frac{H_{\mathrm{JPA}}}{\hbar} = \omega_a a^\dagger a + i\frac{\lambda}{2}(a^2 \exp(i(2\Omega_d t + \theta)) - h.c.), \tag{5.1}$$

where ω_a and a are the angular frequency and the annihilation operator for the oscillator mode, respectively. The external driving field is characterized by the driving strength λ, the angular frequency Ω_d, and phase θ.

Using the quantum Langevin equation [48] and the input-output relation [48], the relation between the oscillator and the input (output) field a_{in} (a_{out}) is given by

$$\frac{da}{dt} = \frac{i}{\hbar}[H_{\mathrm{JPA}}, a] - \frac{\kappa}{2}a + \sqrt{k}a_{\mathrm{in}}(t), \tag{5.2}$$

$$\sqrt{\kappa}a = a_{\mathrm{in}}(t) + a_{\mathrm{out}}(t), \tag{5.3}$$

where κ is the damping rates of the oscillator mode and also represents the coupling between the oscillator with the external field.

The amplification effect of the oscillator is characterized in the frequency domain, via the Fourier transform of the input (output) field operator $a_{\mathrm{in}}[\omega]$ ($a_{\mathrm{out}}[\omega]$). After receiving a signal $a_{\mathrm{in}}[\omega_S]$, the oscillator will output an amplified signal at the same frequency $a_{\mathrm{out}}[\omega_S]$. Together with $a_{\mathrm{out}}[\omega_S]$, the oscillator will also emit another signal $a_{\mathrm{out}}[\omega_I]$ with

the frequency $\omega_I = 2\Omega_d - \omega_S$. The frequencies ω_S and ω_I are called as signal frequency and idler frequency, respectively. The amplification performance for the input signal $a_{\mathrm{in}}[\omega_S]$ is described by the the photon number gain function $G(\omega_S) = |r(\omega_S)|^2 = |a_{\mathrm{out}}[\omega_S]/a_{\mathrm{in}}[\omega_S]|^2$, where $r(\omega_S)$ is the reflection coefficient.

The relation between ω_S and Ω_d defines two different operation modes of the amplifier. When $\omega_S \neq \omega_d$, i.e., $\omega_S \neq \omega_I$, the amplifier works in the non-degenerate mode, also called as phase-preserving mode. In this mode, the gain of the amplifier is independent of the relative phase between the driving field and the input signal, and both quadratures of the input signal are amplified with the same ratio. In contrast, when $\omega_S = \omega_I = \omega_d$, the amplifier works in the degenerate mode, also called as phase-sensitive mode. In this mode, the gain of the amplifier is sensitive to the relative phase between the driving field and the input signal. By tuning the relative phase, the amplifier amplifies one quadrature of the input signal while squeezes the other one. Here, we only consider the amplifier operating in the non-degenerate mode. Thus the phase of the driving field θ in Eq. (5.1) can be ignored in the following discussion.

Now we introduce the practical implementation of the JPA with Josephson junction circuits. There are two main types of JPA, the current pumping JPA (CJPA) and the flux pumping JPA (FJPA), named by the methods of applying the driving field. The schematic of a CJPA is shown in Fig. 5.1. This type of JPA has a transmon-like structure and utilizes the Kerr nonlinearity to implement the quadratic Hamiltonian in Eq. (5.1). As shown in Sec. 2.3, the transmon-like structure can be described by the Hamiltonian

$$\frac{H_t}{\hbar} = \omega_t a^\dagger a - \frac{K}{2} a^\dagger a^\dagger a a, \tag{5.4}$$

where

$$\omega_t = \frac{1}{\hbar} \left(\sqrt{8 E_{\mathrm{J}} E_{\mathrm{C}}} - E_{\mathrm{C}} \right) \tag{5.5}$$

and

$$K = \frac{E_{\mathrm{C}}}{\hbar} = \frac{e^2}{2 C_t \hbar}. \tag{5.6}$$

For the CJPA, the driving field is an intense coherent tone with amplitude α_{in} and angular frequency ω_c. This driving field is sent to the amplifier together with the signal to be processed $\delta a_{\mathrm{in}}(t)$, thus we have

$$a_{\mathrm{in}} = \alpha_{\mathrm{in}} \exp(-i\Omega_c t) + \delta a_{\mathrm{in}}(t). \tag{5.7}$$
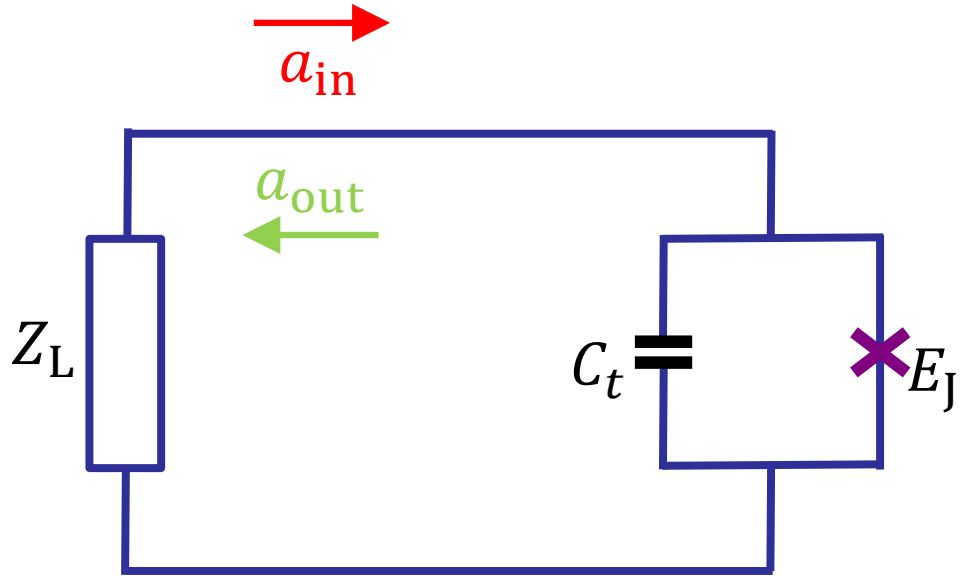
54

Figure 5.1: Schematic of a current pumping JPA. The current pumping JPA, which consists of a Josephson junction with the Josephson energy E_J and a shunting capacitance C_t, is connected to the measurement chain with an input impedance of Z_L, where a_{in} (a_{out}) represents the input (output) tone.

Correspondingly, the annihilation operator of the driven amplifier can also be separated into a classical part and a quantum part,

$$a = \alpha \exp(-i\Omega_c t) + \delta a(t), \tag{5.8}$$

where α is a complex number. Using Eq. (5.2) and Eqs. (5.4–5.8), the quantum Langevin equation for δa and δa_{in} is given by [22, 23]

$$\frac{d\delta a}{dt} = \frac{i}{\hbar}[H_c, \delta a] - \frac{\kappa}{2}\delta a + \sqrt{k}\delta a_{\text{in}}(t). \tag{5.9}$$

The effective Hamiltonian H_c in Eq. (5.9) is expressed as,

$$\frac{H_c}{\hbar} = \omega_c \delta a^\dagger \delta a + i\frac{\lambda_c}{2}(\delta a^2 \exp(i2\Omega_c t) - h.c.), \tag{5.10}$$

where

$$\omega_c = \omega_t - 2\lambda_c, \tag{5.11}$$

$$\lambda_c = K|\alpha|^2. \tag{5.12}$$

In deriving Eq. (5.9) and Eq. (5.10), non-RWA terms are neglected with the assumption $\Omega_c \approx \omega_t \approx \omega_c$.

Now we consider the theoretical model of an FJPA . As shown in Fig. 5.2, the FJPA also has a transmon-like structure, where the Josephson junction is replaced by a dc-SQUID. The dc-SQUID is threaded by an external flux Φ_{ext} generated by a coil. Recalling the knowledge of the dc-SQUID and the transmon in Sec. 2.2 and Sec. 2.3, respectively, the Hamiltonian of the transmon-like structure is given by

$$H_t = 4E_{\text{C}}n^2 - E_{\text{sq}}(\Phi_{\text{ext}})\cos\varphi, \tag{5.13}$$

where $E_{\text{C}} = e^2/(2C_t)$. The driving field is applied via the coil and generates the following external flux

$$\Phi_{\text{ext}} = \Phi_{\text{DC}} + \Phi_{\text{AC}}\cos(\Omega_f t), \tag{5.14}$$

where $\Phi_{\text{AC}}/\Phi_{\text{DC}} \ll 1$. As the AC part of Φ_{ext} is a small value, we can expand $E_{\text{sq}}(\Phi_{\text{ext}})$ to the first order of Φ_{AC},

$$E_{\text{sq}}(\Phi_{\text{ext}}) \approx E_{\text{sq}}(\Phi_{\text{DC}}) + \left.\frac{\partial E_{\text{sq}}(\Phi)}{\partial \Phi}\right|_{\Phi=\Phi_{\text{DC}}}\Phi_{\text{AC}}\cos(\Omega_f t)$$

$$= E_{\text{sum}}\cos\varphi_{\text{DC}} - \varphi_{\text{AC}}E_{\text{sum}}\sin\varphi_{\text{DC}}\cos(\Omega_f t), \tag{5.15}$$
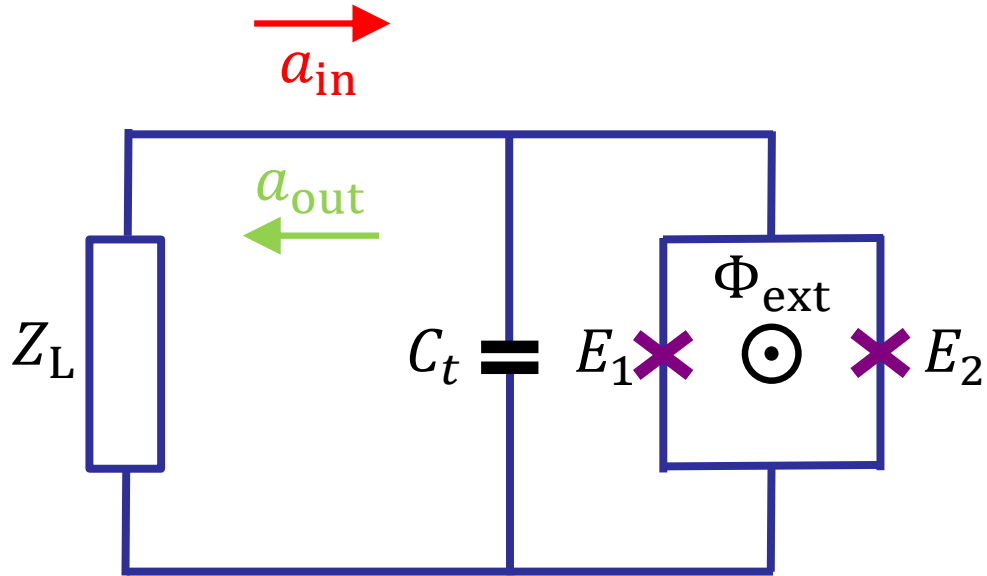
Figure 5.2: Schematic of a flux pumping JPA. The flux pumping JPA, which consists of a dc-SQUID biased by the external flux Φ_{ext} and a shunting capacitance C_t, is connected to the measurement chain with an input impedance of Z_{L}, where a_{in} (a_{out}) represents the input (output) tone. The two junctions in the dc-SQUID have the Josephson energies E_1 and E_2, respectively.

where $E_{\text{sum}} = E_1 + E_2$, $\varphi_{\text{DC}} = \pi\Phi_{\text{DC}}/\Phi_0$, and $\varphi_{\text{AC}} = \pi\Phi_{\text{AC}}/\Phi_0$. In deriving Eq. (5.15), we use the expression for the Josephson Energy of a dc-SQUID in Eq. (2.13). For simplicity, we assume the dc-SQUID is symmetric and $0 \leq \varphi_{\text{DC}} \leq \pi/2$.

Inserting Eq. (5.15) into Eq. (5.13), and expanding $\cos\varphi$ to order φ^2, we can derive the Hamiltonian for the FJPA,

$$\frac{H_f}{\hbar} = \omega_f a^\dagger a + i\frac{\lambda_f}{2}(a^2 \exp(i\Omega_f t) - h.c.), \tag{5.16}$$

where

$$\omega_f = \frac{1}{\hbar}\sqrt{8E_{\text{C}}E_{\text{sum}}\cos\varphi_{\text{DC}}}, \tag{5.17}$$

$$\lambda_f = \frac{1}{4}\omega_f\varphi_{\text{AC}}\tan\varphi_{\text{DC}}. \tag{5.18}$$

In deriving Eq. (5.16), the operators n and φ are replaced by ladder operators a and $a^\dagger$ defined by the following equations,

$$n = -\frac{i\beta}{\sqrt{2}}(a - a^\dagger), \tag{5.19}$$

$$\varphi = \frac{1}{\sqrt{2}\beta}(a + a^\dagger), \tag{5.20}$$

$$\beta = \left(\frac{E_{\text{sum}}\cos\varphi_{\text{DC}}}{8E_{\text{C}}}\right)^{\frac{1}{4}}. \tag{5.21}$$

In addition, non-RWA terms are neglected with the assumption $\Omega_f \approx 2\omega_f$.

From Eq. (5.18), we find the driving strength $\lambda_f = 0$ when $\varphi_{\text{DC}} = 0$. Specifically, the value of φ_{DC} should be kept away from zero points of the derivative $\partial E_{\text{sq}}(\Phi)/\partial\Phi$. In practice, we usually make $\varphi_{\text{DC}} \approx \pi/4$, i.e., biasing the amplifier at $\Phi_{\text{DC}} \approx \Phi_0/4$.

From Eq. (5.10) and Eq. (5.16), we can find CJPA and FJPA have the same form of Hamiltonian as in Eq. (5.1), thus both types of circuit implementation can function as an amplifier. However, CJPA and FJPA differ with each other in the following aspects:

1. The driving frequencies Ω_c and Ω_f differ by a coefficient 2 in their corresponding Hamiltonians. As a result, when a signal at frequency ω_S needs to be amplified, the CJPA should be driven at $\Omega_c \approx \omega_S$ while the FJPA should be driven at $\Omega_f \approx 2\omega_S$. This is a shortcoming of CJPA, because the closeness in frequency adds to the difficulty in distinguishing the signal tone from the driving tone.

2. The mode frequency of the CJPA ω_c shifts as the driving strength λ_c changes. While for the FJPA, the resonant frequency ω_f can be kept unchanged in tuning the driving strength λ_f. Thus CJPA and FJPA have different strategies in tuning driving strength to achieve the required amplification. In the following sections, we mainly focus on the gain of FJPA. The tuning of the driving strength for CJPA can be found in Ref. [47].

5.3 Gain function and impedance engineering for JPA

Due to the similarity of Hamiltonian, the gain function of CJPA and FJPA can be given in a unified form. For an input signal at angular frequency ω_S, the gain function $G(\omega) \equiv G(\omega_S - \Omega_d)$ is given by [47]

$$G(\omega) = |r(\omega)|^2, \tag{5.22}$$

$$r(\omega) = 1 - \kappa_1(\omega)\frac{-i(\omega + \omega_d - \Delta_2(\omega)) + \kappa_2(\omega)/2}{(-i\Omega(\omega) + \kappa_-(\omega)/2)(-i\Omega(\omega) + \kappa_+(\omega)/2)}, \tag{5.23}$$

where

$$\Omega(\omega) = \omega - (\Delta_1(\omega) + \Delta_2(\omega))/2, \tag{5.24}$$

$$\kappa_\pm(\omega) = (\kappa_1(\omega) + \kappa_2(\omega))/2 \pm 2\sqrt{(\lambda^2 - \omega_d^2) + \epsilon(\omega)}, \tag{5.25}$$

$$\epsilon(\omega) = \omega_d\delta(\omega) - \delta(\omega)^2/4, \tag{5.26}$$

$$\delta(\omega) = (\Delta_2(\omega) - \Delta_1(\omega)) + i(\kappa_1(\omega) - \kappa_2(\omega))/2. \tag{5.27}$$

In the above equations, $\kappa_i(\omega)$ and $\Delta_i(\omega)$ $(i = 1, 2)$ are determined by the input admittance $Y_{\text{in}}(\omega) = 1/Z_{\text{in}}(\omega)$ seen from the JPA side as,

$$\Delta_1(\omega) = -\text{Im}\left(\frac{Y_{\text{in}}(\omega)}{2C_t}\right), \tag{5.28}$$

$$\Delta_2(\omega) = \text{Im}\left(\frac{Y_{\text{in}}(-\omega)}{2C_t}\right), \tag{5.29}$$

$$\kappa_1(\omega) = \text{Re}\left(\frac{Y_{\text{in}}(\omega)}{C_t}\right), \tag{5.30}$$

$$\kappa_2(\omega) = \text{Re}\left(\frac{Y_{\text{in}}(-\omega)}{C_t}\right), \tag{5.31}$$

where C_t is the shunting capacitance in JPA.

In using the gain function $G(\omega)$ in Eq. (5.22), we need to change the definition of variables according to the type of JPA. For a CJPA, we have

$$\Omega_d = \Omega_c, \tag{5.32}$$

$$\lambda = \lambda_c, \tag{5.33}$$

$$\omega_d = \omega_c - \Omega_c = \omega_t - 2\lambda_c - \Omega_c, \tag{5.34}$$

where Ω_c and λ_c are the driving frequency and the driving strength of the CJPA, respectively. The original mode frequency of the CJPA is ω_t, and ω_c is the mode frequency shifted by λ_c. On the contrary, for an FJPA, we have

$$\Omega_d = \Omega_f/2, \tag{5.35}$$

$$\lambda = \lambda_f, \tag{5.36}$$

$$\omega_d = \omega_f - \Omega_f/2, \tag{5.37}$$

where ω_f, Ω_f, and λ_f are the the mode frequency, the driving frequency, and the driving strength of the FJPA, respectively.

We note that in deriving Eq. (5.22), the quantum Langevin equation and the input-output relation in Eq. (5.2) and Eq. (5.3) are generalized. The original equations describe the situation in which the JPA is coupled to a load with a constant real impedance, e.g., a measurement device with a standard impedance 50 Ω. The real impedance, i.e., resistance, results in the damping rates κ of the JPA. In contrast, $G(\omega)$ in Eq. (5.22) describes a generalized situation, in which the JPA is coupled to a load with a complex frequency-dependent impedance $Z_{\text{in}}(\omega)$. The real part of $Z_{\text{in}}(\omega)$ results in the terms $\kappa_1(\omega)$ and $\kappa_2(\omega)$, which lead to the damping of the JPA. While the imaginary part of $Z_{\text{in}}(\omega)$ results in the terms $\Delta_1(\omega)$ and $\Delta_2(\omega)$, which lead to the frequency shift of the JPA. An elaborate derivation for the gain function $G(\omega)$ can be found in Refs. [38, 47].

As $G(\omega)$ dependent of $Z_{\text{in}}(\omega)$, we can consider impedance engineering to improve the performance of JPA. As shown in Fig. 5.3, the impedance engineering is using an impedance transformer to convert the impedance seen by the JPA from the impedance R of the measurement device to a proper impedance $Z_{\text{in}}(\omega)$, for which $G(\omega)$ has a better property. Here our aim is to improve the bandwidth of JPA, that is to say, we hope that $G(\omega)$ keeps constant over a large range of ω. Noticing that $G(\omega)$ is an even function of ω, we can expand it as a power series of ω at $\omega = 0$,

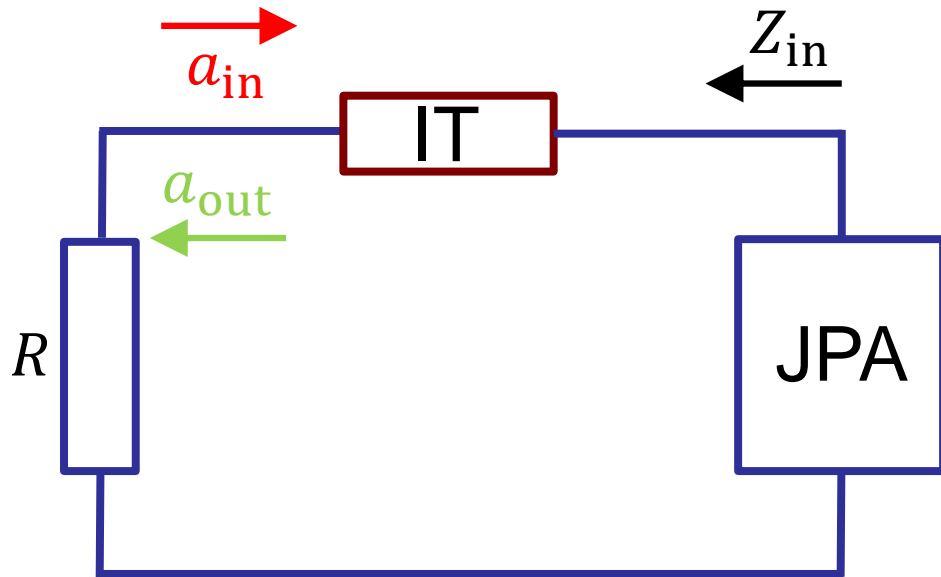$$G(\omega) = G_0 + G_2\omega^2 + G_4\omega^4 + O(\omega^6). \tag{5.38}$$

Figure 5.3: Schematic of an impedance engineered JPA. The impedance engineering is using an impedance transformer (denoted by "IT") to convert the impedance R of the measurement device, resulting in an input impedance Z_{in} seen by the JPA.

From Eq. (5.38), we can find that $G(\omega)$ changes as ω deviates from 0, in which the main factor is the quadratic coefficient G_2. By choosing a proper $Z_{\mathrm{in}}(\omega)$, we can make the coefficient $G_2 = 0$. In this case, the frequency dependence of $G(\omega)$ is dominant by the fourth order term $G_4\omega^4$, which is much smaller than the quadratic term $G_2\omega^2$. As a result, the impedance-engineered JPA has a more flat gain profile than the original one.

5.4 Impedance engineering for the lumped-element FJPA

In this section, we consider a practical example of FJPA, the lumped-element FJPA [46]. The schematic of a lumped-element FJPA is the same as in Fig. 5.2, in which the capacitor C_t is implemented by a lumped element, e.g., a parallel plate capacitor.

First we consider the simplest situation, in which the FJPA is directly connected to the measurement chain with an input impedance $Z_{\mathrm{in}} = R$. Using Eq. (5.22) and Eq. (5.38), we have the zero order gain G_0 as

$$G_0 = 1 + \frac{16\kappa_0^2\lambda_f^2}{(\kappa_0^2 + 4\omega_d^2 - 4\lambda^2)^2}, \tag{5.39}$$

where $\kappa_0 = \kappa_1(\omega) = \kappa_2(\omega) = 1/(C_t R)$ is the damping rates. From Eq. (5.39), we can find that for a given κ_0 and λ, G_0 reaches its maximum when $\omega_d = 0$. Thus we usually let the FJPA operate at $\omega_d = \omega_f - \Omega_f/2 = 0$, i.e., driving the FJPA at $\Omega_f = 2\omega_f$.

We apply the same method of impedance engineering as in Ref. [47] to the FJPA. This strategy is inducing an ω-dependent imaginary part in Z_{in}, i.e., turning Z_{in} into the following form,

$$Z_{\mathrm{in}}(\omega) = R + i\gamma\omega. \tag{5.40}$$

With the above $Z_{\mathrm{in}}(\omega)$, the zero order gain G_0 in Eq. (5.39) is not altered because $Z_{\mathrm{in}}(0) = R$. While the second order coefficient G_2 can be cancelled by properly tuning α and thus the bandwidth of FJPA is improved.

The expression for G_2 when $Z_{\mathrm{in}}(\omega) = R + i\gamma\omega$ is given by

$$G_2 = -128\kappa_0^2\lambda_f^2 \frac{(\kappa_0^2 + 4(\lambda_f^2 - \omega_d^2))(R^2 - R\kappa_0\gamma + (\lambda_f^2 - \omega_d^2)\gamma^2)}{R^2(\kappa_0^2 - 4(\lambda_f^2 - \omega_d^2))^4}. \tag{5.41}$$

We can find that G_2 becomes 0 when γ is the roots of the following equation,

$$R^2 - \kappa_0 R\gamma + (\lambda_f^2 - \omega_d^2)\gamma^2 = 0, \tag{5.42}$$

where the expressions for the roots γ_1 and γ_2 ($\gamma_1 \leq \gamma_2$) are given by

$$\gamma_1 = \frac{R\kappa_0 - R\sqrt{\kappa_0^2 - 4(\lambda_f^2 - \omega_d^2)}}{2(\lambda_f^2 - \omega_d^2)}, \tag{5.43}$$

$$\gamma_2 = \frac{R\kappa_0 + R\sqrt{\kappa_0^2 - 4(\lambda_f^2 - \omega_d^2)}}{2(\lambda_f^2 - \omega_d^2)}. \tag{5.44}$$

From Eq. (5.41), we can find $G_2 < 0$ when $\gamma < \gamma_1$ or $\gamma > \gamma_2$, while $G_2 > 0$ when $\gamma_1 < \gamma < \gamma_2$.

Now we discuss circuit implementing of the impedance transformer which can convert R into $R + i\gamma\omega$. The transmission line (TL) is a good choice for this task. When connected with a load of impedance Z_L, a TL of impedance Z_0 and length (in units of wavenumber) ν can yield the following input impedance [49],

$$Z_{\text{in}}(\omega) = Z_0 \frac{Z_L + iZ_0 \tan(2\pi\nu(1 + \omega/\Omega_0))}{Z_0 + iZ_L \tan(2\pi\nu(1 + \omega/\Omega_0))}, \tag{5.45}$$

where Ω_0 is the design frequency of TL and $\omega = \omega_S - \Omega_0$ is the detuning of the input signal from Ω_0. According to Eq. (5.45), the $\lambda/2$ TL ($\nu = 1/2$) and the $\lambda/4$ TL ($\nu = 1/4$) are useful tools for impedance engineering. When $\omega = 0$, the $\lambda/2$ TL keeps Z_L unchanged, while the $\lambda/4$ TL transforms Z_L into Z_0^2/Z_L. When ω deviates a small value from 0, both the $\lambda/2$ TL and the $\lambda/4$ TL can induce an ω-dependent imaginary part.

In this way, a simple method of impedance engineering is just connecting the measurement device to a $\lambda/2$ TL with impedance $Z_{\lambda/2}$ and design frequency Ω_d, which can transform Z_{in} from R to

$$Z_{\text{in}}(\omega) = R + i\frac{2Z_{\text{aux},\lambda/2}}{\Omega_d}\omega, \tag{5.46}$$

where

$$Z_{\text{aux},\lambda/2} = \frac{\pi Z_{\lambda/2}}{2}\left(1 - \frac{R^2}{Z_{\lambda/2}^2}\right). \tag{5.47}$$

63

Let $R = R_{\mathrm{std}} = 50\ \Omega$, then we can derive the corresponding $Z_{\lambda/2}$ such that $G_2 = 0$.

The problem of the above method is that the solution for $Z_{\lambda/2}$ may exceed our design range of TL. To solve this problem, we can bring in a new design freedom by inserting a $\lambda/4$ TL with impedance $Z_{\lambda/4}$ and design frequency Ω_d between the measurement device and the $\lambda/2$ TL. The main effect of the inserted $\lambda/4$ TL is transforming the real part of Z_{in} from R to $Z_{\lambda/4}^2/R$. Then the following $\lambda/2$ TL can further transform the imaginary part of Z_{in}. As a result, the final Z_{in} after transformation is given by

$$Z_{\mathrm{in}}(\omega) = \frac{Z_{\lambda/4}^2}{R} + i\frac{2Z_{\mathrm{aux}}}{\Omega_d}\omega, \tag{5.48}$$

where

$$Z_{\mathrm{aux}} = \frac{\pi}{4}\left(Z_{\lambda/4}\left(1 - \frac{Z_{\lambda/4}^2}{R^2}\right) + 2Z_{\lambda/2}\left(1 - \frac{Z_{\lambda/4}^4}{R^2 Z_{\lambda/2}^2}\right)\right). \tag{5.49}$$

We note that in changing $Z_{\mathrm{in}}(0)$ from R to $Z_{\lambda/4}^2/R$, the zero order gain G_0 is also affected. Thus we need to tune λ_f accordingly to keep G_0 stay the same before and after transformation.

Now we apply the above theory to a specific FJPA. We take a set of experimentally accessible parameters from Ref. [46] as

$$\omega_f = 2\pi \times 6.7\ \mathrm{GHz}, \tag{5.50}$$
$$C_t = 4\ \mathrm{pF}, \tag{5.51}$$
$$\Omega_d = \frac{\Omega_f}{2} = \omega_f. \tag{5.52}$$

We set a fixed $G_0 = 18$ dB ($x = 10\log(x)$ dB). If we only use a $\lambda/2$ TL as the impedance transformer, the solutions such that $G_2 = 0$ are given by

$$\lambda_f = 2\pi \times 0.351\ \mathrm{GHz}, \tag{5.53}$$
$$Z_{\mathrm{aux},\lambda/2}^{(1)} = 183\ \Omega,\ Z_{\lambda/2}^{(1)} = 135\ \Omega, \tag{5.54}$$
$$Z_{\mathrm{aux},\lambda/2}^{(2)} = 511\ \Omega,\ Z_{\lambda/2}^{(2)} = 333\ \Omega. \tag{5.55}$$

Here we keep $Z_{\mathrm{in}}(0) = R_{\mathrm{std}} = 50\ \Omega$ unchanged.

If we use a $\lambda/4$ TL together with a $\lambda/2$ TL as the impedance transformer, we first need to determine the value of $Z_{\mathrm{in}}(0)$ after transformation. Here we take $Z_{\mathrm{in}}(0) = 32\ \Omega$ as a
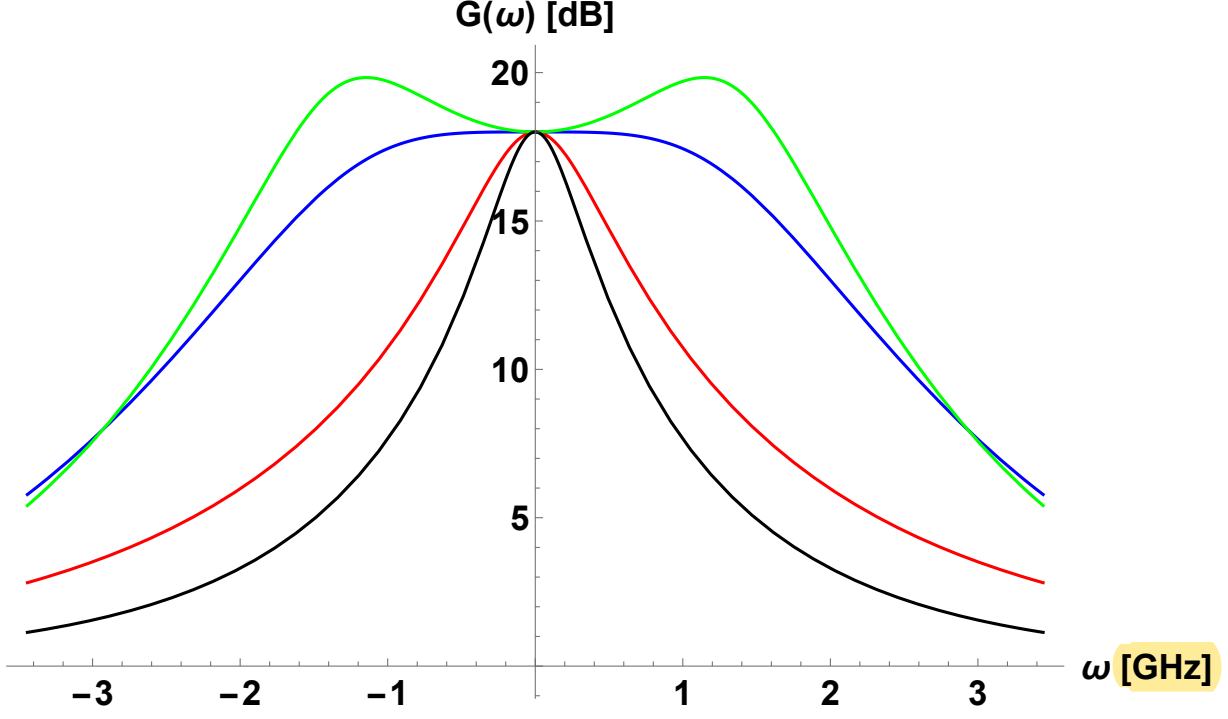
64

Figure 5.4: Gain curves of a lumped-element FJPA. The gain $G(\omega)$ of a lumped-element FJPA is plotted as a function of the signal frequency ω for $Z_{\mathrm{in}} = R_{\mathrm{std}}$ (black), $Z_{\mathrm{in}} = R$ (red), $Z_{\mathrm{in}} = R + i\frac{2Z_{\mathrm{aux}}}{\Omega_d}\omega$ (blue), and $Z_{\mathrm{in}} = R + i\frac{2Z'_{\mathrm{aux}}}{\Omega_d}\omega$ (green), respectively, where the values of R, Z_{aux}, and Z'_{aux} are given in Eqs. (5.59–5.61).

example. In this case, the impedance of the $\lambda/4$ TL should be $Z_{\lambda/4} = \sqrt{R_{\mathrm{std}} Z_{\mathrm{in}}(0)} = 40\ \Omega$. And the solutions such that $G_2 = 0$ are given by

$$\lambda_f = 2\pi \times 8.33\ \text{GHz}, \tag{5.56}$$

$$Z_{\mathrm{aux}}^{(1)} = 117\ \Omega,\ \ Z_{\lambda/2}^{(1)} = 80\ \Omega, \tag{5.57}$$

$$Z_{\mathrm{aux}}^{(2)} = 327\ \Omega,\ \ Z_{\lambda/2}^{(2)} = 206\ \Omega. \tag{5.58}$$

For a TL implemented via a coplanar waveguide, our design range for impedance is about 30–90 Ω. From the above numerical results, we can find that using both the $\lambda/4$ and $\lambda/2$ TL generates more feasible solutions than only using the $\lambda/2$ TL.

In Fig 5.4, we plot the gain $G(\omega)$ as a function of ω for $Z_{\mathrm{in}} = R_{\mathrm{std}}$ (black), $Z_{\mathrm{in}} = R$ (red), $Z_{\mathrm{in}} = R + i\frac{2Z_{\mathrm{aux}}}{\Omega_d}\omega$ (blue), and $Z_{\mathrm{in}} = R + i\frac{2Z'_{\mathrm{aux}}}{\Omega_d}\omega$ (green), respectively. Here R, Z_{aux},

and Z'_{aux} are given by the solutions in Eq. (5.57) as

$$R = 32 \ \Omega, \tag{5.59}$$

$$Z_{\text{aux}} = Z_{\text{aux}}^{(1)} = 117 \ \Omega, \tag{5.60}$$

$$Z'_{\text{aux}} = 1.2 Z_{\text{aux}}. \tag{5.61}$$

To compare the effects of impedance engineering, we tune the λ_f for each gain curve in Fig 5.4, respectively, making all curves have the same $G_0 = 18$ dB. For the black curve that $Z_{\text{in}} = R_{\text{std}}$, λ_f is set as the value given in Eq. (5.53). For the rest three curves (red, blue, and green), λ_f is set as the value given in Eq. (5.56).

From Fig 5.4, we can find that the impedance engineered gain curve (blue) is much flatter than the original case (black) or the one with a smaller real impedance. We note that the key point of impedance engineering is altering the imaginary part of Z_{in} to an optimal value, but not simply decreasing the real part of Z_{in}. The green curve in Fig 5.4 shows the over-engineered situation. The corresponding $\gamma' = 2Z'_{\text{aux}}/\Omega_d$ falls in between the two roots γ_1 and γ_2 of Eq. (5.42), which makes $G_2 > 0$. In this case, the gain will first increase and then decrease as ω deviates from 0.

5.5   Impedance engineering for the transmission line FJPA

In Sec. 5.4, we discuss impedance engineering for the lumped-element FJPA. Here we consider another type of FJPA, the TL FJPA [50], which consists of a dc-SQUID connected with a $\lambda/4$ TL. The advantage of the TL FJPA is that it has multiple resonant modes, in which the parametric amplification can be realized across different modes. Here we only discuss the situation in which the TL FJPA works as a 1-mode, 1-port amplifier. We choose one resonant mode of the TL FJPA with the angular frequency ω_f and the corresponding effective shunting capacitance C_t. In addition, we drive this TL FJPA with the frequency $\Omega_f = 2\Omega_d$ and the driving strength λ_f. In this case, we can still use the theoretical model given in Sec. 5.3 to describe the TL FJPA.

As shown in Fig. 5.5, the TL FJPA is coupled with the external circuit with a small coupling capacitor C_c (10–100 fF). The capacitor C_c makes the input impedance seen by the TL FJPA differ largely from that of a lumped-element FJPA. Thus we need to figure out new methods of impedance engineering for this type of FJPA.
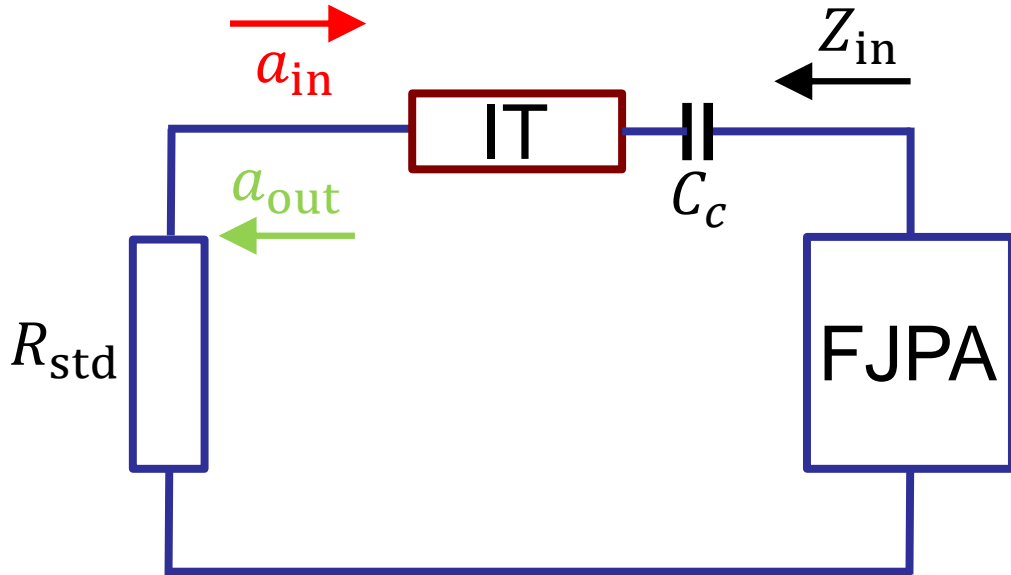
Figure 5.5: Schematic of a TL FJPA. The TL FJPA can be effectively modelled by a single mode FJPA in Fig. 5.2 connected to the measurement chain via a small coupling capacitor C_c. The impedance transformer (denoted by "IT") is inserted between the measurement device with an impedance R_{std} and the coupling capacitor C_c.

The impedance of C_c at the signal frequency ω_S can be expanded as

$$Z_C = \frac{1}{i\omega_S C_c} = -iZ_{C0} + i\frac{Z_{C0}}{\Omega_d}\omega, \tag{5.62}$$

where $\omega = \omega_S - \Omega_d$ and $Z_{C0} = 1/(C_c\Omega_d)$. The impedance transformer is inserted between the measurement device and C_c, which converts the input impedance from R_{std} to $R + i\frac{2Z_{\mathrm{aux}}}{\Omega_d}\omega$. Finally, the input impedance $Z_{\mathrm{in}}(\omega)$ seen by the TL FJPA is given by

$$Z_{\mathrm{in}}(\omega) = R - iZ_{C0} + i\frac{2Z_{\mathrm{aux}} + Z_{C0}}{\Omega_d}\omega. \tag{5.63}$$

For the above $Z_{\mathrm{in}}(\omega)$, the zero order gain G_0 is given by

$$G_0 = 1 + \frac{16C_t^2 Z_{\mathrm{re}}^2 \lambda_f^2}{(1 + 4C_t Z_{\mathrm{im}}\omega_d - 4C_t^2(Z_{\mathrm{re}}^2 + Z_{\mathrm{im}}^2)(\lambda_f^2 - \omega_d^2))^2}, \tag{5.64}$$

where $Z_{\mathrm{re}} = \mathrm{Re}(Z_{\mathrm{in}}(0)) = R$, $Z_{\mathrm{im}} = \mathrm{Im}(Z_{\mathrm{in}}(0)) = -Z_{C0}$, and $\omega_d = \omega_f - \Omega_f/2$. Similar to Eq. (5.39), G_0 reaches its maximum when $\omega_d = 0$. Thus it is still optimal to drive a TL FJPA at the frequency $\Omega_f = 2\omega_f$. The expression of G_2 for the TL FJPA is much more complicated than that in Eq. (5.41). While we know qualitatively that G_2 is a function of the following form

$$G_2 = G_2(R, Z_{\mathrm{aux}}, Z_{C0}, C_t, \omega_d, \lambda_f). \tag{5.65}$$

Now we discuss the method of impedance engineering. For a lumped-element FJPA, the original Z_{in} only have the real part. We mainly engineer the imaginary part of Z_{in}, making it "match" with the real part of Z_{in} and cancel G_2. While for a TL FJPA, the original Z_{in} is dominated by the imaginary impedance Z_C induced by the capacitor C_c, which can hardly be compensated by an impedance transformer with limited design range. Thus we conversely engineer the real part of Z_{in}, making it match with the imaginary part of Z_{in} and cancel G_2. As shown in Sec. 5.4, this task can be done by a $\lambda/4$ TL of impedance $Z_{\lambda/4}$ and design frequency Ω_d, which transforms Z_{in} from R to

$$Z_{\mathrm{in}} = \frac{Z_{\lambda/4}^2}{R} + i\frac{2Z_{\mathrm{aux},\lambda/4}}{\Omega_d}\omega, \tag{5.66}$$

where

$$Z_{\mathrm{aux},\lambda/4} = \frac{\pi Z_{\lambda/4}}{4}\left(1 - \frac{Z_{\lambda/4}^2}{R^2}\right). \tag{5.67}$$

68

Besides the above equations, we add another condition that $G_0 = g_0$ is a fixed value. Combining this condition with the expressions G_0 in Eq. (5.64) and G_2 in Eq. (5.65), we can derive $Z_{\lambda/4}$ and the driving strength λ_f by solving the following equation set,

$$G_2(R, Z_{\text{aux}}, Z_{C0}, C_t, \omega_d, \lambda_f) = 0, \tag{5.68}$$

$$R = \frac{Z_{\lambda/4}^2}{R_{\text{std}}}, \tag{5.69}$$

$$Z_{\text{aux}} = \frac{\pi Z_{\lambda/4}}{4}\left(1 - \frac{Z_{\lambda/4}^2}{R_{\text{std}}^2}\right), \tag{5.70}$$

$$G_0(R, Z_{C0}, C_t, \omega_d, \lambda_f) = g_0. \tag{5.71}$$

Now we apply the above analysis to a specific FJPA with the following experimentally accessible parameters

$$\omega_f = 2\pi \times 6 \text{ GHz}, \tag{5.72}$$

$$C_t = 1.62 \text{ pF}, \tag{5.73}$$

$$C_c = 100 \text{ fF}, \tag{5.74}$$

$$\Omega_d = \frac{\Omega_f}{2} = \omega_f. \tag{5.75}$$

We set a fixed $G_0 = 20$ dB. For the original case without impedance engineering, we have $\lambda_f = 2\pi \times 0.178$ GHz. For the case in which the impedance is engineered by a $\lambda/4$ TL, we have the following solution,

$$\lambda_f = 2\pi \times 0.182 \text{ GHz}, \tag{5.76}$$

$$Z_{\lambda/4} = 38.9 \ \Omega, \tag{5.77}$$

$$R = 30.2 \ \Omega. \tag{5.78}$$

In Fig. 5.6, we plot the gain $G(\omega)$ as a function of ω for the original case (red) and the impedance engineered case (blue) using the above parameters. We find that the impedance engineered gain curve is much flatter than that of the original case.

5.6   Summary

In this chapter, we study impedance engineering for the Josephson parametric amplifier to achieve a broadband gain profile. The principle of impedance engineering is to engineer
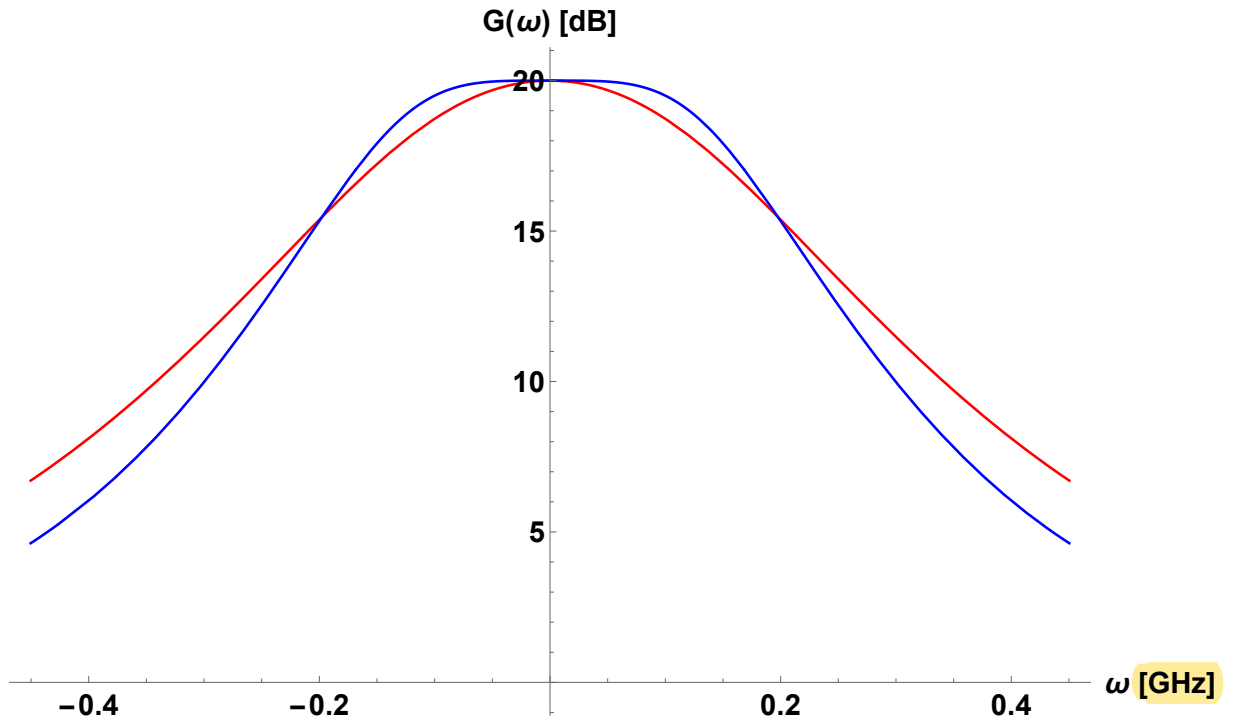
Figure 5.6: Gain curves of a TL FJPA. The gain $G(\omega)$ of a TL FJPA is plotted as a function of the signal frequency ω for the original case (red) and the impedance engineered case (blue).

the input impedance seen by the JPA to decrease the frequency dependence of the gain function. We apply the impedance engineering method to two different types of FJPA, the lump-element FJPA and the TL FJPA.

For the lump-element FJPA, the method of impedance engineering is inducing a frequency-dependent imaginary part in the input impedance and matching it with the real part of input impedance. We use a $\lambda/4$ TL together with a $\lambda/2$ TL as the impedance transformer to implement this impedance engineering, in which the main function of the former (latter) TL is engineering the real (imaginary) part of the input impedance.

For the TL FJPA, the method of impedance engineering is transforming the real part of the input impedance and matching it with the imaginary part of input impedance. We use a $\lambda/4$ TL as the impedance transformer implement this impedance engineering.

Chapter 6

Conclusion

6.1 Conclusion for tunable coupler in superconducting circuits

We studied the circuit implementation for the Xmon tunable coupler between two transmission line resonators. We design a specific chip layout for the tunable coupler and derive its Hamiltonian via the formal circuit quantization method. We obtain the electromagnetic parameters of the chip and determine the fabrication parameters of the Josephson junctions on the chip. From the numerical simulation of the eigenenergies and the eigenstates of the Hamiltonian of the chip, we confirm that the tunable coupling with a turn-off point can be realized on the chip.

For future studies, the near-term task is to experimentally demonstrate the tunable coupling with a turn-off point on the chip fabricated with the parameters in this thesis. Another task needs be done is to characterize the Xmon using the XY control line and the resonator R_m. From the measurement results of the Xmon, we can check whether the parameters used in designing the chip, e.g., the current density of the Josephson junction, agree with the actual situation in fabrication, and update them for the following design.

After doing this, we can remove the resonator R_m in the second version of the tunable coupler to avoid its perturbation to R_a and R_b. In addition, without R_m, the frequency of the Xmon can be further tuned down to achieve a larger effective coupling between R_a and R_b. Besides, in the second version of the tunable coupler, the EM parameters of the R_a, R_b and the Xmon can also be optimized to increase the tuning range of the coupling strength.

In the third version of the tunable coupler, we can couple each resonator with an Xmon to realize single qubit operations. Combining the single qubit operations with the tunable coupler, we can implement two-qubit gates on the composite system of R_a and R_b, which realizes the proposal in Ref. [35].

6.2   Conclusion for impedance engineering for JPA

We studied impedance engineering for the Josephson parametric amplifier to achieve a broadband gain profile. The principle of impedance engineering is to engineer the input impedance seen by the JPA to decrease the frequency dependence of the gain function, which can be implemented by using the transmission lines as impedance transformers. We note that the key point of impedance engineering is letting the frequency-independent and the frequency-dependent part of the input impedance match with each other.

For the lump-element flux pumping JPA, where the input impedance is dominated by its frequency-independent real part, the method of impedance engineering is inducing a frequency-dependent imaginary part in the input impedance and matching it with the real part.

For the transmission line flux pumping JPA, where the input impedance is dominated by its frequency-dependent imaginary part, the method of impedance engineering is transforming the frequency-independent real part of the input impedance and matching it with the imaginary part.

For future studies, we can consider the following three directions. The first direction is to experimentally demonstrate the impedance engineering for a TL FJPA according to the theoretical model given in Sec. 5.5. First we need to obtain the actual input impedance of the measurement chain, and the parameters of the TL FJPA. Then we can design the impedance transformer accordingly.

The second direction is to optimize the design of impedance transformers. For example, the tapered transmission line used in Ref. [46] is a better choice than the transformer in Ref. [47] consisting of a $\lambda/4$ TL and a $\lambda/2$ TL. Because the characteristic impedance of the former one changes in a continuous manner. However, the tapered TL may not have a simple analytical expression to describe its property as an impedance transformer. In this case, we can obtain the optimal design of the TL via numerical simulation.

The third direction is to engineer the impedance for a TL FJPA operating in multiple resonant modes. The TL FJPA can operate across different modes, in which the signal

tone and the idler tone are located at two different resonant modes of the TL FJPA. First, we need to derive the gain function for the TL FJPA operating in multiple modes. Then we can study how to improve the gain function by transforming the input impedance seen by the TL FJPA.

References

[1] G. Wendin. Quantum information processing with superconducting circuits: a review. *Reports on Progress in Physics*, 80(10):106001, 2017.

[2] Xiu Gu, Anton Frisk Kockum, Adam Miranowicz, Yu-xi Liu, and Franco Nori. Microwave photonics with superconducting quantum circuits. *Physics Reports*, 718-719:1–102, November 2017.

[3] Morten Kjaergaard, Mollie E. Schwartz, Jochen Braumüller, Philip Krantz, Joel I.-J. Wang, Simon Gustavsson, and William D. Oliver. Superconducting Qubits: Current State of Play. *Annual Review of Condensed Matter Physics*, 11(1):369–395, March 2020. Publisher: Annual Reviews.

[4] Frank Arute, Kunal Arya, Ryan Babbush, Dave Bacon, Joseph C. Bardin, Rami Barends, Rupak Biswas, Sergio Boixo, Fernando G. S. L. Brandao, David A. Buell, Brian Burkett, Yu Chen, Zijun Chen, Ben Chiaro, Roberto Collins, William Courtney, Andrew Dunsworth, Edward Farhi, Brooks Foxen, Austin Fowler, Craig Gidney, Marissa Giustina, Rob Graff, Keith Guerin, Steve Habegger, Matthew P. Harrigan, Michael J. Hartmann, Alan Ho, Markus Hoffmann, Trent Huang, Travis S. Humble, Sergei V. Isakov, Evan Jeffrey, Zhang Jiang, Dvir Kafri, Kostyantyn Kechedzhi, Julian Kelly, Paul V. Klimov, Sergey Knysh, Alexander Korotkov, Fedor Kostritsa, David Landhuis, Mike Lindmark, Erik Lucero, Dmitry Lyakh, Salvatore Mandrà, Jarrod R. McClean, Matthew McEwen, Anthony Megrant, Xiao Mi, Kristel Michielsen, Masoud Mohseni, Josh Mutus, Ofer Naaman, Matthew Neeley, Charles Neill, Murphy Yuezhen Niu, Eric Ostby, Andre Petukhov, John C. Platt, Chris Quintana, Eleanor G. Rieffel, Pedram Roushan, Nicholas C. Rubin, Daniel Sank, Kevin J. Satzinger, Vadim Smelyanskiy, Kevin J. Sung, Matthew D. Trevithick, Amit Vainsencher, Benjamin Villalonga, Theodore White, Z. Jamie Yao, Ping Yeh, Adam Zalcman, Hartmut Neven, and John M. Martinis. Quantum supremacy using a programmable superconducting processor. *Nature*, 574(7779):505–510, October 2019.

[5] Austin G. Fowler, Matteo Mariantoni, John M. Martinis, and Andrew N. Cleland. Surface codes: Towards practical large-scale quantum computation. *Physical Review A*, 86(3):032324, September 2012.

[6] J. Kelly, R. Barends, A. G. Fowler, A. Megrant, E. Jeffrey, T. C. White, D. Sank, J. Y. Mutus, B. Campbell, Yu Chen, Z. Chen, B. Chiaro, A. Dunsworth, I.-C. Hoi, C. Neill, P. J. J. O'Malley, C. Quintana, P. Roushan, A. Vainsencher, J. Wenner, A. N. Cleland, and John M. Martinis. State preservation by repetitive error detection in a superconducting quantum circuit. *Nature*, 519(7541):66–69, March 2015.

[7] Zaki Leghtas, Gerhard Kirchmair, Brian Vlastakis, Robert J. Schoelkopf, Michel H. Devoret, and Mazyar Mirrahimi. Hardware-Efficient Autonomous Quantum Memory Protection. *Physical Review Letters*, 111(12):120501, September 2013.

[8] Nissim Ofek, Andrei Petrenko, Reinier Heeres, Philip Reinhold, Zaki Leghtas, Brian Vlastakis, Yehan Liu, Luigi Frunzio, S. M. Girvin, L. Jiang, Mazyar Mirrahimi, M. H. Devoret, and R. J. Schoelkopf. Extending the lifetime of a quantum bit with error correction in superconducting circuits. *Nature*, 536(7617):441–445, August 2016.

[9] Y. Nakamura, Yu. A. Pashkin, and J. S. Tsai. Rabi Oscillations in a Josephson-Junction Charge Two-Level System. *Physical Review Letters*, 87(24):246601, November 2001.

[10] William D. Oliver, Yang Yu, Janice C. Lee, Karl K. Berggren, Leonid S. Levitov, and Terry P. Orlando. Mach-Zehnder Interferometry in a Strongly Driven Superconducting Qubit. *Science*, 310(5754):1653–1657, September 2005.

[11] S. Novikov, T. Sweeney, J. E. Robinson, S. P. Premaratne, B. Suri, F. C. Wellstood, and B. S. Palmer. Raman coherence in a circuit quantum electrodynamics lambda system. *Nature Physics*, advance online publication, November 2015.

[12] Xiu Gu, Sai-Nan Huai, Franco Nori, and Yu-xi Liu. Polariton states in circuit QED for electromagnetically induced transparency. *Physical Review A*, 93(6):063827, June 2016.

[13] P. Forn-Díaz, J. J. García-Ripoll, B. Peropadre, J.-L. Orgiazzi, M. A. Yurtalan, R. Belyansky, C. M. Wilson, and A. Lupascu. Ultrastrong coupling of a single artificial atom to an electromagnetic continuum in the nonperturbative regime. *Nature Physics*, advance online publication, October 2016.

[14] Herbert Walther, Benjamin T. H. Varcoe, Berthold-Georg Englert, and Thomas Becker. Cavity quantum electrodynamics. *Reports on Progress in Physics*, 69(5):1325–1382, April 2006. Publisher: IOP Publishing.

[15] Alexandre Blais, Ren-Shou Huang, Andreas Wallraff, S. M. Girvin, and R. J. Schoelkopf. Cavity quantum electrodynamics for superconducting electrical circuits: An architecture for quantum computation. *Phys. Rev. A*, 69(6):062320, June 2004.

[16] Alexandre Blais, Steven M. Girvin, and William D. Oliver. Quantum information processing and quantum optics with circuit quantum electrodynamics. *Nature Physics*, pages 1–10, March 2020. Publisher: Nature Publishing Group.

[17] Alexandre Blais, Arne L. Grimsmo, S. M. Girvin, and Andreas Wallraff. Circuit Quantum Electrodynamics. *arXiv:2005.12667 [quant-ph]*, May 2020. arXiv: 2005.12667.

[18] C. M. Wilson, G. Johansson, A. Pourkabirian, M. Simoen, J. R. Johansson, T. Duty, F. Nori, and P. Delsing. Observation of the dynamical Casimir effect in a superconducting circuit. *Nature*, 479:376, 2011.

[19] Z. K. Minev, S. O. Mundhada, S. Shankar, P. Reinhold, R. Gutierrez-Jauregui, R. J. Schoelkopf, M. Mirrahimi, H. J. Carmichael, and M. H. Devoret. To catch and reverse a quantum jump mid-flight. *arXiv:1803.00545 [quant-ph]*, March 2018. arXiv: 1803.00545.

[20] Y. P. Zhong, H.-S. Chang, K. J. Satzinger, M.-H. Chou, A. Bienfait, C. R. Conner, É Dumur, J. Grebel, G. A. Peairs, R. G. Povey, D. I. Schuster, and A. N. Cleland. Violating Bell's inequality with remotely connected superconducting qubits. *Nature Physics*, 15(8):741–744, August 2019. Number: 8 Publisher: Nature Publishing Group.

[21] R. C. Jaklevic, John Lambe, A. H. Silver, and J. E. Mercereau. Quantum Interference Effects in Josephson Tunneling. *Physical Review Letters*, 12(7):159–160, February 1964. Publisher: American Physical Society.

[22] A. A. Clerk, M. H. Devoret, S. M. Girvin, Florian Marquardt, and R. J. Schoelkopf. Introduction to quantum noise, measurement, and amplification. *Reviews of Modern Physics*, 82(2):1155–1208, April 2010.

[23] Ananda Roy and Michel Devoret. Introduction to parametric amplification of quantum signals with Josephson circuits. *Comptes Rendus Physique*, 17(7):740–755, August 2016.

[24] B. D. Josephson. The discovery of tunnelling supercurrents. *Rev. Mod. Phys.*, 46(2):251–254, April 1974.

[25] Vinay Ambegaokar and Alexis Baratoff. Tunneling Between Superconductors. *Physical Review Letters*, 10(11):486–489, June 1963. Publisher: American Physical Society.

[26] M. Tinkham. *Introduction to superconductivity*. Dover Publications Inc., 2 edition, 2004.

[27] Jens Koch, Terri M. Yu, Jay Gambetta, A. A. Houck, D. I. Schuster, J. Majer, Alexandre Blais, M. H. Devoret, S. M. Girvin, and R. J. Schoelkopf. Charge-insensitive qubit design derived from the Cooper pair box. *Phys. Rev. A*, 76(4):042319, October 2007.

[28] J. A. Schreier, A. A. Houck, Jens Koch, D. I. Schuster, B. R. Johnson, J. M. Chow, J. M. Gambetta, J. Majer, L. Frunzio, M. H. Devoret, S. M. Girvin, and R. J. Schoelkopf. Suppressing charge noise decoherence in superconducting charge qubits. *Phys. Rev. B*, 77(18):180502, May 2008.

[29] R. Barends, J. Kelly, A. Megrant, A. Veitia, D. Sank, E. Jeffrey, T. C. White, J. Mutus, A. G. Fowler, B. Campbell, Y. Chen, Z. Chen, B. Chiaro, A. Dunsworth, C. Neill, P. O'Malley, P. Roushan, A. Vainsencher, J. Wenner, A. N. Korotkov, A. N. Cleland, and John M. Martinis. Superconducting quantum circuits at the surface code threshold for fault tolerance. *Nature*, 508(7497):500–503, April 2014.

[30] Alec Maassen van den Brink, A. J. Berkley, and M. Yalowsky. Mediated tunable coupling of flux qubits. *New Journal of Physics*, 7(1):230, 2005.

[31] Yu Chen, C. Neill, P. Roushan, N. Leung, M. Fang, R. Barends, J. Kelly, B. Campbell, Z. Chen, B. Chiaro, A. Dunsworth, E. Jeffrey, A. Megrant, J. Y. Mutus, P. J. J. O'Malley, C. M. Quintana, D. Sank, A. Vainsencher, J. Wenner, T. C. White, Michael R. Geller, A. N. Cleland, and John M. Martinis. Qubit Architecture with High Coherence and Fast Tunable Coupling. *Physical Review Letters*, 113(22):220502, November 2014. Publisher: American Physical Society.

[32] A. Baust, E. Hoffmann, M. Haeberlein, M. J. Schwarz, P. Eder, J. Goetz, F. Wulschner, E. Xie, L. Zhong, F. Quijandría, B. Peropadre, D. Zueco, J.-J. García Ripoll, E. Solano, K. Fedorov, E. P. Menzel, F. Deppe, A. Marx, and R. Gross. Tunable and switchable coupling between two superconducting resonators. *Physical Review B*, 91(1):014515, January 2015.

[33] David C. McKay, Stefan Filipp, Antonio Mezzacapo, Easwar Magesan, Jerry M. Chow, and Jay M. Gambetta. Universal Gate for Fixed-Frequency Qubits via a Tunable Bus. *Physical Review Applied*, 6(6):064007, December 2016. Publisher: American Physical Society.

[34] Fei Yan, Philip Krantz, Youngkyu Sung, Morten Kjaergaard, Daniel L. Campbell, Terry P. Orlando, Simon Gustavsson, and William D. Oliver. Tunable Coupling Scheme for Implementing High-Fidelity Two-Qubit Gates. *Physical Review Applied*, 10(5):054062, November 2018.

[35] Frederick W. Strauch and Matteo Mariantoni. Multiphoton Quantum Logic Gates for Superconducting Resonators with Tunable Nonlinear Interaction. *arXiv:1807.03820 [quant-ph]*, July 2018. arXiv: 1807.03820.

[36] X. Li, T. Cai, H. Yan, Z. Wang, X. Pan, Y. Ma, W. Cai, J. Han, Z. Hua, X. Han, Y. Wu, H. Zhang, H. Wang, Yipu Song, Luming Duan, and Luyan Sun. A tunable coupler for suppressing adjacent superconducting qubit coupling. *arXiv:1912.10721 [quant-ph]*, January 2020. arXiv: 1912.10721.

[37] Alexandre Blais, Jay Gambetta, A. Wallraff, D. I. Schuster, S. M. Girvin, M. H. Devoret, and R. J. Schoelkopf. Quantum-information processing with circuit quantum electrodynamics. *Physical Review A*, 75(3):032329, March 2007. Publisher: American Physical Society.

[38] Uri Vool and Michel Devoret. Introduction to quantum electromagnetic circuits. *International Journal of Circuit Theory and Applications*, 45(7):897–934, July 2017.

[39] G. J. Dolan. Offset masks for lift-off photoprocessing. *Applied Physics Letters*, 31(5):337–339, September 1977. Publisher: American Institute of Physics.

[40] R. K. Naik, N. Leung, S. Chakram, Peter Groszkowski, Y. Lu, N. Earnest, D. C. McKay, Jens Koch, and D. I. Schuster. Random access quantum information processors using multimode circuit quantum electrodynamics. *Nature Communications*, 8(1):1–7, December 2017.

[41] Andrei Vrajitoarea, Ziwen Huang, Peter Groszkowski, Jens Koch, and Andrew A. Houck. Quantum control of an oscillator using a stimulated Josephson nonlinearity. *Nature Physics*, pages 1–7, November 2019.

[42] M. Hatridge, R. Vijay, D. H. Slichter, John Clarke, and I. Siddiqi. Dispersive magnetometry with a quantum limited SQUID parametric amplifier. *Physical Review B*, 83(13):134501, April 2011. Publisher: American Physical Society.

[43] J. Y. Mutus, T. C. White, E. Jeffrey, D. Sank, R. Barends, J. Bochmann, Yu Chen, Z. Chen, B. Chiaro, A. Dunsworth, J. Kelly, A. Megrant, C. Neill, P. J. J. O'Malley, P. Roushan, A. Vainsencher, J. Wenner, I. Siddiqi, R. Vijay, A. N. Cleland, and John M. Martinis. Design and characterization of a lumped element single-ended superconducting microwave parametric amplifier with on-chip flux bias line. *Applied Physics Letters*, 103(12):122602, September 2013. Publisher: American Institute of Physics.

[44] C. Macklin, K. O'Brien, D. Hover, M. E. Schwartz, V. Bolkhovsky, X. Zhang, W. D. Oliver, and I. Siddiqi. A near–quantum-limited Josephson traveling-wave parametric amplifier. *Science*, 350(6258):307–310, October 2015. Publisher: American Association for the Advancement of Science Section: Report.

[45] T. C. White, J. Y. Mutus, I.-C. Hoi, R. Barends, B. Campbell, Yu Chen, Z. Chen, B. Chiaro, A. Dunsworth, E. Jeffrey, J. Kelly, A. Megrant, C. Neill, P. J. J. O'Malley, P. Roushan, D. Sank, A. Vainsencher, J. Wenner, S. Chaudhuri, J. Gao, and John M. Martinis. Traveling wave parametric amplifier with Josephson junctions using minimal resonator phase matching. *Applied Physics Letters*, 106(24):242601, June 2015. Publisher: American Institute of Physics.

[46] J. Y. Mutus, T. C. White, R. Barends, Yu Chen, Z. Chen, B. Chiaro, A. Dunsworth, E. Jeffrey, J. Kelly, A. Megrant, C. Neill, P. J. J. O'Malley, P. Roushan, D. Sank, A. Vainsencher, J. Wenner, K. M. Sundqvist, A. N. Cleland, and John M. Martinis. Strong environmental coupling in a Josephson parametric amplifier. *Applied Physics Letters*, 104(26):263513, June 2014.

[47] Tanay Roy, Suman Kundu, Madhavi Chand, A. M. Vadiraj, A. Ranadive, N. Nehra, Meghan P. Patankar, J. Aumentado, A. A. Clerk, and R. Vijay. Broadband parametric amplification with impedance engineering: Beyond the gain-bandwidth product. *Applied Physics Letters*, 107(26):262601, December 2015.

[48] C. Gardiner, P. Zoller, and P. Zoller. *Quantum Noise: A Handbook of Markovian and Non-Markovian Quantum Stochastic Methods with Applications to Quantum Optics*. Springer Series in Synergetics. Springer, 2004.

[49] D.M. Pozar. *Microwave Engineering, 4th Edition*. Wiley, 2011.

[50] M. Simoen, C. W. S. Chang, P. Krantz, Jonas Bylander, W. Wustmann, V. Shumeiko, P. Delsing, and C. M. Wilson. Characterization of a multimode coplanar waveguide parametric amplifier. *Journal of Applied Physics*, 118(15):154501, October 2015.

APPENDICES

Appendix A

Fabrication process flow

1. Marker and bonding pads layer (Palladium)

   (a) Piranha cleaning

   (b) Resist coating

   (c) UV lithography

   (d) Development

   (e) E-beam PVD

   (f) Lift off

2. Circuit layer (Aluminum)

   (a) RCA1 cleaning

   (b) HF cleaning

   (c) E-beam PVD

   (d) Spin coating

   (e) UV lithography

   (f) Development

   (g) Wet etching

   (h) Resist cleaning

3. Wafer dicing

    (a) Spin coating

    (b) Dicing

    (c) Resist cleaning

4. Junction layer

    (a) Spin coating

    (b) E-beam lithography

    (c) E-beam PVD

    (d) Lift off

5. Block dicing

    (a) Spin coating

    (b) Dicing

    (c) Resist clean

Appendix B

Codes for simulating the RXR chip

```
##############################################################
# Python codes for simulating the RXR chip
# Author: Huichen Sun
##############################################################

from qutip import *
import numpy as np
import scipy.special as sp
import scipy.integrate as si
import matplotlib.pyplot as plt


# Function Even check
def EvenQ(number):
        return number % 2 == 0


# Function En/Ec of Level n
def EnXm(n,rJC):
  if EvenQ(n):
    return sp.mathieu_a(n,-rJC/2)-sp.mathieu_a(0,-rJC/2)
  else:
    return sp.mathieu_b(n+1,-rJC/2)-sp.mathieu_a(0,-rJC/2)
```

```python
# Function Psi(phi) of Level n
def PsiN(n,rJC,phi):
  Rrad=180/np.pi;
  if EvenQ(n):
    return sp.mathieu_cem(n,-rJC/2,phi*Rrad/2)[0]/np.sqrt(np.pi)
  else:
    return sp.mathieu_sem(n+1,-rJC/2,phi*Rrad/2)[0]/np.sqrt(np.pi)
  # scipy mathieu function take phi(deg) as input,
  # but still regard phi(rad) as its independent variable
  # 1/np.sqrt(np.pi): normalization coefficient


# Function d_Psi(phi)/d_phi of Level n
def PsiNP(n,rJC,phi):
  Rrad=180/np.pi;
  if EvenQ(n):
    return sp.mathieu_cem(n,-rJC/2,phi*Rrad/2)[1]/np.sqrt(np.pi)/2
  else:
    return sp.mathieu_sem(n+1,-rJC/2,phi*Rrad/2)[1]/np.sqrt(np.pi)/2
  # scipy mathieu derivative function take phi(deg) as input,
  # but still regard phi(rad) as its independent variable


# Function Tij
def FTij(rJC,i,j):
  fphi=lambda phi:PsiN(i,rJC,phi) * PsiNP(j,rJC,phi)
  return si.quad(fphi,0,2*np.pi)[0]


# Function En/Ec Matrix of Xmon
def FXEmat(rJC):
  return qdiags([0,EnXm(1,rJC),EnXm(2,rJC)],0)


# Function Transition Matrix of Xmon
def FXTmat(rJC):
  TList=np.array([FTij(rJC,0,1),FTij(rJC,1,2)])
```

```
    return qdiags(TList,1)+qdiags(-TList,-1)


# Function Total Hm of System
def HTotal(rJC):
  Tmat=FXTmat(rJC)
  return (GpEa*HaM+GpEb*HbM+GpEm*HmM+tensor(IC3,GpEcx*FXEmat(rJC))
  +GpEab*HabM +GpEam*HamM +GpEbm*HbmM
  +GpExa*tensor(QII,Tmat)+GpExb*tensor(IQI,Tmat)+GpExm*tensor(IIQ,Tmat))


# Function First N eigenenergies of HTotal
def EnHt(rJC,N):
  return HTotal(rJC).eigenenergies(eigvals=N)


# Function First N eigenenergies of HTotal for Array rJCV
def EnHtV(rJCV,N):
  EnHtV=np.zeros(N)
  for rJC in rJCV:
    EnHtV=np.vstack((EnHtV,EnHt(rJC,N)))
  return np.delete(EnHtV,0,0)


# Function states probability for eigenmodes of Ra & Rb
def EnRab(rJC):
  pArray=np.array([0,0,0,0],dtype = "complex_")
  EigenV=HTotal(rJC).eigenstates(eigvals=3)[1]
  pArray[0]=EigenV[1][48,0]
  pArray[1]=EigenV[1][12,0]
  pArray[2]=EigenV[2][48,0]
  pArray[3]=EigenV[2][12,0]
  return abs(pArray)**2


# Function states probability for eigenmodes of Ra & Rb for vector rJCV
def EnRabV(rJCV):
  pVMat=np.zeros(4)
```

```
  for rJC in rJCV:
    pVMat=np.vstack((pVMat,EnRab(rJC)))
  return np.delete(pVMat,0,0)



# Function derive rJC and flux from a certain f01, Ec, and rJCmax
def FrJC(f01,Ec,rJCmax):
  rJC=(Ec+f01)**2/8/Ec**2;
  flux=np.arccos(rJC/rJCmax);
  return [rJC,flux]



# Function derive f01 from a certain Ec and rJC
def Ff01(Ec,rJC):
  return np.sqrt(8*rJC)*Ec-Ec



# Cavity Parameters
NumC=4; #Cavity levels
aM=destroy(NumC)
adM=create(NumC)
qM=aM-adM
nM=num(NumC) # operator N
IC=qeye(NumC)

# Xmon Parameters
NumX=3; #Xmon levels
IX=qeye(NumX)

# Tensor Matrix
HaM=tensor(nM,IC,IC,IX)
HbM=tensor(IC, nM, IC, IX)
HmM=tensor(IC, IC, nM, IX)
IC3=tensor(IC, IC, IC)
QII=tensor(qM, IC, IC)
IQI=tensor(IC, qM, IC)
IIQ=tensor(IC, IC, qM)
HabM=tensor(qM, qM, IC, IX)
```

```
HamM=tensor(qM, IC, qM, IX)
HbmM=tensor(IC, qM, qM, IX)


# Plot eigenenergies
# Energy levels for all flux range
NumEn=5
NumPoints=1000
FluxV=np.linspace(0,1.4,NumPoints)
rJCV=rJCmax*np.cos(FluxV);
FluxMat_all=np.tile(FluxV,(NumEn,1)).transpose()
EnMat_all=EnHtV(rJCV,NumEn)

plt.plot(FluxMat_all,EnMat_all)
plt.xlabel('f')
plt.ylabel('En [Hz]')
plt.savefig('fig-En1.pdf')
plt.show()

# Energy levels for Xmon mixing with Ra/Rb and Rm
NumEn=5
NumPoints=1000
FluxV=np.linspace(0.9,1.2,NumPoints)
rJCV=rJCmax*np.cos(FluxV);
FluxMat_ac=np.tile(FluxV,(NumEn,1)).transpose()[:,1:5]
EnMat_ac=EnHtV(rJCV,NumEn)[:,1:5]

plt.plot(FluxMat_ac,EnMat_ac)
plt.xlabel('f')
plt.ylabel('En [Hz]')
plt.savefig('fig-En2.pdf')
plt.show()


# Energy levels for Ra/Rb eigenmodes
NumEn=3
NumPoints=1000
FluxV=np.linspace(0,1,NumPoints+1)
```

```
rJCV=rJCmax*np.cos(FluxV);
FluxMat_to=np.tile(FluxV,(NumEn,1)).transpose()[:,1:3]
EnMat_to=EnHtV(rJCV,NumEn)[:,1:3]

plt.plot(FluxMat_to,EnMat_to)
plt.xlabel('f')
plt.ylabel('En [Hz]')
plt.savefig('fig-En3.pdf')
plt.show()

EnDiff=np.abs(EnMat_to[:,0]-EnMat_to[:,1]);
EnDiffMin= np.amin(EnDiff)
IdMin = np.where(EnDiff == EnDiffMin)[0][0]


# Plot eigenstates
# minus mode
plt.rcParams.update({'font.size': 12})
plt.rcParams.update({'figure.autolayout': True})

plt.plot(FluxMat_Rab[:,0:2],pVMat_Rab[:,0:2])
plt.xlabel('f')
plt.ylabel('Probability')
plt.savefig('fig-pabM.pdf')
plt.show()


# plus mode
plt.rcParams.update({'font.size': 12})
plt.rcParams.update({'figure.autolayout': True})

plt.plot(FluxMat_Rab[:,2:4],pVMat_Rab[:,[1,3]])
plt.xlabel('f')
plt.ylabel('Probability')
plt.savefig('fig-pabP.pdf')
plt.show()
```